Spring 2019

Effect of Grain Size and Interface Engineering on the Photovoltaic Performance and Stability of Perovskite Solar Cells

Abdullah Al Mamun
Old Dominion University, mamun.apece.du@gmail.com

EFFECT OF GRAIN SIZE AND INTERFACE ENGINEERING ON THE PHOTOVOLTAIC PERFORMANCE AND STABILITY OF PEROVSKITE SOLAR CELLS

by

Abdullah Al Mamun
B.S. June 2012, University of Dhaka
M. S. July 2014, University of Dhaka

A Dissertation Submitted to the Faculty of
Old Dominion University in Partial Fulfillment of the
Requirements for the Degree of

DOCTOR OF PHILOSOPHY

ELECTRICAL AND COMPUTER ENGINEERING

OLD DOMINION UNIVERSITY
May 2019

Approved by:

Gon Namkoong (Director)

Hani E. Elsayed-Ali (Member)

Helmut Baumgart (Member)

Tarek Abdel-Fattah (Member)

ABSTRACT

EFFECT OF GRAIN SIZE AND INTERFACE ENGINEERING ON THE PHOTOVOLTAIC PERFORMANCE AND STABILITY OF PEROVSKITE SOLAR CELLS

Abdullah Al Mamun
Old Dominion University, 2019
Director: Dr. Gon Namkoong

Organic-inorganic halide perovskite solar cells (PSCs) have grown rapidly in recent years due to their outstanding optoelectronic properties, high efficiency, and low-cost. However, this emerging solar cell technology is experiencing some challenges such as defects, hysteresis, and long-term stability, which need to be addressed in order to make it commercially available. This dissertation aims to assist in overcoming some of the barriers and is therefore important to the field of perovskite solar cells.

Initially, this dissertation focuses on investigating the role of grain interiors (GIs) and grain boundaries (GBs) of perovskite film using chemically, spatially, and temporally resolved measurements at the nanoscale level. It is shown that, the GBs are defective with deeper defect levels and are unfavorable to the high performance of perovskite solar cells. Therefore, larger grain perovskite film can be considered as a plausible solution for better quality perovskite films. This work leads to a novel deconvoluted PL approach to determine the charge carrier dynamics of the GI and the GB of the perovskite film. We have quantitatively demonstrated that the charge carrier dynamics of the GI and GB can be analyzed from the ordered and disordered phase of the asymmetric PL spectrum observed in the perovskite film. This deconvoluted PL approach is simple, rapid, non-destructive, and requires no sample preparation compared with the currently available nanoscale characterization measurements.

Subsequently, this dissertation describes the interface defect passivation between perovskite and the electron transport layer (ETL). To address this, a novel thin film of PCBM/carbon was introduced as ETL in the device architecture, which reduces the interface defects and increases the conductivity compared with that of the competitive ETL of PCBM/C60. Moreover, carbon is abundant in nature and the use of carbon in perovskite solar cells will reduce the manufacturing cost.

Finally, the limitation of the air instability of perovskite film is investigated. For that, an in-depth study of degradation pathways of the perovskite film in air was performed using optical, crystallographic, morphological, and mechanical measurements. Based on this study, we suggest the modification of perovskite device architecture to improve the stability of perovskite solar cells in air.

This thesis is dedicated to my parents and family.

ACKNOWLEDGMENTS

I would first like to express my genuine gratitude to my supervisor Dr. Gon Namkoong for giving me the opportunity to work in his research group and pursue my PhD under his guidance. I am grateful that I worked under such a supportive, knowledgeable, and visionary person. He taught me everything from scratch and steered me always in the right direction. Also, he not only assisted me in all aspects of my PhD program but also encouraged me in my failures.

I would like to thank my exam committee members Dr. Hani E. Elsayed-Ali, Dr. Helmut Baumgart, and Dr. Tarek Abdel-Fattah for being on my thesis committee and for their continuous guidance and valuable time.

I would also like to give my appreciation to Dr. Mun Seok Jeong, Dr. Hargsoon Yoon, Dr. Kai Zhang and Dr. Wei Cao for assisting me with various characterization tools and for all the help. Also, I would like to offer my thanks to my colleagues Enas Younes, Derek Demuth, Douglas Ford, Loi Nguyen, Christine Gausin, Jonny Blincoe, Hyeryung Byun, Seonhye Han, Pengtao Lin, Xin Chen, Md Nizam Sayeed, Md Mahmudur Rahman, Tasnuva Ashrafee, and Mahbubul Alam for their support. A special thanks to Md Haider Ali Shaim for supporting me throughout my PhD program. Also, I would like to thank all my Bangladeshi, American, and international friends for their support.

Finally, I must express my profound gratitude to my parents and family members for their unfailing support and continuous encouragement throughout my years of study and through the process of researching and writing this thesis. At last, I thank my wife and colleague, Tanzila Tasnim Ava for her patience and massive support throughout the PhD program.

TABLE OF CONTENTS

Page

Chapter Page

Chapter Page

LIST OF TABLES

LIST OF FIGURES

Figure Page

Figure Page

Figure Page

Figure Page

CHAPTER 1

INTRODUCTION

1.1 Motivation

The climate of the world is changing and posing a serious threat to places, species and people's livelihoods on earth day by day. The increase in global temperature is causing climate alteration and unexpected weather changes. For example, heat waves, frequent flooding, and intense drought are experienced in many places. Greenhouse gases, such as carbon dioxide pollution, are considered to be one of the major causes of global warming. Carbon dioxide acts like a blanket, trapping heat in the atmosphere and raising the temperature of our climate. These gases are naturally found in the atmosphere; however, extensive burning of fossil fuels (e.g., coal, oil, diesel) and deforestation increases the emission of greenhouse gases more [1,2].

According to the United States Environmental Protection Agency (EPA) [1], average global temperatures have risen since 1901. The world's top 10 warmest years on record have been since 1998. A clear indication of global warming is related to the increase of water temperature worldwide. Scientists around the world have come to the overwhelming consensus that climate change is primarily caused by human activity. Producing energy by burning fossil fuels such as coal, oil, and natural gas has a greater impact on the atmosphere than any other single human activity. Global power generation causes about 23 billion tons of CO_2 emissions per year [2]. Coal emits 70% more carbon dioxide than natural gas for every unit of energy produced [2]. The electricity sector in the United States is responsible for about 29% of global warming emission which mainly originates from fossil fuels such as coal, natural gas, etc. [2].

Atmospheric carbon dioxide (CO_2) levels are higher than ever in the last 400,000 years, as shown by National Oceanic and Atmospheric Administration (NOAA) in Fig. 1 [3]. At the time of the Ice Age, CO_2 levels were about 200 ppm, but in 2013, for the first time ever, CO_2 levels exceeded 400 ppm [3]. The continuous rise in atmospheric CO_2 levels since 1950 shows a constant relationship with fossil fuel burning [3]. If the burning of fossil-fuels continues at the normal level, CO_2 will continue to rise to levels of 1500 ppm in the next few centuries [3]. The atmosphere on earth will never be the same as it was before industrialization. Along with portraying scientific measurements, this graph indicates that controlling human activity can have a positive impact on changing the climate and saving our planet for future generations.

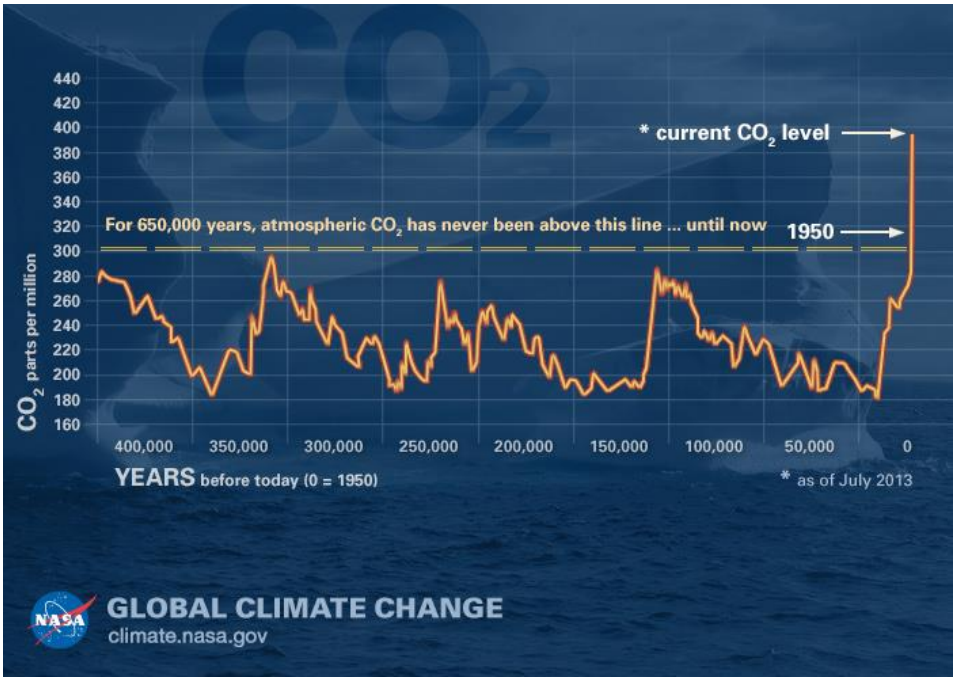

Fig. 1. The continuous rise of CO_2 level in earth's atmosphere from the year 1950 [3].

Renewable energy is one of the most effective solutions to fight against deadly and alarming environmental changes. Renewable energy will not only replace existing fossil-fuel based energy consumption but also will be a source of economic benefit. Most importantly, we will be able to fight against global warming since most renewable energy sources release little to no greenhouse gases. Global warming emissions will be minimized, as evidenced by the data in Fig. 2, even though the overall life cycle of renewable energy sources, including manufacturing, installation, maintenance and disassembly, is considered [4]. Fig. 2 states the comparison between renewable and non-renewable energy sources with respect to CO_2 emission into the environment. For example, non-renewable energy sources like natural gas and coal release 0.62 to 2 pounds of carbon dioxide equivalent per kilowatt-hour (CO_2E/kWh) [6]. On the other hand, renewable energy sources, such as wind, solar, and geothermal cause a maximum emission of 0.2 CO_2E/kWh [6]. An exception is the use of biomass as a renewable source of energy, which can lead to greenhouse gas emissions depending on the resource and whether sustainably sourced or harvested. This means replacing renewable energy sources with non-renewable energy sources will not only prevent global warming but can also significantly reduce CO_2 emissions.

According to a study by the National Renewable Energy Laboratory (NREL), it is possible to produce nearly 80% of the national electricity generation in the United States using renewable energy sources by 2025. In addition, it states that replacing non-renewable energy sources with renewable energy sources can reduce greenhouse gas emissions by about 81% [5]. In 2017, nearly 11% of the total energy consumption in the United States was provided by renewable energy sources which is equivalent to about 11 quadrillion British thermal units (Btu) (1 quadrillion = 10^{15}), as shown in Fig. 3. Of the 11% renewable energy sources, almost 45% of the energy produced is from biomass, which can release greenhouse gases and cause global warming if not

properly sourced [11]. However, solar energy is considered to be a clean energy source with only 0.07 to 0.2 pounds of CO_2E/kWh [6]. Therefore, solar energy can be a solution to achieve clean energy by reducing greenhouse gas emissions into the environment.

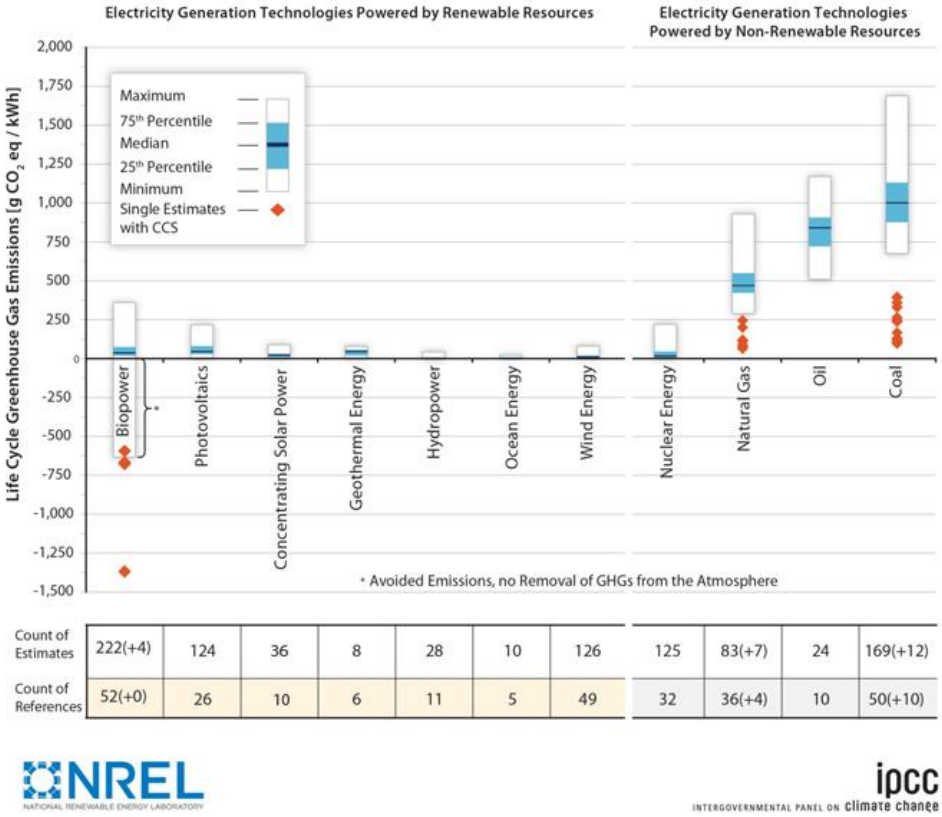

Fig. 2. Amounts of greenhouse gases emission by different energy producing renewable and non-renewable sources. Renewable energies tend to have much lower emissions than other sources, such as natural gas or coal [6].

Solar power is a technology where solar radiation is converted into electricity. The solar power that we currently have is known to have been introduced 60 years ago, but the original

history spans more than 200 years. Today, we have everything from solar-powered homes to solar-powered vehicles and equipment on both earth and in space. The concept of the solar cell was first introduced by French scientist Edmond Becquerel when he discovered the photovoltaic effect in 1839 [7]. The first solar cell with 1-2% efficiency was created by New York inventor Charles Fritts in 1883 by coating selenium with a thin layer of gold [8]. Later, Albert Einstein received the Nobel Prize in 1921 by explaining the photoelectric effect [9], which was first observed by Heinrich Hertz. Today's solar cells depend on this photoelectric effect. In 1954, silicon was used to make solar cells with 6% efficiency by physicists at Bell Laboratories [8]. Afterwards, Western Electric began selling commercial licenses for its silicon photovoltaic (PV) technology in 1956 [10].

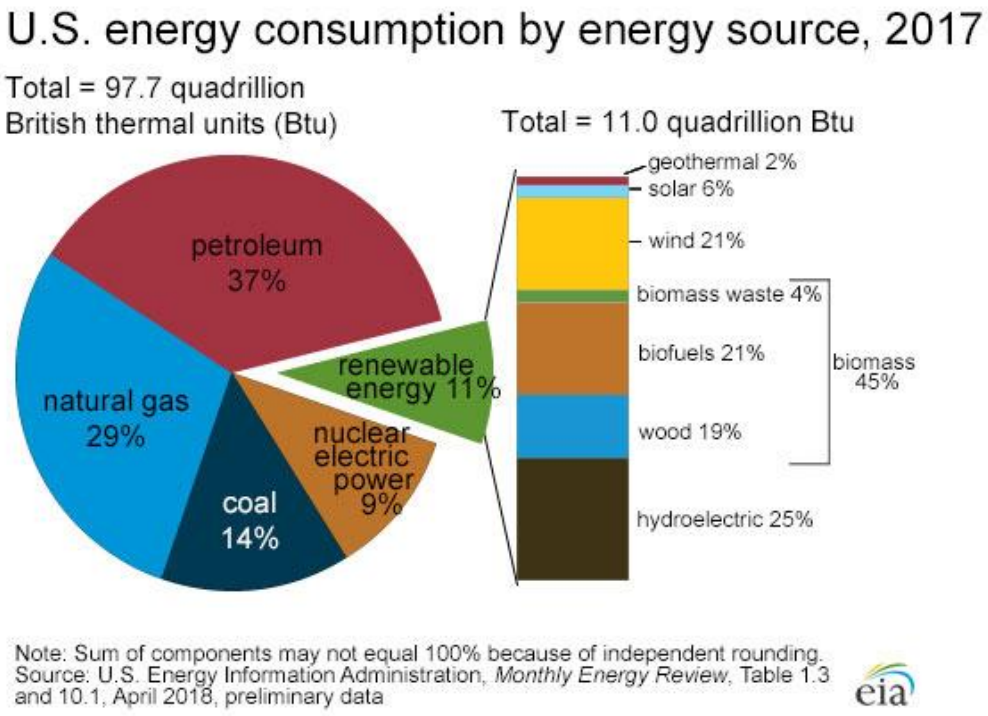

Fig. 3. U.S energy consumption of 2017 from different energy sources [11].

Si based solar cells have dominated the solar industry for the last 60 years by achieving a high efficiency above 26% (Fig. 4) [12]. In addition, many other thin film technologies such as CIGS, CdTe, and GaAs have exhibited higher efficiency and are used commercially. However, these existing commercial PV technologies show several drawbacks such as high installation and production cost [13], requirement of high-temperature and high vacuum technology. Hence, numerous next generation solar technologies have been developed, which include dye-sensitized solar cells (DSSCs), organic photovoltaics (OPVs), quantum-dot solar cells, etc. [14]. All of these emerging technologies require a low-cost fabrication process and exhibit promising photo-conversion efficiency (PCE). Recently, a new type of solution processed solar cells, known as perovskite solar cells (PSCs) have achieved a PCE of above 22% and have attracted the attention of researchers due to their impressive balance between low cost and high efficiency [13].

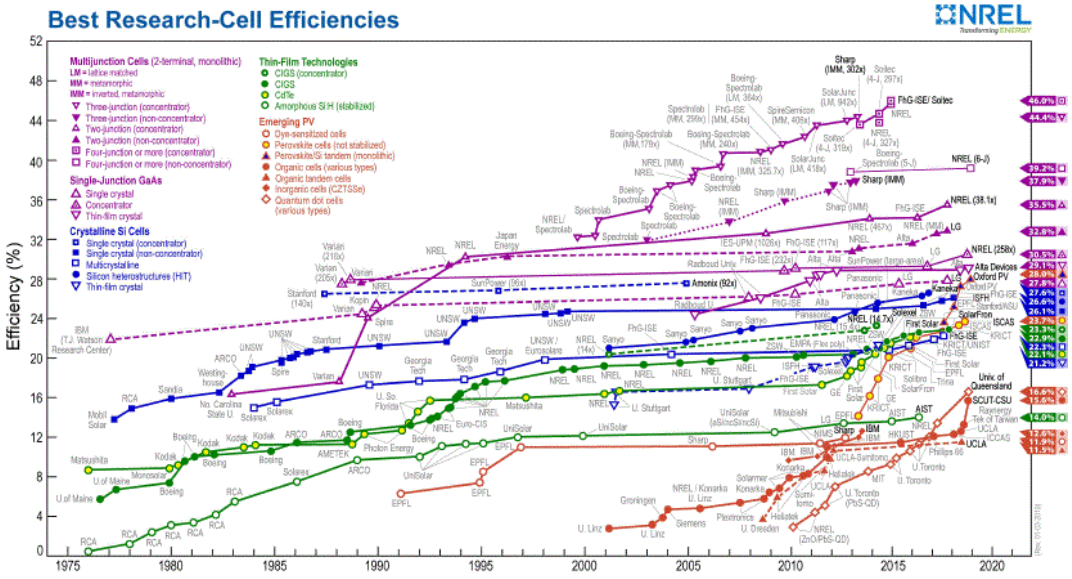

Fig. 4. Best solar cell efficiency chart by National Renewable Energy Laboratory (NREL) [12].

1.2 Outline of the thesis

Chapter 1 demonstrates the deadly impact of global warming in the present and future and the need for renewable energy and solar energy to replace existing fossil-fuel based energy sources. Later, the next generation solar cell named perovskite solar cells (PSCs) is introduced in this chapter.

Chapter 2 covers the overview and background of perovskite material, perovskite device structure, working principle, and the performance evaluation method. Finally, a brief description of the advantages and limitations of perovskite solar cells is illustrated.

Chapter 3 provides detailed fabrication and characterization techniques that have been used throughout the thesis. This chapter also contains conditions and parameters for different fabrication processes and characterization techniques.

Chapter 4 provides investigation of grain interior (GI) and grain boundary (GB) of perovskite film using chemically, spatially, and temporally resolved measurement [15]. In particular, SEM/EDS and 2D steady-state photoluminescence (PL) and time resolved photoluminescence (TRPL) are used to characterize GI and GB.

Chapter 5 elucidates a new characterization approach using deconvoluted PL to determine perovskite film quality [16]. Moreover, the recombination mechanism of chare carrier in GIs and GBs of different sized grain is described. Lastly, the photovoltaic performance of different grain sized PSCs is compared.

Chapter 6 illustrates the effect of a novel electron transport layer of PCBM/carbon which can be used in PSCs to improve the interface defects and remove hysteresis from the solar cell [17]. In addition, the photovoltaic performance of three different ETLs, i.e. PCBM, PCBM/C60 and PCBM/carbon is compared.

Chapter 7 describes the detailed degradation mechanism of perovskite film using optical, crystallographic, morphological, and mechanical characterization techniques [18]. In particular, UV-vis spectroscopy, steady state photoluminescence, XRD, SEM and nanoindentation have been used.

Chapter 8 finally summarizes the conclusions of this dissertation and the future prospects of this work. It is shown that modification of perovskite solar cell architecture is needed to achieve better air stability.

CHAPTER 2

BACKGROUND AND LIMITATION OF PEROVSKITE SOLAR CELLS

2.1 Perovskite crystal structure

The initial meaning of "perovskite" was related to the crystal structure of calcium titanate, which was discovered in 1839 by the German mineralogist Gustav Rose and was named by the Russian mineralogist Lev Perovski [19].

Perovskite compounds have a general chemical formula of ABX_3, where A and B are cations and X is an anion. Their crystal structure is similar to that of calcium titanium oxide. A typical unit cell structure of a basic perovskite compound is shown in Fig. 5. Usually, the A cations are larger than the B cations. Oxide perovskites have been studied extensively because of their multifunctional nature [19]. However, owing to their wide bandgap, oxide perovskites harvest only 8–20% of the solar spectrum, limiting their use in photovoltaic applications [19]. Instead, halide organic-inorganic perovskites were developed by replacing the oxygen anion of oxide perovskites with an inorganic halide (I^-, Cl^-, Br^-) [19]. An organic or inorganic monovalent A^+ cation (e.g., Rb^+, Cs^+, methyl-ammonium $CH_3NH_3^+$, formamidinium $HC(NH_2)_2^+$) and a divalent B^{2+} metal cation (e.g., Pb^{2+}, Sn^{2+}, Ge^{2+}) were also implemented in the frame of the perovskite structures [19]. Among them, methylammonium lead iodide ($CH_3NH_3PbI_3$) is the most widely used perovskite light absorber.

The halide perovskites obtain a desired crystal symmetry by maintaining an allowable tolerance factor. A tolerance factor developed by Goldschmidt [20] determines the radii sizes associated with cubic symmetry, described by

$$t = \frac{R_A + R_X}{\sqrt{2}(R_A + R_X)} \quad (1)$$

where R_A, R_B, R_X are the ionic radii of A, B, X, respectively. The tolerance factor provides a rough estimate of the stability and distortion of crystal structures of a compound. In addition, it gives an idea of whether the phase is cubic (t = 1) or deviates into the tetragonal or orthorhombic phase [21]. In general, an established tolerance factor value for halide perovskites lies in the range of $0.85 < t < 1.11$ (Fig. 6) [22]. Non-perovskite structures are formed when the tolerance factor is higher or lower. In an inorganic-organic hybrid perovskite, it is difficult to calculate the absolute tolerance factor as the organic cation has a non-spherical geometry [23]. However, it is possible to qualitatively analyze the transition of structure in these materials. For example, formamidinium lead iodide, $HC(NH_2)_2PbI_3$ ($FAPbI_3$), has a larger A cation than methylammonium lead iodide, $CH_3NH_3PbI_3$ ($MAPbI_3$) and a larger cation would generally represent a higher tolerance factor [24].

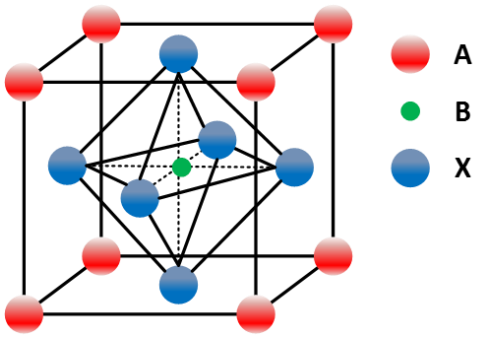

Fig. 5. The unit cell of cubic perovskite (ABX_3), where the red spheres at lattice corners are A cations, the green sphere at the center is a B cation, and the blue spheres at the lattice faces are X anions [25].

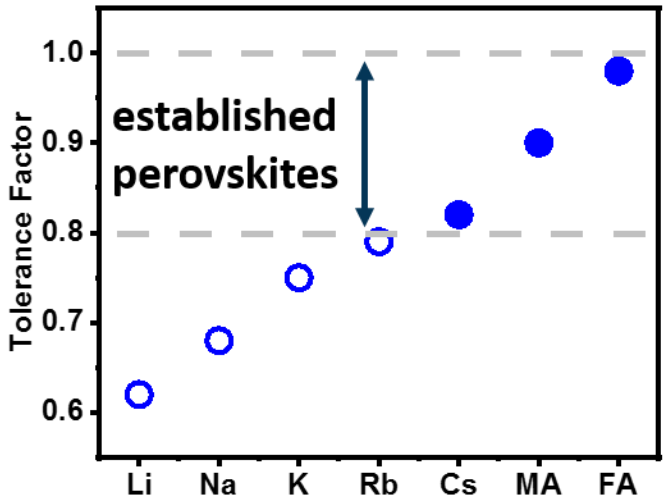

Fig. 6. Tolerance factor of $APbI_3$ perovskites, where A= Li, Na, K, Rb, Cs, MA, and FA [26].

2.1.1 Impact of organic or inorganic A cation

As mentioned before, the typical crystal structure of perovskite is denoted as ABX_3, where A is a cation and can be organic or inorganic, such as methylammonium (MA) $CH_3NH_3^+$, formamidinium (FA) $CH_2(NH_2)_2^+$, Cs^+, or Rb^+. $MAPbX_3$, $FAPbX_3$ and $CsPbX_3$ (X = Br or I) are considered as pure perovskite compounds, which are suitable for photovoltaic applications. $MAPbI_3$ has been extensively used as the light absorber and has showed efficiencies close to 20%. $FAbI_3$ attracted many due to its smaller bandgap and high heat resistance [27]. However, pure $FAPbI_3$ lacks structural stability at room temperature as it can crystallize either into a photoinactive, non-perovskite hexagonal δ-phase (‘‘yellow phase’’) or a photoactive perovskite α-phase (‘‘black phase’’) [26,28] sensitive to solvents or humidity. The need for absolute replacement of organic cations leads to the idea of using inorganic cesium lead halide, which

showed excellent thermal stability [29]; however, $CsPbBr_3$ does not have a favorable bandgap for PV applications and $CsPbI_3$ crystallizes in a photoinactive phase at room temperature and exhibits a photoactive stable perovskite phase only at temperatures above 300 °C [30]. Recently, multiple cation perovskite such as cesium (Cs) and formamidinium (FA) or methylammonium (MA) have demonstrated high power conversion efficiency and promising stability [31].

2.1.2 Impact of B metal cation

B is an inorganic cation in ABX_3 perovskite structure. Generally, a divalent metal such as Pb^{2+}, Sn^{2+}, or Ge^{2+} can be used as the metal cation. Among the various alternatives, lead is by far the most suitable in terms of overall performance of perovskite solar cells. However, the toxicity of heavy metals like lead has raised the necessity of a replacement since lead exposure is very harmful for the environment. Germanium and Silicon are the best alternatives to lead. These alternative elements (Si^{2+}, Sn^{2+} and Ge^{2+}) are unstable up on exposure to air [32]. Tin is considered to be the best alternative to replace lead among the other metals. Sn-based hybrid perovskites have been shown to exhibit outstanding electrical and optical properties, including high charge carrier mobilities, high absorption coefficients, and low exciton binding energies [33,34]. Even *et al.* [35] and Chiarella *et al.* [36] have theoretically shown promising properties of Sn perovskites, such as suitable band gaps and favorable effective mass. However, the primary challenge of Sn-based perovskite solar cells is their sensitivity towards oxidation from Sn^{2+} state to Sn^{4+} state when exposed to air. Consequently, lead based PSCs are dominating since their analogous tin-based PSCs showed efficiency below 10% [32].

2.1.3 Impact of X halide anion

Three different halides are mainly used in perovskite solar cells such as Cl^-, Br^-, and I^-. The most common single halide perovskites are $MAPbI_3$, $FAPbI_3$, and $CsPbBr_3$ [37]. In particular, methylammonium lead iodide has an optical bandgap of 1.55 eV, large diffusion length, and longer carrier lifetime. Later, mixed halide-based perovskite ($MAPbI_{3-x}Cl_x$, $MAPbI_{3-x}Br_x$) was introduced into the PV technology [15]. In particular, a small amount of chlorine improves the solar cell performance by removing the defects from the perovskite film [38]. Moreover, the diffusion length of $MAPbI_{3-x}Cl_x$ is more than 1 µm, whereas single halide perovskite film has a diffusion length of about 100 nm [38,39,40]. In this thesis, $MAPbI_{3-x}Cl_x$ have been studied mainly as the light absorbing layer of PSCs.

Another important property of perovskite is tunable bandgap, which is achieved by changing the amount of iodine and bromine in a mixed halide perovskite. For instance, the absorption onset of $FAPbI_{3-x}Br_x$ can be tuned from 556 nm (2.23 eV) to 838 nm (1.48 eV) [25]. Note that, there is no significant change of absorption band edge observed in the chlorine based mixed halide perovskite.

2.2 Device Architecture

Perovskite solar cells were first introduced by Miyasaka *et al.* in 2009 with a PCE of 3.9% [41]. The device structure used by them was a TiO_2 based meso superstructure with $MAPbI_3$ and $MAPbBr_3$ perovskites. Later, the efficiency of the meso superstructure perovskite solar cells was improved by using a modified fabrication process, innovative device engineering, and better understanding of device physics. However, this device requires high-temperature (>450 °C) during the fabrication process and increases the fabrication cost [42]. World-wide research efforts have

revealed that it is possible to devise a planar structure with perovskite due to its ambipolar transport properties [39] and long electron-hole diffusion lengths [39]. First planar architecture-based PSC was introduced by Guao *et al.,* which showed an efficiency of ~4% [43]. Device engineering has led to approximately 20% efficient PSCs with planar device structure. The comparable efficiency of planar to mesoporous device structure make them feasible to use in PSCs since the processing temperature is low for a planar structure. Different perovskite solar device architectures are shown in Fig. 7.

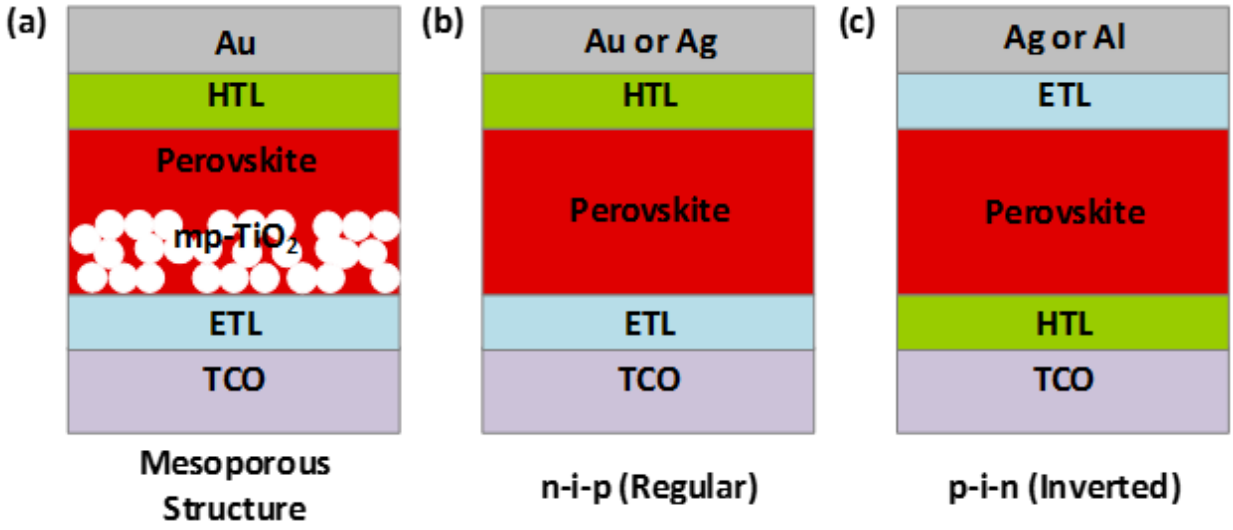

Fig. 7. Three typical device architecture of perovskite solar cells. (a) Mesoporous, (b) n-i-p (regular), and (c) p-i-n (inverted) structure. (HTL: hole transport layer; ETL: electron transport layer; TCO: transparent conductive oxide) [39].

Planar architecture can be classified as a regular n-i-p and an inverted p-i-n structure according to the position of electron and hole transport layers, as shown in Fig. 7. The regular n-

i-p structure is influence by dye-sensitized solar cells (DSSCs) and the inverted p-i-n structure is inspired by organic solar cells. In the early stage of development, perovskite solar cells used an n–i–p structure [44,45] employing an n-type TiO_2 layer as a bottom electron transport layer (ETL) and p-type spiro-OMeTAD as a top-hole transport material (HTM) [46,47]. However, high temperature sintering of TiO_2 inevitably increases manufacturing costs and trapped charges at the interface between the perovskite and the TiO_2 ETL led to decomposition of the perovskite structure through a sequence of chemical reactions [42]. Furthermore, spiro-OMeTAD suffers from high cost and low stability [47]. Thus, HTM-free perovskite solar cells using carbon or graphene paste have been developed [48,49,50,51]. Alternatively, inverted p–i–n device structures of FTO/PEDOT: PSS/perovskite/PCBM/Ag or Al were sought [52,53] due to low temperature processes and better device flexibility. However, an inverted perovskite solar cell typically exhibited notorious photocurrent hysteresis [52,53]. In this thesis, we have fabricated a PSC with a p-i-n architecture to improve efficiency and stability and reduce hysteresis.

2.3 Working principle of PSCs

A typical Perovskite solar cell is made of an active layer, charge transport layers, and electrodes. As mentioned earlier, this thesis work is based on inverted p-i-n device architecture. In this structure, perovskite serves as the active layer or light harvesting layer which is sandwiched between a p-type hole transport layer (e.g., PEDOT: PSS) and n-type electron transport layer (e.g. PCBM), as shown in Fig. 8. A transparent conductive layer of FTO and a metal layer of Ag act as the back and front contact, respectively for inverted p-i-n device structure. The most commonly used perovskite material is $MAPbI_3$. Our work mainly focuses on perovskite solar cells based on $MAPbI_{3-x}Cl_x$ perovskites.

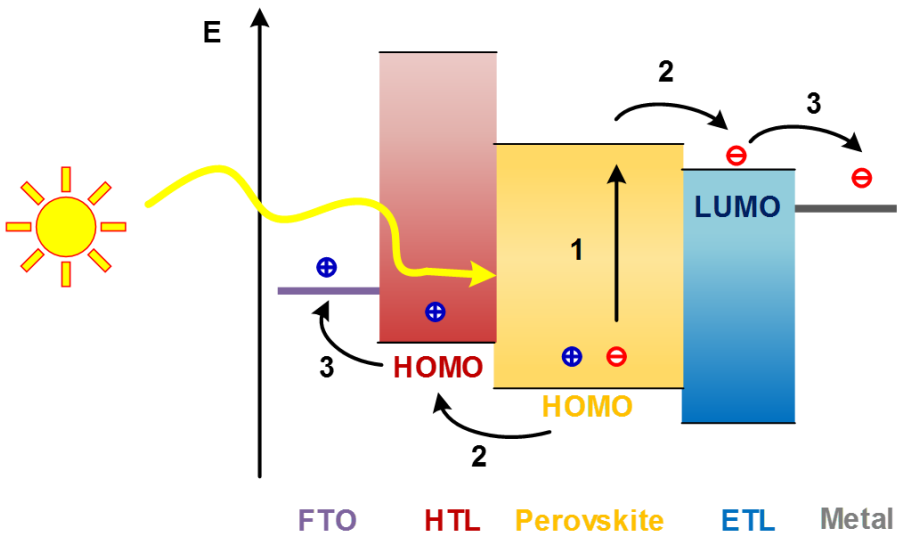

Fig. 8. Energy band diagram of a typical p-i-n (inverted) perovskite solar cells. Basic working principle can be explained as: 1. Light absorption and exciton formation, 2. Charge carrier separation, 3. Charge carrier extraction [54].

When light is absorbed by perovskite, an electron is transferred from HOMO (highest occupied molecular orbital) to LUMO (lowest unoccupied molecular orbital). HOMO and LUMO resemble the valence band and conduction band as in inorganic semiconductors. With the transfer of an electron from HOMO, a hole is created, resulting in an electron-hole pair. Unlike an inorganic semiconductor, this electron and hole pair is regarded as excitons [54]. The excitons are bound electron-hole pairs with a relatively large binding energy ranging from 0.3 to 1 eV [54]. A photo-current is generated when the excitons overcome this binding energy by absorbing light and dissociating the bound electron-hole pair into free charges. The exciton dissociation in perovskite solar cells occurs at the p-type (donor) and n-type (acceptor) interface. After dissociation, free charges are diffused to the respective charge transport layer (electrons to ETL and holes to HTL)

and are collected by the metal electrodes. The free charges move through the metal electrodes and when connected with a wire, a photo-current is generated.

2.4 Single diode equivalent circuit and performance calculation

The equivalent circuit of an ideal solar cell can be represented as a current source connected in parallel with a diode. An ideal current source delivers current in proportion to the amount of exposed solar illumination present. The ideal current-voltage equation is expressed as,

$$I = I_0 \left(e^{\frac{qV}{nk_BT}} - 1 \right) - I_{pH} \quad (1)$$

where I_0 is the saturation current, I_{ph} is the photocurrent, n is the ideality factor, q is the electron charge, k_B is the Boltzmann constant, and T is the cell temperature.

However, in a practical solar cell, the I-V characteristics performance is influenced by a series resistance, R_s, and a shunt resistance, R_{sh}. The influence of these parameters on the I-V characteristics of the solar cell can be studied using an equivalent circuit as shown in Fig. 9. The I-V characteristics of the one-diode equivalent circuit with series resistance and shunt resistance can be represented as [55],

$$I = I_0 \left(e^{\frac{q(V-R_sI)}{nk_BT}} - 1 \right) + \frac{V-R_sI}{R_{sh}} - I_{pH} \quad (2)$$

where, R_s is the series resistance and R_{sh} is the shunt resistance.

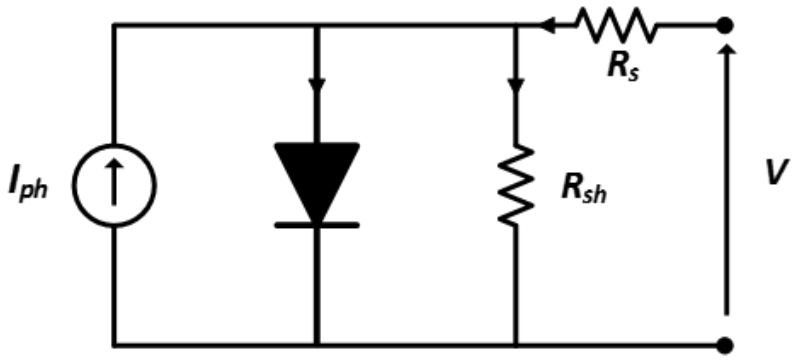

Fig. 9. Equivalent circuit of a solar cell (single diode model) [55].

The typical J-V characteristics of a solar cell and corresponding power curve are shown in Fig. 10. The most common parameters of J-V curves are short circuit current (J_{SC}), Open circuit Voltage (V_{OC}), and Fill Factor (FF). Short circuit current (J_{SC}) is the current density of the solar cell when no voltage is applied. Open circuit voltage (V_{OC}) is the voltage when no current is flowing through the solar cell. Fill Factor (FF) relates to the maximum power which can be represented as,

$$FF = \frac{V_{max}J_{max}}{V_{OC}J_{SC}}. \quad (3)$$

The main parameter that evaluates the performance of one solar cell to another solar cell is efficiency (η), which can be represented as

$$\eta = \frac{P_{out}}{P_{in}} \quad (4)$$

where, η is the efficiency, Power output, $P_{out} = V_{oc} \times I_{sc} \times FF$, and power input, $P_{in} = 100\ mW/Cm^2$.

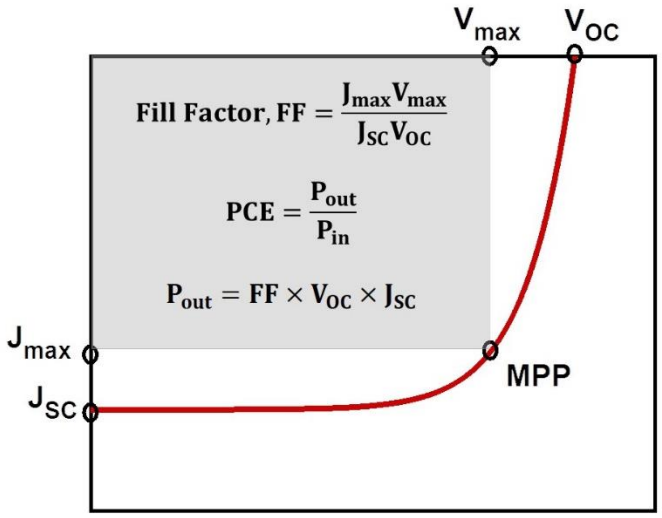

Fig. 10. Typical current – voltage (J-V) characteristics of a solar cell.

2.5 Advantages of PSCs

Hybrid organic-inorganic perovskites have attracted much attention in recent years due to their outstanding optoelectronic properties [56,57,58,59,60,61,62,63] and opened new avenues for optoelectronic applications such as photovoltaics [64,65,66,67,68,69], photodetectors [70], light emitting diodes (LEDs) [71], and lasers [72,73]. In the photovoltaic research, perovskite materials have achieved photo conversion efficiencies exceeding 22% [12]. In particular, perovskites have gotten the most attention in the field of photovoltaics as a new candidate for next-generation photovoltaics in an unprecedentedly short period of time. During the past few years, refined fabrication processes of perovskite solar cells, improved understanding of solar cell physics, and innovative device engineering have led to significant progress and much improved cells that operate at greater than 20% efficiency. In particular, worldwide research efforts have revealed exceptional optical and electrical properties such as high electron and hole mobility strong defect tolerance, large absorption characteristics, and long electron-hole diffusion lengths.

In particular, perovskite material has a large absorption co-efficient of 10^5 cm^{-1} [74], which paves a way to fully utilize the photon energy absorbed by a thin perovskite film (approximately 300 nm) and delivers high current from the device. In addition, the electron beam induced current measurement on the perovskite device shows that the charge carriers can be collected on both electrodes when an electron beam is focused on one side of the perovskite layer. This clearly supports the ambipolar carrier transport behavior of $MAPbX_3$ perovskites [60]. Moreover, the diffusion length of solution-processed single crystal $MAPbI_3$ perovskite can exceed more than 175 µm [61], which indicates the non-radiative recombination process and suppressed defect associated recombination of free charge carriers. Furthermore, the bandgap of mixed halide perovskite is tunable and provides a wide range of bandgap ranging from 1.48-2.53 eV [75].

2.6 Limitation of PSCs

Despite having outstanding optoelectronic properties for efficient perovskite solar devices, there are some issues related to perovskite materials which need to be addressed in order to make them commercially available. The theoretical power conversion efficiency of a perovskite solar cell is more than 30% [76]. However, in reality, it is still not possible to get such high efficiency with current perovskite solar cells. The key issues regarding industry application of PSCs include power conversion efficiency, hysteresis, charge carrier recombination at the interface, defects, and, most importantly, device stability.

2.6.1 Recombination of charge carriers

The efficiency of PSCs is still far from the theoretical efficiency. One of the reasons behind this is the recombination of charge carriers in the device, which reduces the open circuit voltage (V_{OC}) and fill factor (FF) in PSCs. The recombination mechanism can be classified as radiative and non-radiative recombination. In radiative recombination, an electron from conduction band combines with a hole in the valence band directly, while in non-radiative recombination, an electron or hole is trapped in the forbidden region which forms defect states in the crystal lattice. A dominant non-radiative recombination mechanism in PSCs limits the efficiency of the device.

In polycrystalline perovskite thin films, defects or impurities are found at the grain boundaries (GBs) and at the surfaces. The perovskite film is connected to ETL and HTL in the device structure. Therefore, an interface is formed which is prone to impurities and trap or defect states. Non-radiative recombination at the interface severely damages device performance. Larger grain (mm-scale) perovskite films can efficiently reduce the influence of defective GBs in perovskite thin films by reducing defects associated with GBs. In this work, large grain perovskite film was fabricated using a hot-casting technique in order to reduce the effect of GBs. In addition, the role of GIs and GBs have been systematically studied since there has been a controversy regarding the effect of GBs in the performance of perovskite solar cells.

2.6.2 Hysteresis

Another key issue which influences perovskite solar device performance is the photocurrent hysteresis. The hysteretic current-voltage, J−V behavior between forward (lower voltage → higher voltage) and reverse scan (higher voltage → lower voltage) during current-voltage characterization presents a challenge for determining the accurate power conversion

efficiency of the PSCs. Generally, the reverse scan displays higher PCE than the forward scan, which means the reverse scan and the forward scan displays a mismatch in the efficiency of the PSCs (Fig. 11) [77,78,79]. The J-V hysteretic behavior of PSCs depends on many parameters such as scan rate, voltage range, scan direction, and configurations of PSCs [80,81,82,83,84,85,86].

Presently, there is a strong debate about the origin of the photocurrent hysteresis of perovskite solar cells. The proposed mechanism behind the hysteresis effect involves a slow ferroelectric polarization and the migration of excess ions as interstitial defects under the application of an applied bias [52,53,83,87]. In addition, electron charge traps at surfaces or/and GBs are pointed out as a plausible explanation for notorious hysteresis [52]. The slow decay process of the capacitive charging or discharging during J-V characterization is assumed to cause non steady-state photocurrent and hysteresis [81,82,83,84]. The non-steady state photocurrent, due to capacitive charging or discharging results from electrode polarizations at perovskite and electrode interfaces, which influences the hysteresis. However, the PV performance after light soaking with different bias voltages cannot be explained only with the capacitive effect. The modified steady-state current due to band bending, instead of the capacitive effect, could be the reason behind the change in the PV performance. The origin of band bending is due to trapped charges, ion migrations, or ferroelectric polarization. The extraction efficiency of the electron and hole contributes to the observed hysteresis behavior. The extraction efficiency is influenced by the charge trapping and detrapping process at the interface and grain boundaries, and enhancing charge extraction is vital for controlling hysteresis. The partially trapped states at the interfaces create a depletion region at HTL/Perovskite and ETL/Perovskite interfaces. This leads to a change in the band structure and reduces charge extraction under forward bias condition. Under large forward bias, trap states can be filled, which reduces the depletion region and the band bending. The

trapping and detrapping process of charges thus affect the hysteresis behavior in PSCs. Accumulation of ions occurs at interfaces near the electrodes due to ion migration, and an electric field is generated. This ion migration is considered to be another cause of band bending, which influences the separation and extraction of photogenerated charges. Ferroelectric polarization is another possible cause to modulate the electric field distribution, resulting in different PV performance under reverse and forward scan.

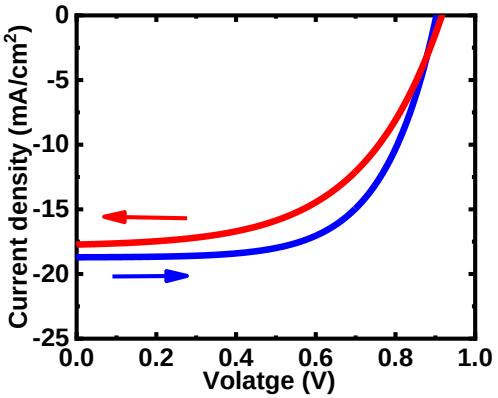

Fig. 11. Hysteresis effect of a solar cell. Current-voltage characteristics are not same in forward and reverse voltage sweep [88].

2.6.3 Device Stability

Presently, a Perovskite solar cell possesses high efficiency at more than 20%. Despite achieving a comparable lab-scale device efficiency to make solar cells commercially available, PSCs have critical issues regarding stability. The common standard PV modules available on the market typically have a warranty to retain their initial efficiency for 20–25 years. However,

perovskite solar cells are prone to degradation when exposed to air, UV light, thermal stress (heat), light soaking, electric fields, and many other factors [18,89,90].

The stability of perovskite devices is affected by different extrinsic and intrinsic factors. The main extrinsic factors are environmental influences such as air and moisture, which decompose the perovskite film as well as the whole device. The exposure of perovskite solar devices to oxygen and moisture in the atmosphere can affect the stability of the components directly. $CH_3NH_3PbI_3$ tends to hydrolyze in the presence of moisture (Fig. 12), which leads to decomposition of perovskite occurring as follows [91]:

$$CH_3NH_3PbI_3\ (s) \leftrightarrow PbI_2\ (s) + CH_3NH_3I\ (aq) \quad (5)$$

$$CH_3NH_3I\ (aq) \leftrightarrow CH_3NH_2\ (aq) + HI\ (aq) \quad (6)$$

$$4HI\ (aq) + O_2(g) \leftrightarrow 2I_2\ (s) + 2H_2O\ (l) \quad (7)$$

$$2HI\ (aq) \leftrightarrow H_2\ (g) + I_2\ (s). \quad (8)$$

It should be noted that moisture, oxygen, and UV radiation are indispensable for the degradation process. The most critical stability issue is the intrinsic instability of PSCs. Hygroscopicity, thermal instability, and ion migration are three major intrinsic factors corresponding to perovskite solar device instability. The hygroscopicity is related to the environmental factors and the thermal instability also leads to the decomposition of perovskite into lead iodide evaporating methylammonium iodide under thermal stress. Lastly, the ion migration is almost inevitable in all halide perovskites due to the high external field applied across the thin films during the J-V scan and the high ionic mobility [92]. Moreover, the situation is more severe at the defective sites, grain boundaries, and the interfaces.

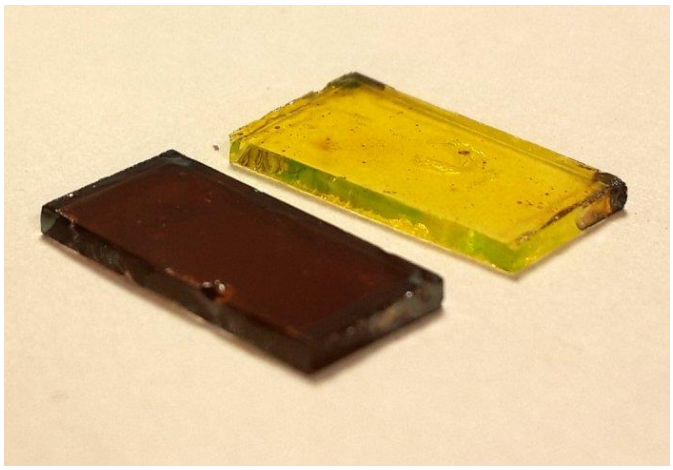

Fig. 12. Degradation effect. Black perovskite films turns into yellow when it is exposed to air for 7 days [93].

2.6.4 Toxicity

The efficiency of perovskite solar cells at laboratory scale has come close to the current silicon photovoltaics available on the market. However, a major concern of these materials is related to the use of heavy metals as cations. The best performed PSCs until now have had a high PCE comprised of lead, which is very harmful in the environment. Although lead is present in batteries and equally toxic chemicals such as cadmium are found in commercial photovoltaics, the possibility of lead exposure in the environment poses a serious threat to the ecosystem. Long-term exposure of toxic chemicals due to occupational or environmental causes will damage human health severely. Therefore, the toxicity issue concerning PSCs are should be considered seriously while progress is being made on its performance and stability.

An alternative to lead could be tin; however, PSCs with tin exhibits much lower efficiency. In addition, Sn^{2+} in perovskite degrades into Sn^{4+} [94]. Hence, the perovskite technology requires installation in an absolutely safe way with proper encapsulation resistant to extreme conditions.

Moreover, an in-depth investigation of the toxicity of Pb and Sn is crucial. Furthermore, standardized protocols for recycling PSC modules should be established as well.

2.7 Summary

Perovskite has a generic chemical structure ABX_3 comprised of two cations and one anion and there are different combinations available by maintaining tolerance factor and electronic properties. In particular, this thesis work will focus on perovskite solar cells with $CH_3NH_3PbI_{3-x}Cl_x$ perovskite. Though the Perovskite solar cell has outstanding optoelectronic properties, it has various limitations such as defective grain boundary, hysteresis, stability, toxicity, etc. These limitations need to be resolved before making it commercial. In this work, several ways to resolve some of these limitations will be discussed.

CHAPTER 3

EXPERIMENTAL METHODS

3.1 Perovskite precursor preparation

A Perovskite ($CH_3NH_3PbI_{3-x}Cl_x$) solution was prepared by dissolving equimolar ratios of lead iodide (PbI_2, Sigma-Aldrich, 99%) and methylamine hydrochloride (MACl, Sigma-Aldrich) in N, N-dimethylformamide (DMF, Sigma-Aldrich, anhydrous, 99.8%) in 11 wt% concentration. In this case, 0.09 g PbI_2 and 0.013 g MACl were mixed in 1 ml DMF. The solution was ready for use after heating on a hot plate at 70 °C for 24 hrs with magnetic stirring in a N_2 filled glove box.

3.2 Perovskite solar cell fabrication

Solar cells were fabricated using an inverted p-i-n device structure. The generic perovskite solar cell has five different layers with the structure of FTO/PEDOT: PSS/perovskite/PCBM/Ag as shown in Fig. 13. Later, a layer of C60 or carbon was inserted between PCBM and Ag to passivate the interface defect and improve efficiency. Moreover, the hole transport layer of PEDOT: PSS was replaced by NiO to improve the air stability.

3.2.1 Transparent electrode FTO preparation

Fluorine doped tin oxide coated (FTO) glasses (SnO_2/F, 8 Ωsq^{-1}, Aldrich) were used as the transparent electrode and substrate of the devices and were etched using zinc powder (Zn, Sigma-Aldrich, 98%) and a hydrochloric acid (HCl, Alfa-Aesar) solution to form the desired pattern. The patterned FTO substrates were subsequently cleaned in ultrasonic baths (Branson 1500) containing

mucasol (Sigma-Aldrich), de-ionized water, methanol (Alfa-Aesar), acetone (Alfa-Aesar) and 2-propanol (J.T.Baker), respectively (each for 10 mins). Afterwards, the substrates were dried with nitrogen, followed by heat treatment at 120 °C for 20 mins to remove the last traces of any solvent.

3.2.2 Hole transport layer (HTL) deposition

A hole transporting layer was deposited on the cleaned FTO substrate at 3000 rpm for 1 min using a PEDOT: PSS (AI 4083, HERAEUS) solution and annealed at 150 °C for 20 mins. The PEDOT: PSS solution was diluted in 2-propanol (J. T. Baker) in the ratio of 1:3. The thickness of the PEDOT: PSS layer was measured to be about tens of nanometers. In the case of NiO based HTL, the NiO precursor was prepared by mixing 0.72 g of NiO (Sigma-Aldrich) with 2 mL of HCl (Alfa Aesar, 36%) and then stirred at 75 °C for 15 mins. After mixing, the solution was filtered by a 0.45 µm filter. The NiO precursor solution was spun coated at 2000 rpm for 60 s followed by annealing at 350 °C for 15 mins.

3.2.3 Active layer of perovskite deposition

Perovskite ($CH_3NH_3PbI_{3-x}Cl_x$) films were prepared using a hot casting technique. In this process, the substrates were kept at 180 °C and the precursor solution at 70 °C. The solution was then immediately deposited on the hot substrate by spin coating at 4000 rpm for 10 s so that the substrate temperature was retained. During this process, the temperature was closely monitored using an IR (infrared) thermal gun. The thickness of the perovskite was calculated from a cross-sectional SEM image as shown in Fig. 13 (b), which is about 252±7 nm [95]. After depositing the perovskite absorber layer, the devices were transferred to a nitrogen-filled glove box.

3.2.4 Electron transport layer (ETL) deposition

PCBM (Nano-C, 99.5%), used as an ETL, was spun on top of the perovskite layer at 1250 rpm for 60 s in a nitrogen-filled glove box. PCBM was diluted using a solution of 1,2-dichlorobenzene (Alfa-Aesar, 99%) in 2 wt% concentration. The thickness of the PCBM layer was measured to be about tens of nanometers. In chapter 6, a layer of C60 or carbon was inserted between PCBM and Ag contact. C60 or carbon was deposited on top of the PCBM layer at a base pressure of 1×10^{-7} torr. In particular, C60 (Alfa Aesar, 99%) or graphite (Aldrich, 99.99%) was placed in a graphite crucible and irradiated by e-beam. The resultant thickness was ~10 nm, as measured by SEM.

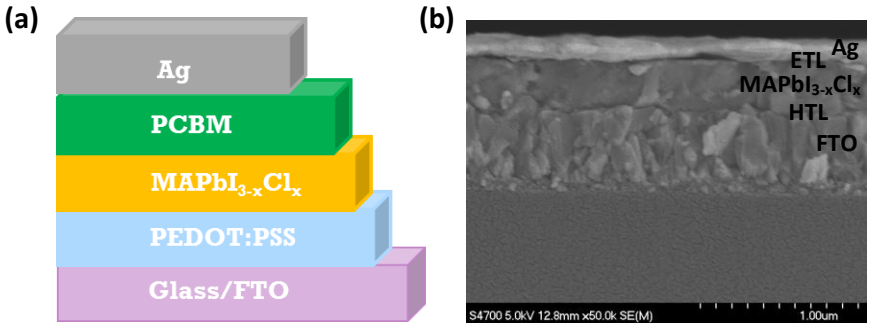

Fig. 13. (a) A schematic of perovskite solar device with the structure of FTO/PEDOT: PSS/perovskite/PCBM/Ag. (b) The cross-sectional SEM image of the corresponding device architecture.

3.2.5 Cathode electrode deposition

Finally, 170 nm thick silver (Alfa-Aesar, 99.9%) as a cathode electrode was deposited at 4 Å per second under a pressure of 1×10^{-7} torr using an electron beam (E-beam) evaporator. The

active area of the device is 10 mm^2. A schematic device structure without the C60/carbon layer is shown in Fig. 13 (a) and the corresponding cross-sectional SEM image is shown in Fig. 13 (b).

3.3 Electrical characterization

3.3.1 Current-voltage characteristics (J-V)

The photocurrent density (J) vs. voltage (V) curves were determined using a Keithley 2400 source meter under AM 1.5G illumination at 100 mW/cm^2 provided by a solar simulator (Newport 69907). One sun illumination was adjusted using the NREL-calibrated, KG-2 filtered Si diode. A 450 W Xenon lamp was used as a light source and the lamp remained on for 30 mins before starting the photocurrent measurement to stabilize the light intensity. J–V curves were obtained by scanning from -0.05 V to 1.2 V.

3.3.2 Hall and Four-point probe measurement

The sheet resistance of the perovskite film was measured using a Jandel RM3 four-point probe. In addition, an Ecopia HMS-5300 Hall effect measurement system was used to determine electrical properties such as sheet resistance, mobility, resistivity, Hall coefficient, and so on.

3.4 Optical characterization

3.4.1 Steady state and time resolved photoluminescence (PL) measurement

Steady-state and time-resolved photoluminescence (PL) measurements were performed using Horiba FluoroLog-3 spectrofluorometer and time-correlated single photon counting

(TCSPC) with a solid-state laser with 450 nm, which was used for the various excitation intensities. Both a continuous 450 W xenon lamp and pulsed laser-diode were used to measure steady-state PL and lifetime decays. The TCSPC is fiber-coupled into Olympus BX53F microscope equipped with a CCD camera capable of measuring PL and lifetime mappings while showing microscopic morphologies.

3.4.2 UV-vis measurements

The UV-vis spectrum was measured by using a Perkin Elmer Lambda 45 spectrophotometer in absorption and transmission mode. To measure UV-vis, a specific layer such as perovskite was prepared on top of a glass substrate following the same fabrication procedure as mentioned in the film preparation section.

3.5 Structural and morphological characterization

3.5.1 X-ray diffraction measurement

X-ray diffraction was conducted using a Rigaku MiniFlex II X-ray diffractometer. An acquisition rate of 5° min^{-1} with a step size of 0.02° was used. X-ray diffraction was used to find out the crystal structure, crystal size, and defects of different films. Crystal size can be calculated from XRD spectrum using Scherrer equation [96,97],

$$L = \frac{K\lambda}{\beta \cos\theta} \quad (9)$$

where L is the average crystal size, λ is the wavelength of the X-ray irradiation (0.154 nm), K is the dimensionless shape factor, β is the full width at half maximum (FWHM), and θ is the Bragg angle. The intermolecular spacing (d_{hkl}) can be calculated from Braggs law,

$$d_{hkl} = \frac{\lambda}{2\sin\theta} \quad (10)$$

where, λ is the wavelength of the X-ray irradiation (0.154 nm) and θ is the Bragg angle.

3.5.2 Scanning electron microscopy (SEM) and energy dispersive X-ray spectroscopy (EDS) measurement

Surface and cross-sectional scanning electron microscope (SEM) images of the perovskite film were collected by a field emission scanning electron microscope (FESEM, JSM7500F, JEOL). Images were taken at different magnifications and accelerating voltages. A thin conductive layer of gold (Au) was coated on the film for preventing electron charging using a Hummer V Sputter Coater before scanning the surface and cross-section of the film. To analyze the compositions of each component in different films, EDS was calibrated with a series of standard samples including SiO_2, KCl, PbF_2, Cu (K_α – 8.04 keV, K_β – 8.9 keV) and others. The measurement uncertainty was estimated to be ±1% by statistical analysis of a series of observations.

3.6 Mechanical characterization

3.6.1 Nanoindentation

To measure the elastic properties of perovskite films, a nanoindenter XP (Agilent Technologies, Inc., Santa Clara, CA) was used in conjunction with the continuous stiffness method (CSM) in depth control mode. The nanoindenter XP is equipped with a three-sided diamond Berkovich probe. The CSM method provides continuous evaluation of the mechanical properties of materials as a function of contact depth. The Berkovich indenter tip was calibrated on fused

silica standards using a preliminary calibration procedure recommended by Agilent Technologies for an initial 100 nm, 500 nm and 2 μm of geometry. Arrays of 12-16 indentation tests were performed with proper spacing between adjacent indents. The allowable drift rate and the strain rate for loading were specified as 0.05 nm/s and 0.05 s^{-1}, respectively.

3.7 Summary

This chapter covers the fabrication and characterization techniques used throughout this thesis. In particular, perovskite thin film was fabricated using a hot-casting technique, where the substrate and precursor solution was kept at a specific temperature. For fabricating other layers, we mainly used spin-coating and e-beam evaporation technique. The detailed parameters of different characterization technique used in this work are described as well.

CHAPTER 4

ROLE OF GI AND GB IN ORGANIC-INORGANIC LEAD HALIDE PEROVSKITE

4.1 Introduction

Halide perovskites have gained tremendous research interest as a new category of semiconductor materials that will revolutionize photovoltaic technologies. During the last few years, significant improvements in the performance of halide perovskite solar cells have been made, thanks to a new understanding of the materials and new device architecture designs [44,59,64,68,98,99,100]. In particular, world-wide research efforts have revealed the exceptional optical and electrical properties such as high electron and hole mobility, strong defect tolerance, large absorption characteristics resulting from s-p antibonding coupling and the long electron-hole diffusion lengths exceeding 1 μm [44,59,64,68,98,99,100]. All of these unique characteristics of perovskites led to unprecedented energy conversion efficiency of perovskite solar cells. However, many problems remain to be solved to unravel the underlying mechanisms that will allow for improved photovoltaic performances. In particular, there's been intensive interest in understanding the nature of grain boundaries (GBs) of perovskites in the solar cell community [40,101,102,103,104,105,106,107]. Since the perovskites are prone to defect formation, due to the low thermal stability of the materials, it is expected that chemical disorder occurs, particularly at the GBs. According to theoretical studies, the GBs are characterized by defects that have very shallow intrinsic levels, i.e. the GBs are completely benign [101]. On the contrary, Agiorgousis *et al.*, also conducted a theoretical calculation and found that the deep charge-state transition levels

within the bandgap were indeed possible by forming Pb dimers and I trimmers through very strong covalent bonds [102].

In addition, experimental studies also revealed controversial results. Until now, the GBs of organic–inorganic halide perovskite films were characterized by confocal fluorescence microscopy, conductive-atomic force microscope (c-AFM), Kelvin probe force microscopy (KPFM), and electron beam-induced current (EBIC) [40,104,105,106,107]. Nanoscale photoluminescence (PL) and lifetime mappings [40,104] unambiguously revealed that the GBs exhibited strong non-radiative relaxation of charge carriers. This result implies that the GBs are defective and not as benign as previously suggested in ref. [101]. In contrast, C-AFM measurements indicate a higher short-circuit current was observed at the GBs than at the grain interiors (GIs), indicating the photo-generated charge carriers more effectively separated at the GBs [103]. Yun *et al*., also conducted KPFM measurements that revealed greatly enhanced charge separation and collection at the GBs, indicating the benign characteristics of the GBs [103]. In short, the confocal microscope optical measurements [40,104] concluded that the GBs can be detrimental whereas the benign characteristics were unveiled by other measurements [103,104]. This begs the question of why defective GBs in perovskite materials do not act as high recombination sites for photogenerated charge carriers but enables perovskites solar cells to achieve their high efficiencies. To address this question, we need to clearly understand the nature of the GBs for perovskite solar cells by contrasting them with the GIs. Hence, in this chapter, we focused on probing defects at the GIs and GBs, on characterizing the discrete roles of the GIs and GBs mostly influenced by morphological, and chemical variations of perovskites through concerted combinations of chemically, spatially, and temporally resolved microscope studies at the nanoscale.

4.2 Hot casting technique for larger grain perovskite

One of the main challenges is to produce pin-hole free morphologies with larger grains during the deposition and crystallization of the perovskite layer. This is because a uniform surface coverage of the perovskite film is crucial for solar cells to avoid shunting [100] and the notorious hysteresis effects [108]. Conventionally, perovskite film is spin coated or sequentially deposited at room temperature followed by annealing at 100 °C to crystallize the film. The sequential deposition or conventional spin-coating methods have been widely used and typically resulted in smaller grain size of 1~2 μm with many pin-holes. However, we have incorporated a hot casting process by following previous reports [109] which gives pinhole free larger grain perovskite films. In this process, perovskite films were prepared when the substrate and solution were kept at 180 °C and 70 °C respectively. Substrate was transferred to spin coater chunks from a hot plate very quickly and the solution was dropped instantly so that temperature remains the same on the top of the sample. During this process, sample temperature is higher than the boiling point of solvents (DMF or DMSO) at the time of spinning in the spin coater. The thermal energy facilitates the formation of a larger grain of the perovskite during the spin-casting process [109]. The difference in grain sizes between the two different hot casting temperatures is shown in Fig. 14.

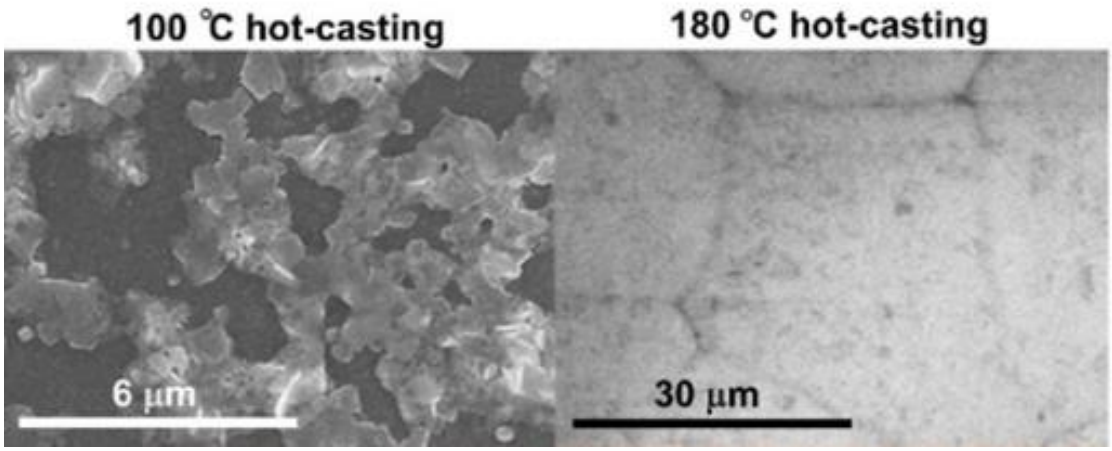

Fig. 14. Comparison of grain sizes of lower (100 °C) and higher (180 °C) hot-casting perovskites [15].

4.3 Chemical analysis of GI and GB of various grain sizes using SEM and EDS

To investigate the local chemical compositions of the GIs and GBs for perovskites, an EDS measurement coupled with an SEM was performed. Fig. 15 shows the two-dimensional (2D) EDS mapping of a higher (180 °C) hot-casting perovskite that highlighted the chemical distributions across the GBs. Remarkably, a higher hot-casting perovskite produced pin-hole free GBs, as shown in the SEM image of Fig. 15 (a). In particular, the chemical components composed of perovskites were carefully examined between the GIs and GBs in order to fully understand the role of GIs and GBs of perovskites. The chlorine signal (2.621 KeV) [110] can be clearly distinguished from the Pb signal (2.342 KeV). The resultant EDS mapping of $CH_3NH_3PbI_{3-x}Cl_x$ clearly revealed that the contents of lead (Pb) and chloride (Cl) in Fig. 15 (b) and (c) were significantly lower at the GBs. Note that the EDS mapping of iodide (I) was not shown but found to be similar to that of Pb. One of the critical observations is an increase in O contents when approaching the GB, as shown in Fig. 15 (d).

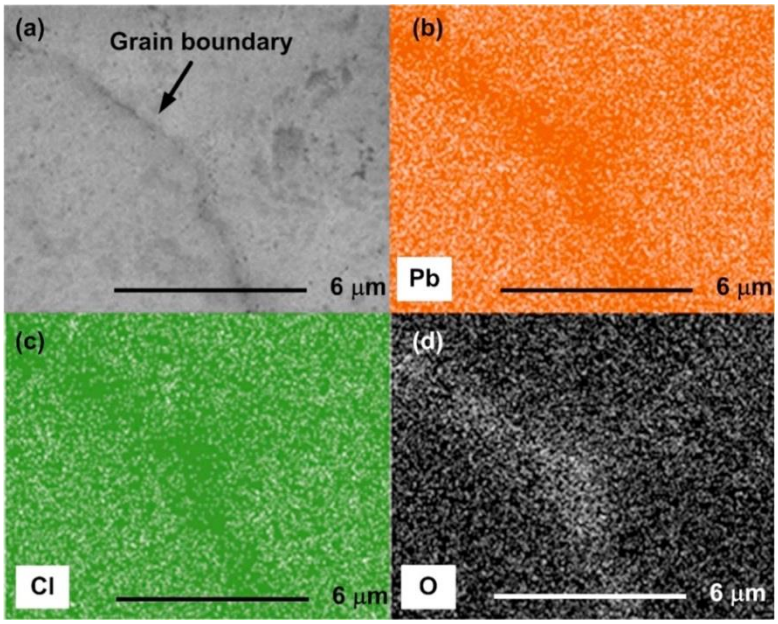

Fig. 15. (a) SEM images of large grain perovskite and corresponding chemical distributions of (b) lead (Pb), (c) chlorine (Cl) and (d) oxygen (O) that were measured by EDS mapping [15].

Fig. 16 shows the quantitative analysis of the variations of the chemical components of perovskites as functions of grain sizes and the positions of perovskites. In this study, the controlled grain sizes of perovskites ranged from a few micrometers to ~60 μm in Fig. 16 (a)-(c). The quantitative atomic percentage of $MAPbI_{3-x}Cl_x$ for representative areas in Fig. 16 (a) and (b) was analyzed and listed in Table 1. Interestingly, the density of chemical compositions (C, Pb, Cl and I) of perovskites at the GIs is gradually reduced when the grain sizes of perovskites were reduced, as shown in Fig. 16 (d). Notably, a higher atomic percentage (5%) of Cl was found with enlarged grain size (60 μm) perovskites, which is contrasted with a negligible amount (<1%) of Cl for smaller grain perovskites. Note that Cl-doping is a common technique for achieving higher open circuit voltage and long diffusion lengths of perovskite solar cells [111,112,113]. Despite intensive studies to increase the Cl content, the control of the Cl content in perovskite is extremely difficult,

resulting in the negligible content of Cl in perovskites [111,112,113]. As demonstrated, our study suggests a novel way to tune the Cl content by controlling the grain sizes of perovskite using a hot-casting technique. We also found that the grain size of perovskite influenced the (Cl+I)/Pb ratio, as shown in Fig. 16 (e). For instance, for smaller grain (~4 μm) perovskites, the GIs yielded a ratio of Pb to (Cl+I) close to 1:2.3 while the larger grain perovskites led to stoichiometric values of ~ 1:3. It suggests that the enlarged grains of perovskites have excellent chemical structures. In addition, it is found that the distributions of chemical compositions were quite distinct, especially at the GIs and GBs of perovskites. Fig. 16 (f) illustrates the variations of chemical compositions across the perovskites, showing a gradual decrease in the chemical components (C, Pb, I, Cl) of $MAPbI_{3-x}Cl_x$ from the GIs to the GBs while clearly illustrating a drastic increase in oxygen at the GBs.

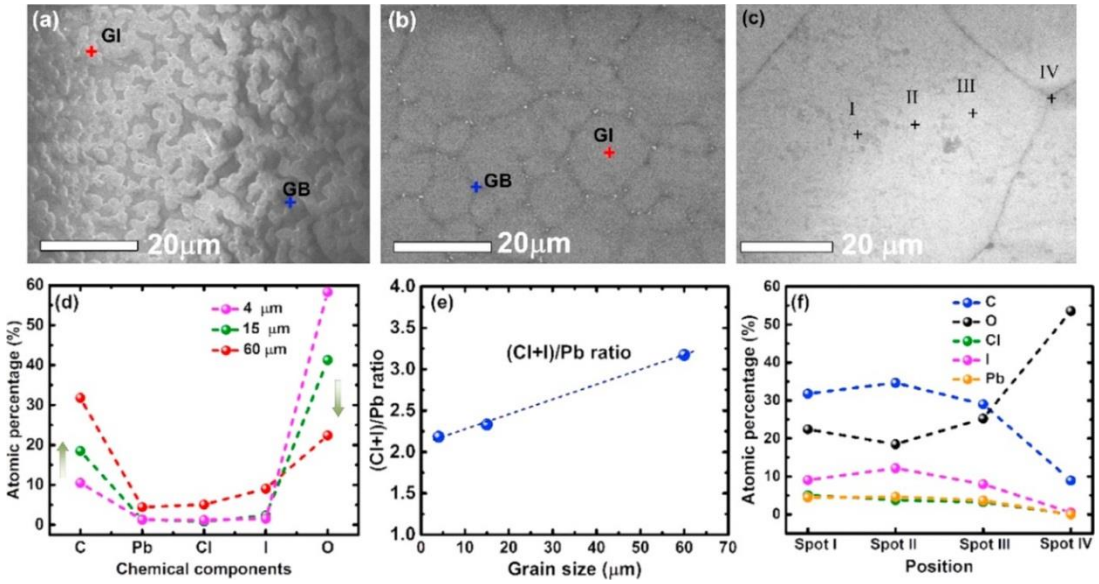

Fig. 16. SEM images of (a) small (~4 μm), (b) medium (~15 μm) and (c) large (~60 μm) grain perovskites. (d) Atomic percentage of chemical components (C, Pb, Cl, I, O) and (e) (Cl+I) to Pb

ratio at the GIs as functions of grain sizes and the positions of perovskites. (f) Atomic percentage of selected areas of I, II, III, and IV across large (~60 μm) grains [15].

Table 1. Atomic chemical percentage of selected chemical components of small (~4 μm) and medium (~15 μm) perovskites of Fig. 16 (a) and (b). Other chemical elements such as Na, Mg, Al, Si, S, Ka, and Ca were detected but not shown here.

	100 °C hot-casting perovskite		**180 °C hot-casting perovskite**	
	Grain Interior (GI)	Grain Boundary (GB)	Grain Interior (GI)	Grain Boundary (GB)
C	9.79		19.64	12.85
O	58.28	66.44	41.95	53.64
Pb	0.97	0.47	1.14	0.37
Cl	1.21		0.71	
I	1.01	0.34	1.91	0.43

To quantitatively examine chemical distributions between the GIs and GBs, the representative areas in Fig. 16 (a) and (b) were further analyzed. In particular, the GIs and GBs showed three distinct discrepancies. First, it is found that the chlorine was absent at the GBs for both smaller and larger grain perovskites, which provides critical insight into the nature of grain boundaries. This is because the presence of Cl in $MAPbI_3$ plays a critical role in mitigating the formation of defects, but yielding a long diffusion length of charge carriers in perovskites [111,112,113]. The absence of Cl at the GBs suggests that the GBs are more defective and yield shorter diffusion lengths of charge carriers when compared with the GIs. As reported, the reduction mechanism of Cl in perovskite films was attributed to the release of gaseous CH_3NH_3Cl through an intermediate phase reaction during thermal annealing [111]. In our case, since the GBs are

characterized by disordered structures, it is reasonable to assume that the disruptive chemical structures at the GBs will have weakly bonding chemical configurations and thereby promote the release of gaseous CH_3NH_3Cl during the hot-casting processes. Additionally, the smaller radii of Cl compared to those of Pb and I might also enhance the depletion of Cl at the GBs, resulting in the absence of Cl at the GBs. Second, the GBs are characterized by non-stoichiometric PbI_x and $MAPbI_x$ for smaller and larger grain perovskites, respectively. Note that the incomplete coverage of perovskites was also observed for smaller grain perovskites. Our EDS measurements indicated Pb/I ratios of ~1:0.7 and 1:1.2 for PbI_x and $MAPbI_x$ at the GBs, largely deviating from a stoichiometric ratio of 1:3, indicating a higher density of iodide vacancy. Therefore, the dominant defects at the GBs were the iodide vacancy (V_I) for both perovskites. Third, a higher atomic concentration of oxygen at the GBs, compared to the GIs, is found, as shown in Fig. 17. Note the level of oxygen at the GBs was similar regardless of the grain sizes of perovskites, while the oxygen contents at the GIs were decreased with increased grain sizes, indicated in Fig. 17. An increase in oxygen concentration at the GBs might be related to the iodide vacancy in which the Pb cations attract oxygen anions to compensate the iodide anion deficiency. Based on our measurements, it is likely that the GBs are characterized by an absence of chloride, a number of iodide vacancies (V_I), and a higher concentration of oxygen. In contrast, the GIs showed better structural compositions of perovskite, showing the stoichiometric $MAPbI_{3-x}Cl_x$.

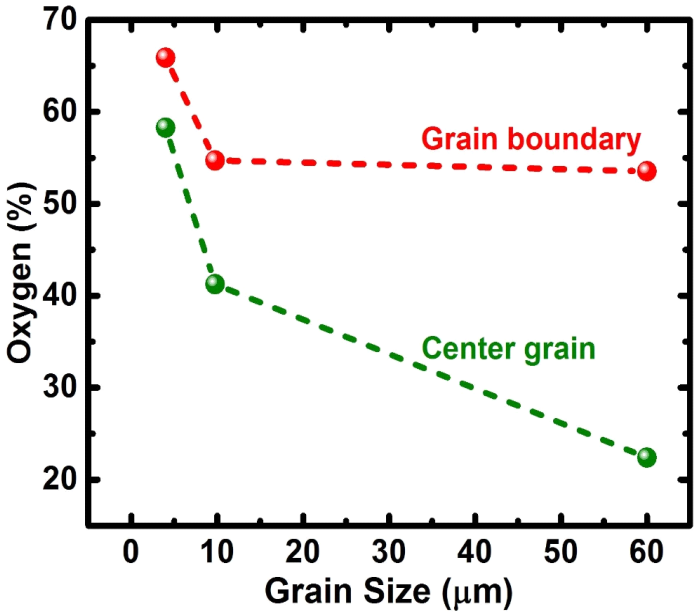

Fig. 17. Atomic percentage of oxygen as functions of grain sizes at the center grain and grain boundaries [15].

4.4 Two dimensional (2D) photoluminescence mapping of smaller and larger grain perovskite film

To investigate the local variation of chemical compositions of perovskites on the optical properties of perovskite, steady-state PL and time-resolved lifetime mapping were performed. Fig. 18 shows high-resolution PL spatial mapping that correlates topologies to emission spectra of $MAPbI_{3-x}Cl_x$. For the PL and lifetime mapping, poly(methyl methacrylate) (PMMA) was coated on top of the perovskite as the protective layer from moisture and/or atmospheric oxygen. In particular, it has been proved that PMMA polymer as an optically transparent material exhibited a higher stability under irradiation [59]. Without PMMA coating on perovskite films, it is found the PL intensities and lifetimes gradually varied during 2D mapping due to photo-degradation. A laser

diode (λ_{exc} = 405 nm) was used for optical excitation of the PL mapping, which was scanned over an area of 20 μm × 20 μm of perovskites. The excitation power of 0.2 μW/cm^2 was used to avoid the degradation by a laser diode, and spatially integrated emission spectra ranging from 680 to 815 nm were collected. We note that the PL images are consistent with microscopic morphologies which depict a higher contrast at the GBs and suggest significant differences in optoelectronic properties between the GIs and GBs. Overall, the PL intensity of a larger grain perovskite, Fig. 18 (a), is approximately 10 times stronger than that of a smaller grain perovskite, Fig. 18 (c). This suggests that a larger grain perovskite possesses better optical quality. Based on 2D PL mapping, it was found that the GBs for both perovskites were characterized by the strong PL quenching at the GBs, which could be in part attributed to non-radiative trap centers. In addition, it is found that emission spectra were gradually blue-shifted towards the GBs and had an abrupt blue-shift at the GBs, as shown in Fig. 18 (e) and (f). An increase in chemical inhomogeneity towards the GB might be responsible for the non-radiative PL and the blue-shift in PL peaks. Note, a blue-shift towards the GBs suggests a gradual broadening of the energy bandgap from GIs towards GBs and an abrupt broadening of the energy bandgap at the GBs.

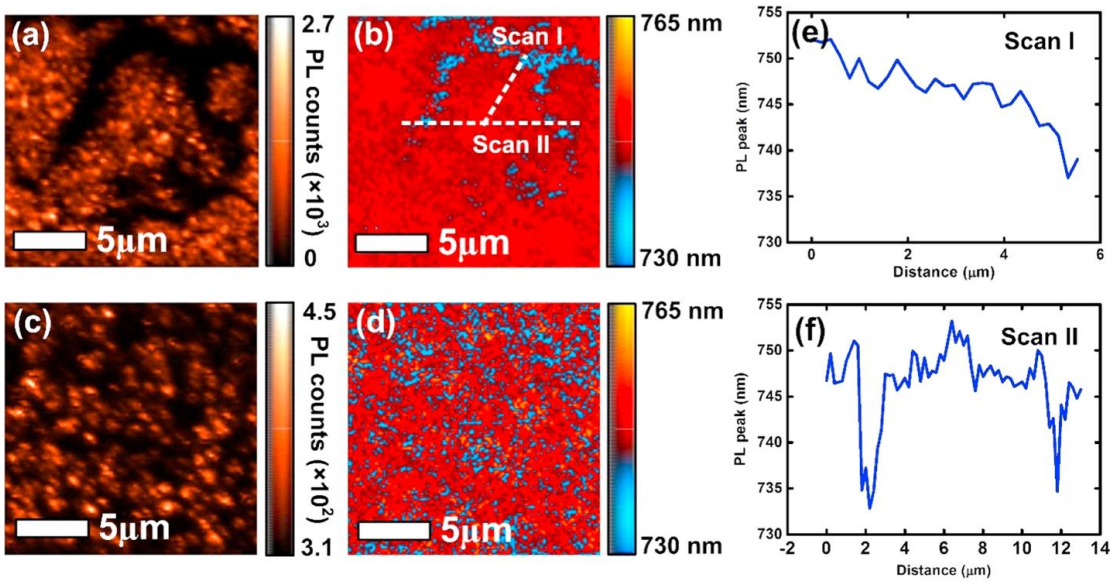

Fig. 18. High-resolution photoluminescence (PL) confocal microscopic images and PL intensity spatial mapping that correlate topologies to emission spectra of $CH_3NH_3PbI_{3-x}Cl_x$. (a) and (c) Microscopic image, (b) and (c) corresponding PL intensities of large and small grain perovskites, respectively. (c) and (f) PL mapping showing the blue-shift of emission peaks at the GB for a large grain perovskite shown in (b) [15].

4.5 Two-dimensional (2D) time resolved photoluminescence (TRPL) mapping of smaller and larger grain perovskite film

To get deeper insight into the recombination kinetics of perovskites, time-resolved PL mapping was investigated with a confocal microscope at a nanoscale resolution of ~380 nm, which allows for spatially resolving recombination kinetics at the GIs and GBs. In this case, the perovskites were excited with a 405 nm pulsed laser (pulse width down to 60 ps, repetition rate 50 MHz). Fig. 19 shows the lifetime mapping of perovskites that are clearly distinguishable between the GIs and the GBs. By quantitatively analyzing the lifetimes across the grains, the average

lifetimes for smaller and larger grain perovskites at the GIs, were estimated about ~ 1.8 and 2.5 ns, respectively. Interestingly, a smaller grain perovskite produced a slightly longer lifetime at the GIs by ~1.4 times than that of a larger grain perovskite. Note that Nie *et al*. [109], reported a similar observation in which a smaller grain perovskite yielded the longer effective carrier lifetime but smaller diffusion constants of minority carriers than that of a larger grain perovskite, emphasizing the disordered and defective natures of a smaller grain perovskite. The carrier lifetime distribution in Fig. 19 was further analyzed by contrasting four different transient regions highlighting the hot-spot (donated by red region A), the GI (yellow region B), the area adjacent to the GBs (light blue region C) and the GB (dark blue region D), respectively. Interestingly, hot spots within the grain interiors showed longer lifetimes compared to the surrounding regions for both perovskites as highlighted in Fig. 19 (c) and (f). Approaching the GBs, i.e. approaching from hot-spot A to B to C and to D regions, the lifetimes of both perovskites gradually decreased, indicating the non-radiative characteristics towards the GBs. Such variations of lifetimes are closely correlated to the localized chemical variations and the evolution of non-stoichiometric perovskites towards the GBs.

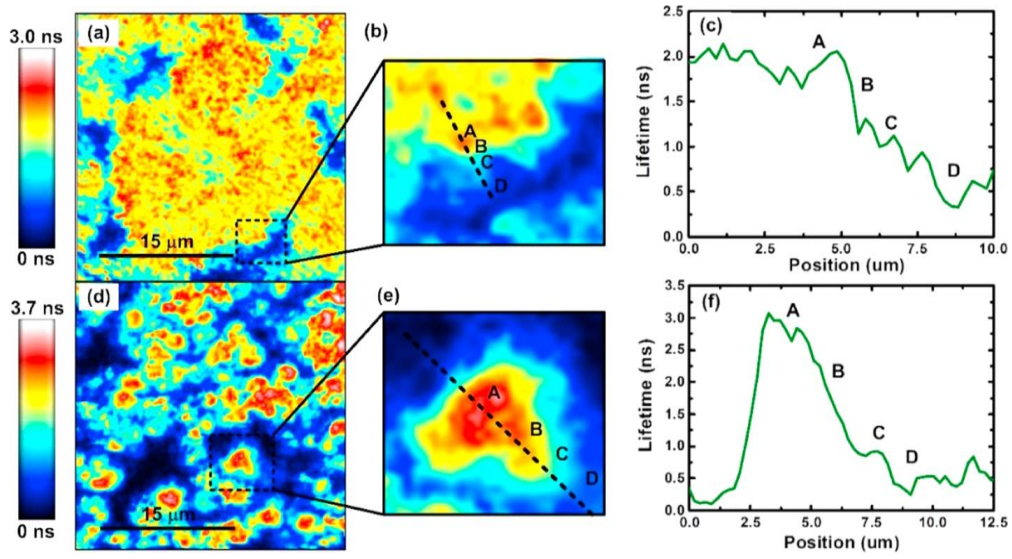

Fig. 19. Lifetime mapping of hot-casting perovskites that are clearly distinguishable between the GIs and the GBs. (a) and (d) Time resolved 2D lifetime mapping, (b) and (e) magnified selected lifetime mapping and (c) and (f) corresponding lifetime values as a function of positions for large and small grain perovskites, respectively [15].

4.6 Plausible recombination mechanism at GB

Since the defect with deep levels can only be responsible for non-radiative recombination, the V_I one of dominant defects found from our EDS measurements, must have deep defect levels instead of shallow transition energy level. Recently, Agorgousis *et al*. [102], suggested that the deep-level of defect state V_I can be formed when the Fermi energy is close to the band edge. Otherwise, the formation energy of deep-level V_I defects is very high, so that it is unlikely to form deep defects, but leads to the shallow-level of V_I defects. However, there will be much possibility that an incorporation of a higher concentration of oxygen at the GBs might shift the position of Fermi energy level close to conduction band. As a consequence, the modification of Fermi level

is likely to lower the formation energy of V_I defects that have the deep-level of defect states and serve as trap-assisted recombination centers at the GBs. Indeed, a recent experiment demonstrated that the incorporation of H_2O as an n-type dopant shifted the Fermi energy level of the perovskites close to the band edge [114]. Thus, the GBs will contain the deep trap states which might serve as recombination centers. Nevertheless, the GBs might not act as high recombination sites for charge carriers due to the favorably energy bandgap configuration of nonstoichiometric $MAPbI_x$ or PbI_x at the GBs, as shown in Fig. 20. As observed from PL mapping, $MAPbI_x$ or PbI_x at the GBs will have a larger energy bandgap than that of GIs. Given the larger energy bandgap of these materials, they would result in a type I band offset, previously measured by ultraviolet photoemission spectroscopy (UPS) [106]. If such energy bandgap alignment is formed, its beneficial effect would form energy barriers that will prevent charge carriers from the traps states at the GBs, thereby greatly reducing the recombination rates at the GBs. It should be noted that the grain boundary of $Cu(InGa)Se_2$ and Cu_2ZnSnS_4 solar cell materials has broadening or band bending of the band gap, consequently leading to the suppression of the photogenerated charge carriers at the GBs [115,116,117]. Therefore, the benign characteristics of the GBs of perovskites observed from many experimental measurements could be originated from a favorable larger energy bandgap alignment at the GBs, even though the $MAPbI_x$ or PbI_x formed at the GBs is defective and contains deep trap centers.

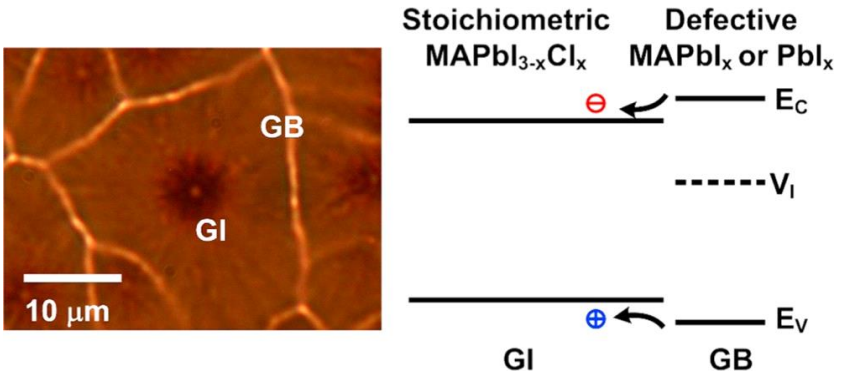

Fig. 20. Energy bandgap profile in perovskites outlined, based on the chemical and optical characteristics of EDS, PL and time resolved lifetime measurements. The larger bandgap of PbI_x or $MAPbI_x$ at the GBs was formed and had a favorable bandgap alignment, thereby greatly reducing the recombination rate of photogenerated charge carriers at the GBs [15].

4.7 Summary

We have systematically investigated GIs and GBs of perovskite film using chemically, spatially, and temporally resolved measurements. Irrespective of grain size, GBs has non-stoichiometric ratio of PbI_x and $CH_3NH_3PbI_x$ with enriched oxygen concentration, an absence of chlorine and an increased amount of iodine. Indeed, it has been found from 2D PL lifetime mapping that GB has deep defect centers due to non-radiative characteristics. Also, there has been bandgap broadening observed at GB which is a benign characteristic of GB. Due to bandgap broadening, charge carrier is repelled from GB and lower recombination might occur at GBs. In the next chapter, we will fabricate perovskite solar cells using different grain sizes to show the effect of GBs in the photovoltaic performance.

CHAPTER 5

NEW DECONVOLUTED PL APPROACH TO PROBE THE CHARGE CARRIER DYNAMICS OF THE GI AND GB

5.1 Introduction

Perovskite solar cells (PSCs) have emerged as a promising candidate in the field of photovoltaic technology and have shown remarkable energy conversion efficiency improvement within a short period [26,41]. However, there are still some issues such as long-term stability, hysteresis, and defects in perovskite films [91,118,119]. In particular, there has been controversy about the nature of the grain boundary (GB), [40,105,120,121] which plays a decisive role in the solar cell performance. The GBs of perovskite solar cells have been examined by using nanoscale characteristic tools including Kelvin probe force microscopy (KPFM), conductive atomic force microscopy (c-AFM), electron beam-induced current (EBIC), and confocal microscopy [40,105,120,121,122]. To date, based on KPFM, c-AFM and EBIC measurements, the benign characteristic of GBs has been reported [105,120], providing effective charge separation and collection at grain boundaries, which results in a higher photocurrent. However, according to confocal microscopy measurements [40], the grain boundaries are characterized by a source of nonradiative recombination centers with lower PL intensity and faster nonradiative decay. In addition, there is controversy about the nature of GBs in theoretical studies [102]. First principles calculation studies performed by Yin, *et al.* [101] showed that GBs are benign because they do not produce deep defect states. On the other hand, Agiorgousis, *et al.* [102] also conducted the same first principles calculations but reported that Pb cations and I anions were strongly covalently

bonded by the formation of Pb dimers and I trimers, which led to the formation of deep defect states within the band gap. However, in spite of the experimental and theoretical controversies about GBs, there is agreement on the positive effect of increased grain size on the reduction of notorious hysteresis and improved performance of perovskite solar cells [84,109]. This suggests that controlling the grain size and GBs is important for achieving a reliable and high energy conversion efficiency of perovskite solar cells. In this regard, it is important to develop a rapid method for measuring the nature of GBs that can provide timely feedback to modify the processing methods and conditions of the perovskite film. However, the prevalent method of studying the effect of GBs relies on nanoscale equipment, including KPFM, c-AFM, EBIC, confocal microscopy, etc. that limits the flexibility of experiments due to sample preparation and time consuming processes. In this paper, a comprehensive new method of simultaneously probing both grain interiors (GIs) and GBs of $CH_3NH_3PbI_{3-x}Cl_x$ perovskite films is introduced using well-established, regular photoluminescence (PL) measurements. In particular, we were able to resolve the PL spectra which were typically asymmetric and deconvoluted with a bi-Gaussian function representing the ordered and disordered phases of the perovskite film. Quantitative analysis of two-dimensional (2D) PL mapping using confocal microscopy revealed that the ordered PL spectra originated from GIs whereas the disordered PL spectra mainly came from GBs. The systematic analysis of the ordered and disordered PL spectra provided deep insight into the recombination processes of the GIs and GBs of perovskite films. Remarkably, we found that the GIs showed exciton-like recombination processes regardless of grain size. However, the recombination process of the GBs was largely dependent upon the size of the grains which induced nonradiative recombination or exciton-like transition. We also correlated the performance of perovskite solar

cells with perovskite morphology. In particular, higher efficiency perovskite solar cells were achieved with a larger grain size while much lower efficiency was achieved with smaller grains.

5.2 Deconvoluted PL approach to separate GI and GB

Fig. 21 shows the photoluminescence (PL) spectra of $CH_3NH_3PbI_{3-x}Cl_x$ ($MAPbI_{3-x}Cl_x$) perovskite thin films that were measured using a Horiba FluoroLog-3 spectrofluorometer. The perovskite film was excited by a 450 nm solid-state laser that had a beam spot size of about 25 mm. The perovskite film was prepared on a glass slide using a hot-casting technique. A scanning electron microscope (SEM) image of the perovskite film is also shown in Fig. 21. The perovskite film exhibits PL peak positions at 760 nm within the sharp absorption range associated with the band edge observed in the range from 730 nm to 790 nm.

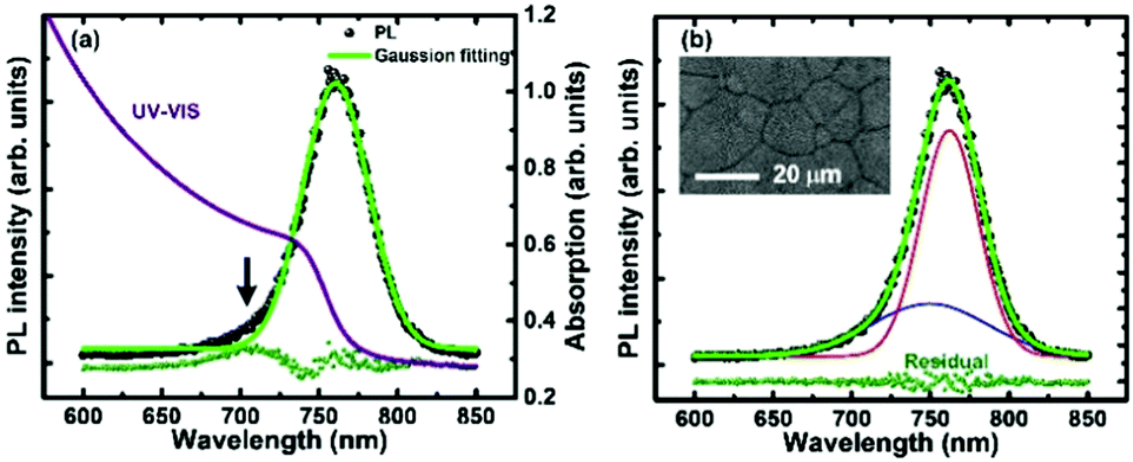

Fig. 21. (a) Absorption and PL of $MAPbI_{3-x}Cl_x$ that was fitted by a single Gaussian function and (b) PL spectrum fitted by a bi-Gaussian function. Residual values are also displayed at the bottom of each figure. The inset shows a SEM image of the perovskite film used for PL measurement. Reproduced by permission of the PCCP Owner Societies [16].

A close examination of the PL spectra in Fig. 21 (a) indicates that the PL spectral line is asymmetric and cannot be fitted into a single Gaussian function. Analysis of the residual plot showed that a larger residual value was observed on the short wavelength side indicated by an arrow. However, when the PL spectra are fitted by a bi-Gaussian function, the residual value was significantly reduced, as shown in Fig. 21 (b). In particular, the deconvoluted PL spectra in Fig. 21 (b) contain two distinct emission peaks. One has a broad full-width at half maximum (FWHM) of 86.8 nm but a shorter wavelength of 749.5 nm whereas another PL spectrum showed a narrow FWHM of 43.5 nm but a longer wavelength of 762.1 nm. Recently, the deconvoluted PL spectra were described as the ordered and disordered phases of perovskite films [123], represented by longer and shorter wavelengths, respectively. However, the origin of the disordered phase of perovskite films has not been identified.

5.3 Origin of ordered and disordered phase by 2D PL mapping

To further investigate the origin of the ordered and disordered phases of PL, two dimensional (2D) PL mapping was performed using confocal spectroscopy (NTEGRA spectra, NTMDT) to probe spatially resolved PL spectra at the nanoscale level. Our confocal spectroscopy has an in-plane spatial resolution of ~380 nm which was achieved by an objective lens with a numerical aperture of 0.7 and a 405 nm solid-state laser. Fig. 22 (a) shows the 2D PL intensity of the perovskite film, where the grain boundary exhibited strong PL quenching. In addition, the analysis of 2D spectral PL mapping in Fig. 22 (b) shows a dominant PL peak of ~750 nm at the GIs but an abrupt blueshift of PL at the GBs (denoted by blue color in the 2D PL map). It should be noted that some dark spot regions in the intensity map in Fig. 22 (a) are larger than the sizes of the blue-shifted PL spectra in Fig. 22 (b). However, it is clearly shown that the blue shifted PL

spectra are located in the dark spot region when the intensity and spectral PL maps overlap, as shown in Fig. 22 (c). In addition, the high magnification SEM image in Fig. 22 (d) indicates that the pinholes are partially covered by perovskite islands. This suggests that blue-shifted PL spectra originated from a number of small perovskite islands located in the dark region. Interestingly, confocal PL spectra from the GI and GB can be fitted by a single Gaussian function but not by a bi-Gaussian function, as shown in Fig. 22 (e) and (f). We found that the PL at the GBs showed a relatively lower intensity and a shorter wavelength while the GIs showed a higher intensity and a longer wavelength. This is reminiscent of the deconvoluted ordered and disordered PL spectra obtained from typical (or non-confocal) PL measurements in Fig. 21. Therefore, it is inferred that the disordered phase of the PL spectrum in Fig. 21 mainly originated from the GBs whereas the ordered phase PL spectra came from the GIs. However, we cannot exclude the possibility of the contribution of the disordered phase from the GIs which contain chemical disorder within the GIs. Previously, we reported 2D PL and chemical mapping studies [15] on perovskite films with various morphologies and grain sizes. The grain size of perovskite films varied from a few micrometers to over 50 micrometers. In particular, the smaller the grain size, the more the non-stoichiometric chemical composition of the perovskite film was observed. Critically, chemical analysis of controlled morphologies [15] revealed that non-stoichiometric chemical disorder increased towards the GBs. In addition, the blue-shift of the PL spectra was increased towards the GBs while the GIs showed very uniform but longer wavelengths. Remarkably, the GB was found to consist of Pb-rich $CH_3NH_3PbI_x$ or PbI_x with high oxygen concentration. Our observation is in good agreement with recent electron energy loss spectroscopy (EELS) studies that revealed iodine deficiency, that is, Pb-richness at the GBs [122]. Note that pure PbI_2 will have an energy bandgap of 2.3 eV [106] while the stoichiometric $CH_3NH_3PbI_{3-x}Cl_x$ has an energy bandgap of 1.66 eV.

Therefore, the GBs consisting of Pb-rich $CH_3NH_3PbI_x$ or PbI_x will have a relatively larger energy bandgap than the GIs. In particular, it is found that the larger energy bandgap material at the GBs has a type I alignment with the lower bandgap material of the GIs [106]. Such band alignment is also shown in the inset of Fig. 22 (f). Rationally, the shoulder peaks of shorter wavelengths from the deconvoluted PL spectra in Fig. 21 cannot be explained by defect-mediated PL transitions from the GIs but should originate from the bandgap broadened GBs.

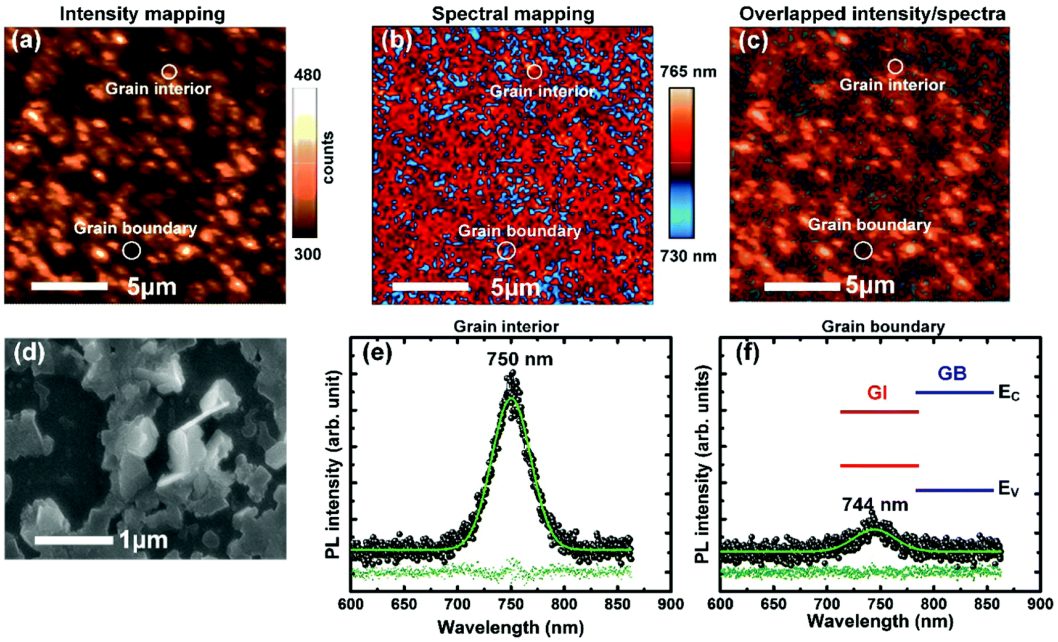

Fig. 22. (a) Two-dimensional (2D) PL intensity, (b) spectral mapping, and (c) overlapped intensity/spectral PL mapping showing that the blue-shifted PL spectra are located in the dark spot region. (d) High magnification SEM image shows that the pinholes are partially covered by a number of perovskite islands. In addition, PL spectra from (e) the grain interior and (f) the grain boundary were fitted by a single Gaussian function. This inset of (f) shows a type I alignment of energy band gaps between the GI and GB. Reproduced by permission of PCCP Owner Societies [16].

5.4 Grain size dependent recombination mechanism at GIs and GBs

As shown, the confocal PL mapping approach provides valuable insights into local PL variations at the nanoscale level but is a time-consuming process. However, the typical (or non-confocal) PL approach using a laser with a larger beam diameter can provide prompt measurements capable of probing the optical properties of the GIs and GBs at the same time. For instance, deconvoluted PL measurements can be used as a metric to promptly and simultaneously assess the nature of the GIs and GBs including charge carrier dynamics from an analysis of the power-dependent PL measurements, described below. This PL approach can promptly provide feedback on the optical quality of both GIs and GBs. For this study, we intentionally fabricated defective perovskite films with smaller grains and high-quality perovskite films with larger grains, as shown in Fig. 23. Specifically, we have fabricated $CH_3NH_3PbI_{3-x}Cl_x$ films with three different grain sizes ranging from 1–2 μm to 10–20 μm, and >50 μm, as shown in Fig. 23 (a)–(c). We conducted power dependent PL measurements using a 450 nm laser with a beam size of 25 mm. As shown in Fig. 23 (a)–(c), the perovskite film with larger grains (>50 μm) showed an emission peak at 755 nm (1.66 eV) while a significant blue shift of 26–31 meV was observed for the perovskite films with smaller grains. In addition, we found that the intensity of the perovskite films with a larger grain size was three or six times stronger than those with smaller grain sizes in the range of 10–20 μm or 1–2 μm, suggesting better optical quality for larger grain perovskite films. The PL spectra obtained from excitation-dependent PL for all samples were analyzed by a bi-Gaussian function to investigate the underlying recombination processes of the ordered and disordered phases of perovskite films. Power dependent PL intensity was plotted on a double-logarithmic scale to explain the linearity effect shown in Fig. 23 (d)–(f). The recombination process [124,125] can be elucidated by investigating the change in PL intensity (I_{PL}) and a power index value (β), expressed

as $I_{PL} \propto I_{EX}^{\beta}$. For the free-to-bound recombination and donor–acceptor pair, the power index value will be less than unity, i.e. $\beta < 1$ while for exciton-like recombination the power index value will be in the range of $1 < \beta < 2$. Interestingly, regardless of grain size, ordered phases have power index β values in the range of 1 and 2 which corresponds to exciton like recombination. However, we found that the recombination dynamics of GBs are diverse and strongly dependent upon the grain size. The disordered phase of smaller grain perovskite films with a lower excitation intensity of 120 mW/cm^2 or less exhibited power index values of β = 0.66 and β = 0.92 suggests non-radiative recombination. In contrast, the perovskite film with a larger grain size (>50 μm) showed β = 1.60, which indicates exciton-like recombination. This suggests that the charge carrier recombination at the GBs showed a very strong dependence on the grain size in which the smaller grains showed defect-mediated recombination while for larger grains the exciton-like transition at GBs was observed. In other words, the characteristics of GBs are not stationary but might strongly depend upon the processing conditions that might lead to different degrees of structural disorder, morphologies, and chemical inhomogeneities.

Fig. 23 (g)–(i) shows the evolution of the peak energy, which is indicative of distinct states of ordered and disordered phases of perovskite films. The ordered phases for all samples remained in the same peak position between 1.65 and 1.69 eV regardless of grain size. This confirms that the PL transition of the ordered phase of PL originated from band-edge radiative recombination. This is consistent with the observation of power index values indicating exciton-like recombination. However, for the disordered phase, we observed a gradual blueshift for all samples upon increasing excitation intensity, which is a typical characteristic of defective films [126,127]. However, we observed different transient trends of disordered phases of smaller and larger grain perovskites. For instance, the smaller grain perovskite showed a continuous increase in energy

peak positions upon increased power density, as shown in Fig. 23 (g) and (h). Typically, the shift of the peak position towards higher energy is attributed to the trap filling from a moderately deep level to a shallow energy level. The continued increase in energy peak positions indicates that perovskite films with smaller grains contain a high density of deeper defect states. In contrast, the disordered phase of the larger grain perovskite film in Fig. 23 (i) showed a rapid blueshift and then the energy peak position remained the same. It suggests that larger grain perovskites contain a lower density of defects that quickly saturate with increased power excitation.

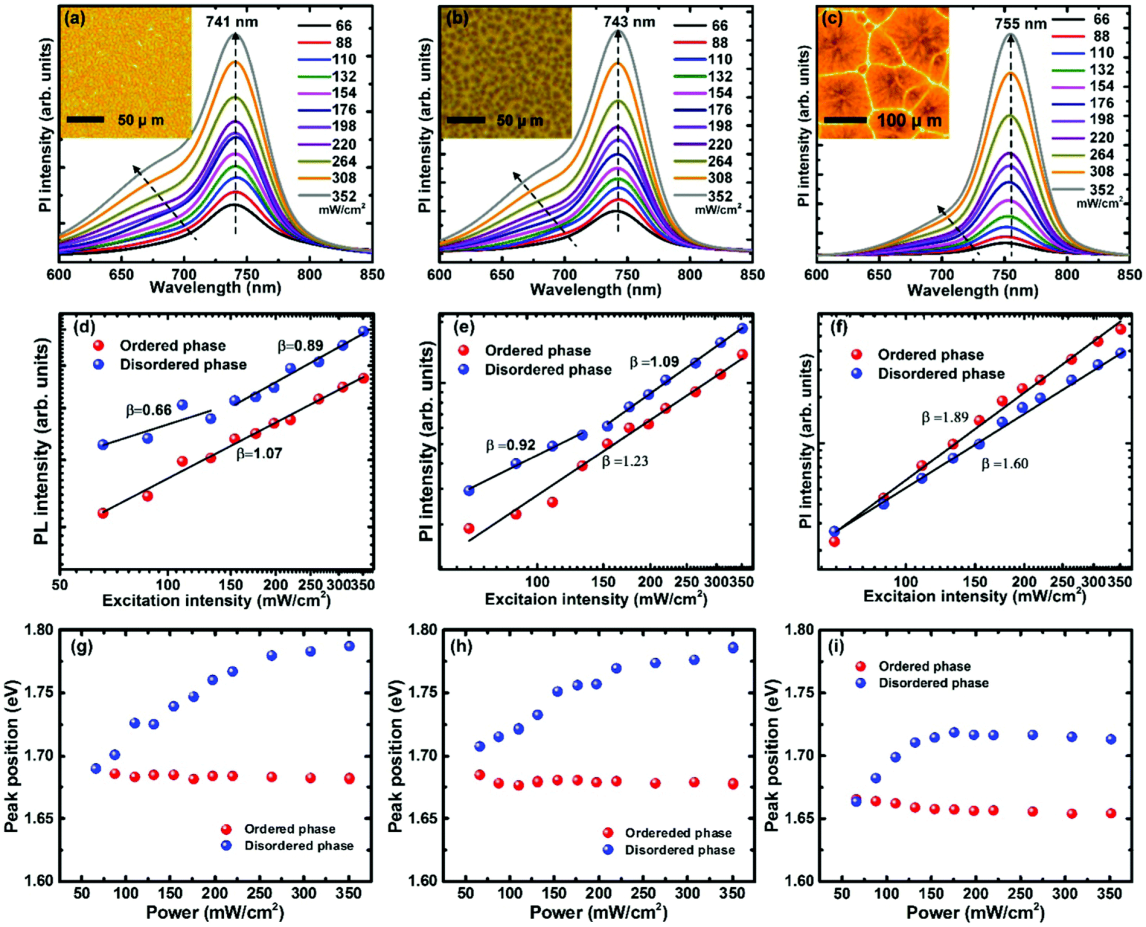

Fig. 23. Power dependent PL spectra excitation intensity of (a) 1–2 μm grains, (b) 10–20 μm grains and (c) >50 μm grain. The insets in (a–c) show the corresponding microscopic images. A

double-logarithmic PL plot for (d) 1–2 μm grains, (e) 10–20 μm grains, and (f) >50 μm grains was used to calculate the power index values. In addition, the evolutions of energy peak position values for (g) 1–2 μm grains, (h) 10–20 μm grains, and (i) >50 μm grains are shown. Reproduced by permission of PCCP Owner Societies [16].

5.5 Grain size dependent current-voltage characteristics

We also investigated the photovoltaic performance by fabricating hybrid perovskite solar cells with different grain sizes composed of FTO/PEDOT:PSS/$MAPbI_{3-x}Cl_x$ /PCBM/Ag, as shown in Fig. 24 (a). Fig. 24 (b) shows the current–voltage (J–V) characteristics under 100 mW/cm^2 illumination using AM 1.5G and the resultant photovoltaic parameters are listed in Table 2. The perovskite solar cells with smaller grains showed energy conversion efficiencies of 2.59% and 9.19%, respectively; however, a dramatic increase in efficiency to 13.72% was observed for the perovskite solar cell with larger grains. An enhanced performance was attributed to improved photovoltaic parameters of short circuit current (J_{SC}), open circuit voltage (V_{OC}) and fill factor (FF). We found that the enhancement of J_{SC} with increased grain size is closely related to an increased light absorption in the range from 400 nm to 600 nm, as shown in Fig. 24 (c). Interestingly, the larger grain perovskite film showed a sharp absorption edge between 700 and 800 nm while the absorption edge of smaller perovskite solar cells was not well defined but gradually decreased. This indicates that perovskite films with smaller grains contain larger chemical disorders which will lead to broader absorption profiles but not sharp absorption edges. Another critical observation is the quenching efficiency of photogenerated charge carries at the PEDOT:PSS/ perovskite interface. Typically, PEDOT:PSS is commonly used as a hole transport

layer (HTL) for perovskite solar cells and relatively higher PL intensity of $MAPbI_{3-x}Cl_x$ with a PEDOT:PSS quenching layer indicates poor quenching efficiency. Fig. 24 (d) shows the comparison of the PL spectra with the PEDOT:PSS quenching layer, showing that the larger grain perovskite showed the lowest PL intensity, indicating the excellent charge extraction efficiency. In contrast, a poor charge extraction efficiency was observed for a perovskite film with smaller grains. This might be attributed to defective perovskite layers that slow down the extraction process of photogenerated charge carriers.

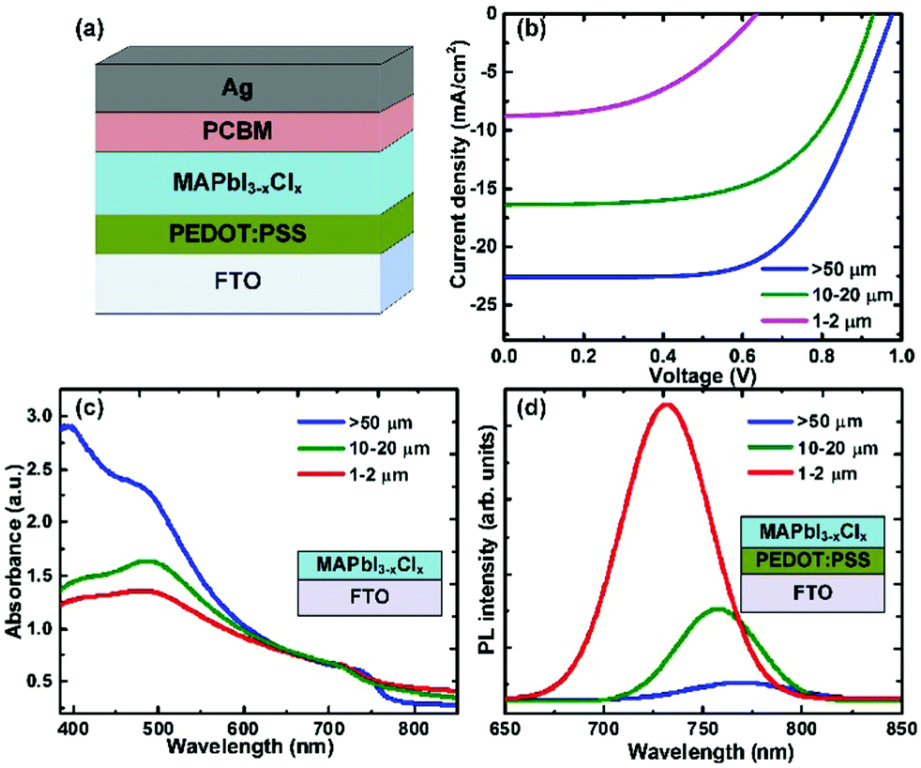

Fig. 24. (a) Device structure of the perovskite solar cell, (b) current density (J)–voltage (V) characteristics, (c) UV/vis spectra and (d) PL spectra for three perovskite/PEDOT:PSS/FTO films with different grain sizes. Reproduced by permission of PCCP Owner Societies [16].

Table 2. Photovoltaic parameters for perovskite solar cells

Grain size	J_{SC}(mA/cm^2)	V_{OC} (V)	FF	η (%)
1-2 μm	8.77	0.63	46.88	2.59
10-20μm	16.39	0.93	60.29	9.19
>50μm	22.59	0.97	62.61	13.72

5.6 Summary

We developed a new characterization technique using deconvoluted PL approach to determine the film quality of perovskite film. PL spectrum can be deconvoluted using a bi-Gaussian fitting. It has been proved that longer wavelength peak originates from ordered phase of GI and shorter wavelength peak originates from the disordered phase of GB. Moreover, the power dependent PL spectra reveal that GB of smaller grain film has a non-radiative recombination while the GI and GB of larger grain film both have an exciton-like recombination. Finally, larger grain PSCs show better performance than smaller grain PSCs; however, these solar cells have hysteresis and interface defects. In the following chapter, we will focus on removing interface defects from PSCs.

CHAPTER 6

INTERFACE ENGINEERING USING NEW PCBM/CARBON BASED ETL

6.1 Introduction

In recent years, hybrid halide perovskite material family has revolutionized the prospects of next-generation photovoltaic technologies [44,68,98], demonstrating a quantum jump to more than 20 % over the past few years. The rapid development of perovskite solar cell was attributed to its excellent electrical and optical properties including long charge carrier diffusion length [59,61], high charge carrier mobility [128,129], high absorption coefficients, [64,130] and unusual defect properties [119]. In the early stage of development, perovskite solar cells used an n-i-p device structure employing an n-type TiO_2 layer as the bottom electron transport layer [44,45,131]. In this structure, a high temperature (>400 °C) sintering process is typically required to ensure high quality TiO_2, which inevitably increases manufacturing costs and lacks compatibility with flexible substrates. In addition, p-type spiro-OMeTAD is generally used as a hole transport layer and suffers from poor crystallinity, low mobility and decomposition [46]. Critically, the n-i-p planar structure is subject to a considerable current-voltage (J-V) hysteresis [82]. Alternatively, inverted p-i-n device structures have been passionately pursued because of negligible hysteresis, low temperature processing and device structure flexibility [53,82]. In this case, poly(3,4 ethylenedioxythiophene): poly(styrenesulfonate) (PEDOT:PSS) was used as a hole transport layer while fullerene derivatives such as C60, PCBM, and ICBA were investigated as an electron transport layer (ETL) [52,53,132]. Among them, PCBM is widely used as an ETL due to its high electron accepting property and its role as a trap passivation in the perovskite film [52,53]. In

particular, the double ETL composed of PCBM/C60 has been highly pursued because of increased conductivity, trap passivation capability, and quenching efficiency [132,133]. Recent studies revealed that shallow defects were passivated by PCBM while deep traps with a trap depth greater than 0.5 eV were passivated by C60 [133]. However, high-purity C60 is relatively expensive because it must be synthesized using raw chemical materials and high temperature process [134,135]. Alternatively, carbon is abundantly available in nature and relatively inexpensive, which can have a great potential for replacing expensive C60 for perovskite solar cells. Recently, carbon has been used as a hole transport layer or a counter electrode for perovskite solar cell [136]. This is because the work function of carbon (~5 eV) [49] is well aligned with the highest occupied molecular orbit (HOMO) of perovskite (~5.4 eV). In particular, the deep work function of carbon as an ETL in Fig. 25 will result in a small built-in voltage of the perovskite solar cell. However, when carbon is combined with PCBM ETL, photogenerated electrons will be directed by the work function difference between PEDOT:PSS and PCBM. To demonstrate the effectiveness of carbon as a new electron transport material for the perovskite solar cell, we were able to deposit ultra-flat carbon on the top of PCBM using electron beam irradiation method. We also compared the effectiveness of PCBM/carbon with PCBM/C60 ETL for photovoltaic performance of $CH_3NH_3PbI_{3-x}Cl_x$ ($MAPbI_{3-x}Cl_x$) perovskite solar cells. Remarkably, the power conversion efficiency of the PCBM/carbon based perovskite solar cell was raised to 16% from 14%, compared to perovskite the solar cell fabricated with PCBM/C60 ETL. The splendid performance was attributed to the reduction of interfacial defects and improved series and shunt resistance of perovskite solar cells while the quenching efficiency of PCBM/carbon was comparable to that of PCBM/C60.

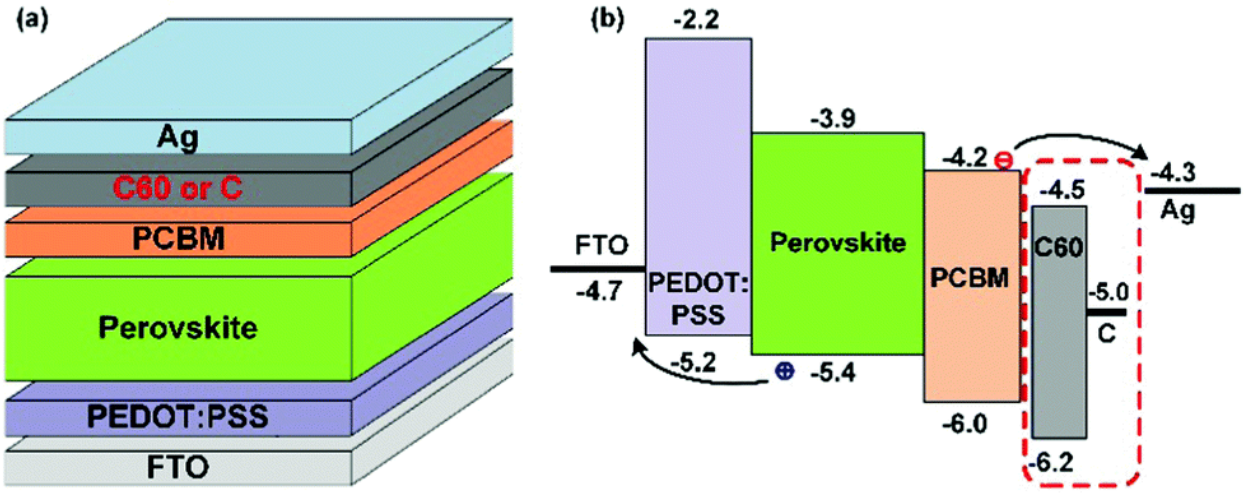

Fig. 25. (a) Schematic of perovskite solar cell with electron transfer layer if C60 or carbon and (b) corresponding energy levels of each layer. Reproduced by permission of PCCP Owner Societies [17].

6.2 Fabrication and electrical characterization of Carbon film

One of the critical challenges is to achieve controlled deposition of carbon layer on top of soft perovskite film. PCBM can be typically coated on the perovskite film by spin-casting PCBM dissolved in dichlorobenzene [132,133] while C60 thin film can be typically deposited through thermal evaporation on the top of perovskite/PCBM layer [137,138]. Currently there is no report regarding the uniform deposition of carbon films on perovskite layer while not disturbing perovskite layer, thereby requiring relatively low temperature deposition. In particular, the precise control of the thickness of carbon is required for effective electron transport. Currently, several methods have been reported for the fabrication of thin-film carbon including ink printing [139], high-temperature chemical vapor deposition (CVD) [136], sputtering [140], and electron-beam irradiation methods [141,142]. We report here a method for depositing high-purity carbon films

using e-beam irradiation in which electron beam generated from a filament and steered to strike graphite rods or flakes. Due to the nature of the deposition and the use of a high-purity carbon source, the e-beam deposited carbon will be highly pure and easily mass-produced. This approach allows one to precisely control thickness of the graphite layer by simply controlling the e-beam exposure time. Graphite (Aldrich) placed in a graphite e-beam crucible was irradiated by e-beam in a high vacuum of ~10^{-7} torr at room temperature. Fig. 26 (a) and (b) show the high-resolution scanning electron microscopy (HR-SEM) images of 50 nm thick carbon film on glass slide, showing an exceedingly flat surface. At the higher magnification in Fig. 26 (b), carbon film had a densely-packed morphology of an exceedingly flat surface of carbon film composed of small grains with grain size of ~30 nm. Also, a 50 nm thick carbon film on top of $MAPbI_{3-x}Cl_x$/PCBM layer was deposited and showed the sharp interface, as shown in Fig. 26 (c). A four-point probe and Hall effect measurements were used to measure the sheet resistance and mobility of the carbon films. Hall Effect measurement of carbon film showed the mobility of ~0.2 cm^2/V.s which is a little lower to the reported mobility of C60 (1.6 cm^2/V.s) but is better than that of PCBM (6.1×10^{-2} cm^2/V.s) [132]. We also deposited an ultrathin ~10 nm thick carbon film whose thickness is typically used for the electron transport layer. Our measurement indicates that the conductivity of ~10 nm thick carbon film was measured to be $\sigma = 4.24\pm0.68$ Scm^{-1} which is much better than reported conductivities of C60 (2.4×10^{-3} Scm^{-1}) and PCBM (3.2×10^{-4} Scm^{-1}) [132].

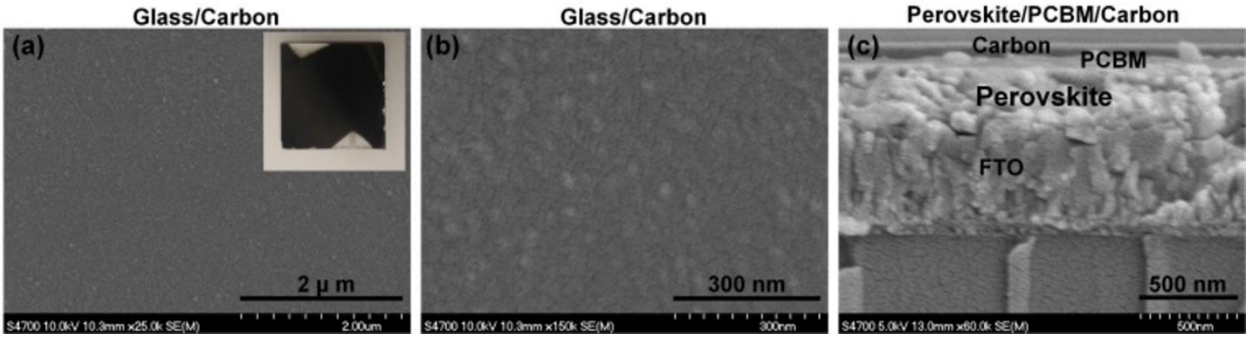

Fig. 26. SEM images of 50 nm thick carbon on glass slide with (a) lower, and (b) higher magnification and (c) cross-section view of FTO/$MAPbI_{3-x}Cl_x$/PCBM/carbon. Reproduced by permission of PCCP Owner Societies [17].

6.3 Morphology of carbon and C60 on top of perovskite film

Fig. 27 shows morphologies of perovskite films coated with various electron transport layers of PCBM, PCBM/C60, and PCBM/carbon. In this regard, perovskite films were fabricated by using a hot-casting technique [15,109]. In this case, the FTO/glass slide was pre-heated at 180 °C while preheated perovskite solution at 70 °C was spin-casted. Typically, a hot-casting technique resulted in pinhole-free and larger grains, as shown in Fig. 27 (a). However, higher magnification of perovskite films showed that the larger grains were packed with nanoscale grains in Fig. 27 (b). The deposition of ETL slightly modified the surface morphologies. In particular, the spin-casting of PCBM on perovskite film resulted in smoother surface with larger grains, as shown in Fig. 27 (c) and (d). PCBM/C60 layer in Fig. 27 (e) and (f) was covered by densely packed small grains which might be attributed to the fact that the C60 lacks bulky side-chains, leading to densely packed grains. In contrast, the morphology of perovskite film with PCBM/carbon in Fig. 27 (g) and (h) is similar to that of the perovskite/PCBM layer.

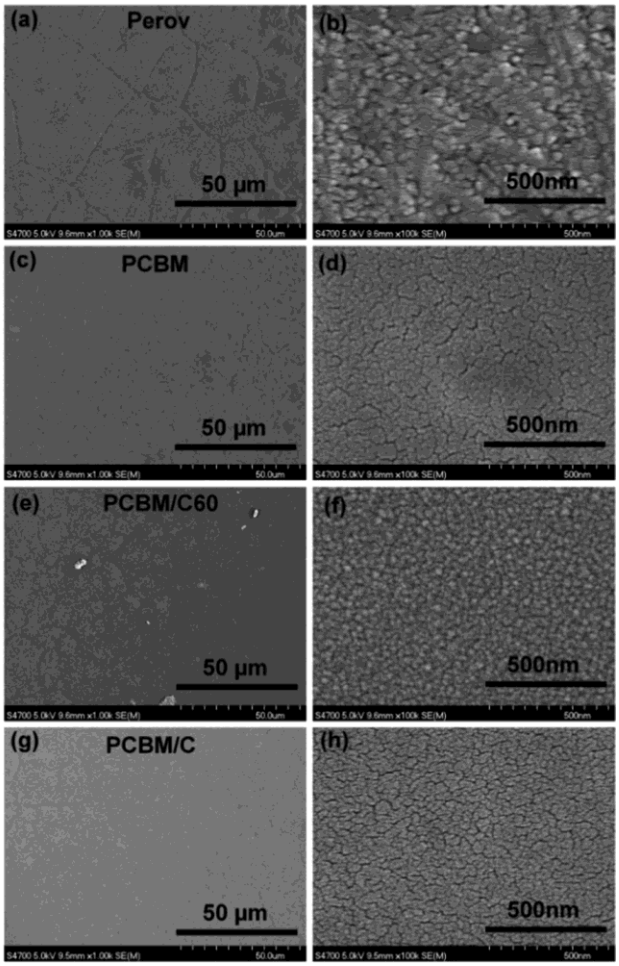

Fig. 27. SEM images of (a-b) perovskite thin film, (c-d) perovskite/PCBM, (e-f) perovskite/PCBM/C60 and (g-h) perovskite/PCBM/carbon film with low and high magnification, respectively. Reproduced by permission of PCCP Owner Societies [17].

6.4 Current-voltage characteristics of PSCs using Carbon and C60

Fig. 28 shows the current-voltage characteristics of p-i-n perovskite solar cells composed of FTO/PEDOT:PSS/$MAPbI_{3-x}Cl_x$ /ETL (PCBM, PCBM/C60 or PCBM/carbon)/Ag with forward (lower → higher voltage) and reverse (higher → lower voltage) scans at a sweep rate of 0.2 V/s. Their photovoltaic parameters are summarized in Table 3. When PCBM was used as an ETL,

larger hysteresis effects were observed, as shown in Fig. 28 (b). One of the proposed reasons for the reduced hysteresis effects was attributed to thermally annealed PCBM that passivated defects at grain boundaries and subsequently eliminated the photocurrent hysteresis [52]. For this study, $MAPbI_{3-x}Cl_x$ solar cells were not thermally annealed due to the thermal degradation of perovskite solar cells [143]. Perovskite solar cell with PCBM ETL showed energy conversion efficiencies of 10.6 and 8.6% with forward and reverse scans, respectively. Remarkably, when PCBM/C60 and PCBM/carbon were used as ETLs, hysteresis effects diminished even though thermal treatment was not performed, as shown in Fig. 28 (c) and (d). In addition, the efficiency of perovskite solar cell with PCBM/C60 improved to ~14% which was due to the improved J_{SC} (22.47 mA/cm^2), FF (0.64) and higher V_{OC} (0.97 V). When PCBM/carbon is used, much higher efficiency of ~16% was obtained. This is attributed to further improved J_{SC} (23.69 mA/cm^2) and FF (0.71) while V_{OC} (0.96 V) values are slightly lower than that (0.97 V) of perovskite solar cells with PCBM/C60 ETL. It is worthwhile noting that use of PCBM/carbon led to significant improvement of fill factor which is very sensitive to the interfacial charge transfer. Therefore, the improved FF of the perovskite solar cell with PCBM/carbon infers that PCBM/carbon ETL might lead to the better interface between perovskite and the PCBM/carbon layer. To further investigate perovskite solar cells, the single-diode mode was used to extract the characteristics of perovskite solar cells that have the relation of the current I and the voltage V, given by the implicit formula [55],

$$I = I_0\left(\exp\left(\frac{q(V - R_s I)}{nV_T}\right) - 1\right) + \frac{V - R_s I}{R_{sh}} - I_{ph} \tag{11}$$

where I_0 is the saturation current, I_{ph} the photocurrent, R_s, the series resistance, R_{sh}, the shunt resistance, n the ideality factor, and q the electron charge. The quantity $V_T = k_B T/q$ is the thermal voltage of the solar cell where k_B is the Boltzmann constant, and T is the cell temperature. The extracted diode parameters were listed in Table 3. As shown, we note the

variations of series resistance (R_s) and shunt resistance (R_{sh}) of perovskite solar cells by applying different ETLs. When the PCBM/C60 layer was applied to the perovskite film, the R_s slightly dropped when compared with the perovskite solar cell fabricated with PCBM ETL. However, the drastic reduction of the R_s was observed when PCBM/carbon was used as an electron extraction layer which was attributed to highly conductive carbon ETL. We also observed a much lower reverse saturation current of the perovskite solar cells with PCBM/carbon than those of the perovskite solar cells fabricated with PCBM only and PCBM/C60. Remarkably, the I_0 dropped from mid 10^{-8} mA to 1.5×10^{-8} mA when PCBM ETL was replaced by PCBM/C60. When PCBM/carbon ETL was used, the I_0 further dropped by a factor of 10 to a low of 10^{-9} mA. It is well known that reverse bias saturation current I_0 is related to loss of photogenerated charge carriers at the defects which reflects the quality and defect states of interfaces [144].

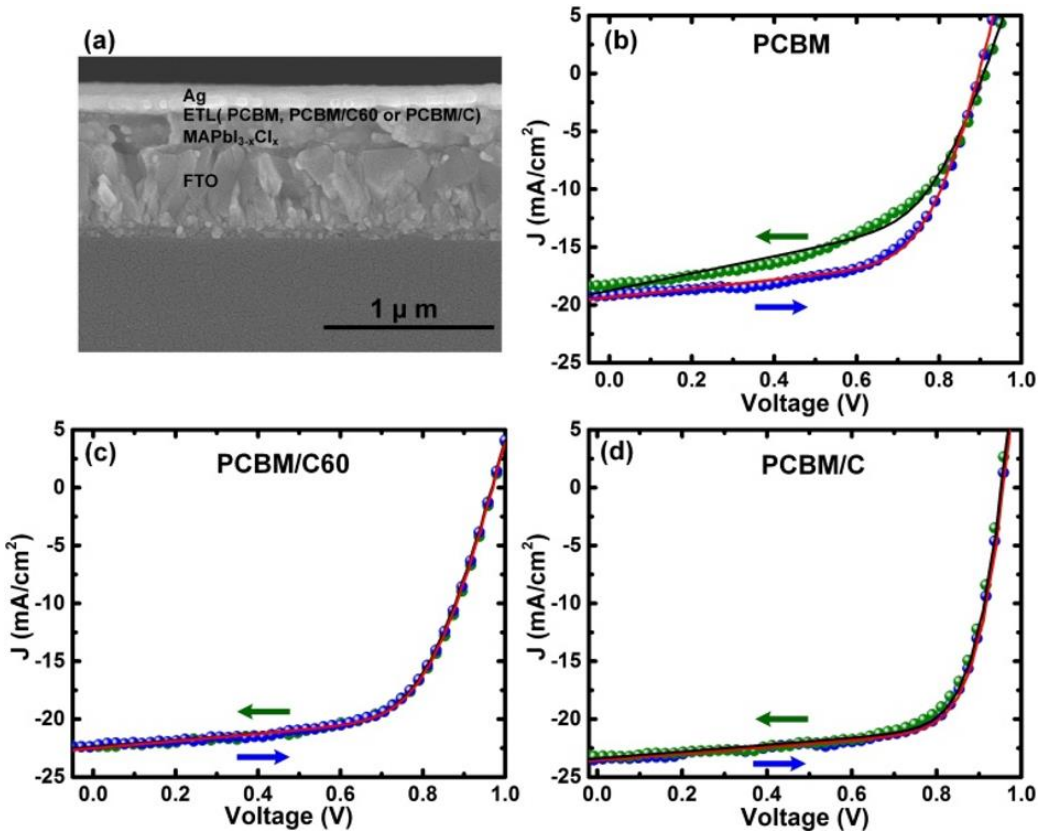

Fig. 28. (a) SEM image of FTO/PEDOT:PSS/$MAPbI_{3-x}Cl_x$/ETL/Ag solar cell and current-voltage characteristics of perovskite solar cells with (b) PCBM, (c) PCBM/C60 and (d) PCBM/carbon ETLs. Reproduced by permission of PCCP Owner Societies [17].

Table 3. Photovoltaic parameters of $MAPbI_{3-x}Cl_x$ perovskite solar cells with different electron transport layers.

		J_{SC} (mA/cm^2)	V_{OC} (V)	FF	η (%)	R_{sh} (kΩ)	R_s (Ω)	Io (mA)
PCBM	**FS**	19.35	0.90	0.61	10.6	2.6	43.6	4.9×10^{-8}
	RS	18.32	0.91	0.52	8.6	1.3	62.1	3.1×10^{-8}
PCBM/C60	**FS**	22.47	0.97	0.64	14.0	3.4	53.7	1.5×10^{-8}
	RS	22.47	0.97	0.64	14.0	3.2	52.1	1.5×10^{-8}
PCBM/C	**FS**	23.69	0.96	0.71	16.2	3.5	9.97	2.2×10^{-9}
	RS	23.40	0.95	0.71	15.8	3.4	10.02	3.2×10^{-9}

6.5 Interface trap density and charge extraction

To evaluate the trap density of perovskite films, excitation- dependent PL measurement is utilized in which the initial photogenerated charge carrier density n(0) is given by an equation [60,145],

$$n(0) = \sum_i N_t^i\,(0)\left(1 - \exp\left(-\frac{a_i \tau_0 I_{PL}}{k}\right)\right) + \frac{I_{PL}}{k} \qquad (12)$$

where e $I_{PL} = k\int_0^\infty n(t)/\tau_0\, dt$ is the integrated PL intensity, k is a constant for a given sample, τ_0 is the PL lifetime, N_t^i is the initial unfilled trap state density and a^i is the product of the trap cross section and the carrier velocity. A quantitative analysis of experimental data using equation 12 will yield bulk (N_t^B) trap densities of perovskite film and interface or surface trap density (N_t^S) of perovskite film with or without ETL. PL measurements were carried out with a 450 nm laser source to excite samples that were coated with a polymethyl methacrylate (PMMA) layer to avoid degradation induced by air exposure [59]. In particular, PL excitation densities were varied to yield photogenerated carriers from low 10^{14} cm^{-3} to 10^{17} cm^{-3}. Fig. 29 (a) shows photogenerated charge carriers as a function of normalized PL intensity which was fitted to equation 12 and shown with solid lines. The extracted interface and bulk trap densities are listed in Table 4. Note that interface trap density was somewhat reduced, depending upon electron transfer layers of PCBM, PCBM/C60 and PCBM/carbon. As expected, the perovskite film contained a significant amount of surface trap of 5.17×10^{17} cm^{-3}, which is in good agreement with previously reported values [144,145,146]. When PCBM is applied on perovskite film, interfacial trap density was decreased to 2.40×10^{17} cm^{-3}. The further reduction of interface trap density to 1.55×10^{16} cm^{-3} and 1.07×10^{17} cm^{-3} was observed for perovskite/PCBM/C60 and perovskite/PCBM/carbon, respectively. Fig. 29 (b) shows the close relationship between interface defects and reverse saturation current of perovskite solar cells. This suggests that the perovskite/PCBM/carbon layer effectively passivated

the interface defects of the perovskite film, which might lead to a reduced saturation current of perovskite solar cells. However, such trend is rather unexpected because the PCBMs in the PCBM/C60 and PCBM/carbon layers were in direct contact with the perovskite layer, which should result in similar interfacial trap densities for samples. In particular, we found that bulk trap densities for all samples were almost identical. It is well known that thermal treatment facilitates the diffusion of PCBM and C60 into perovskite, which subsequently passivate bulk defects. As mentioned earlier, no thermal treatment was carried out for all samples due to thermal degradation at elevated temperature. This suggests that extensive diffusion of PCBM, C60 and carbon did not occur which does not affect the bulk trap densities.

To further understand interfacial charge carriers, the lifetime decays of perovskite films with an ETL quenching layer were evaluated using a time-correlated single photon counting (TCSPC) system, as shown in Fig. 29 (c). In this regard, samples were excited with a 450 nm pulsed diode laser (FWHM ≈ 120 ps) at a repetition rate of 4 MHz and an excitation intensity of 107 mW/cm^2. The exponential decays were fitted with bi-exponential decay functions, containing a fast decay (τ_1) and slow decay (τ_2) [132]. It should be noted that a slow decay is due to radiative recombination, whereas a fast decay occurs due to defects or quenchers. Therefore, the quenching efficiency of ETL can be evaluated by comparing the fast decay. As expected, the perovskite film without electron transport quenching layers had fast and slow decay lifetimes of 3.63 ns and 28.5 ns, respectively. This suggests that radiative recombination dominated for the perovskite film when there is no electron transport quenching layer. As expected, the presence of the quenching ETL layer on the perovskite film significantly reduced a fast decay component of perovskite films. In particular, fast decay lifetimes were 0.94 ns, 0.82 ns and 1.19 ns with corresponding slow decay lifetimes of 5.63 ns, 5.32 ns and 5.93 ns for perovskite/PCBM, perovskite/PCBM/C60 and

perovskite/PCBM/carbon, respectively. Based on the results of lifetime decays, all electron transport quenching layers of PCBM, PCBM/C60 and PCBM/carbon were comparable while the PCBM/C60 showed slightly better quenching efficiency. Notably, the different lifetime decays for ETLs infer the modification of perovskite/PCBM interfacial layer. We think that the interfacial modification occurred during or/and after the deposition of C60 and carbon on the PCMB layer. Some insights can come from PCBM surface morphologies containing nanoscale grains with pinholes, as shown in the SEM image of Fig. 27 (d). We believe that C60 and carbon diffuse through the PCBM grain boundaries or/and pinholes and subsequently modify the perovskite/PCBM interface, as illustrated in Fig. 29 (d). Since the atomic size of carbon is much smaller than C60, the diffusion process can be facilitated much more easily than with C60. As described earlier, the direct contact of carbon on perovskite will inevitably reduce the built-in voltage of perovskite solar cells due to the deep work function of carbon. Indeed, we observed the slightly reduced V_{OC} of perovskite solar cells fabricated with PCBM/carbon ETL when compared with perovskite solar cells with PCBM/C60, as shown in Table 5. However, the positive aspect of interfacial modification with carbon would be the enhanced conductivity and reduction of the interfacial defects that were evidenced by power-dependent defect calculation and J-V curve analysis. Such results were the improved J_{SC} and FF of perovskite solar cells with PCBM/carbon ETL.

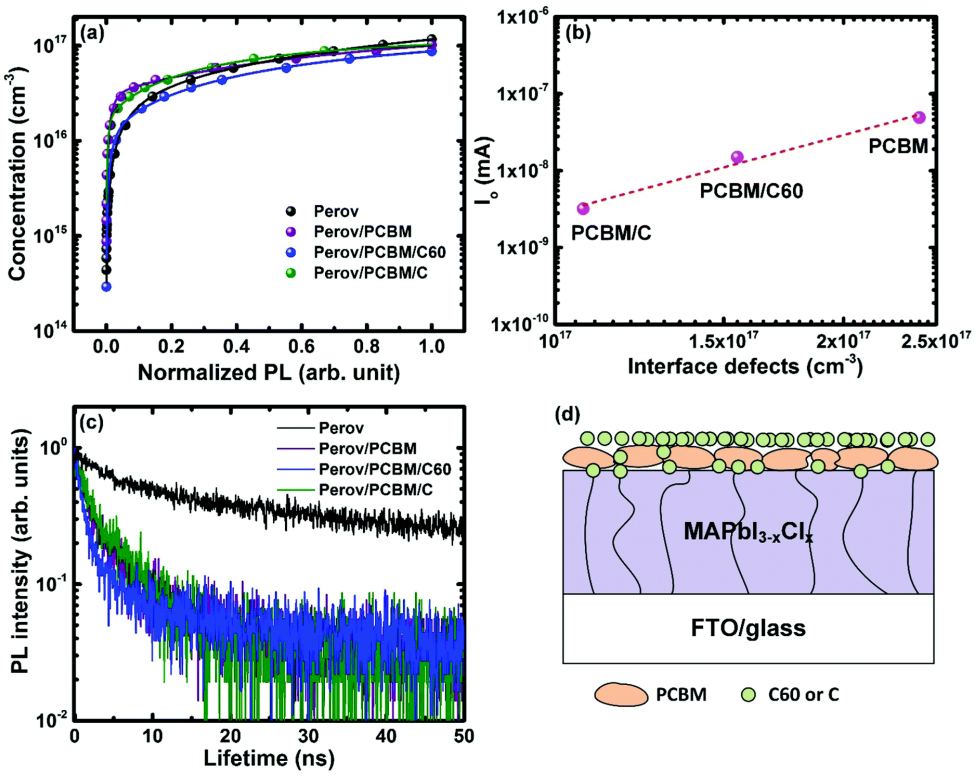

Fig. 29. (a) Photogenerated carriers with normalized PL intensity, (b) reverse saturation current vs. interfacial defect densities of perovskite solar cells with different ETLs, (c) lifetime decays of perovskite films with different ETLs, and (d) schematic of plausible diffusion process of C60 and carbon on PCBM layer. Reproduced by permission of PCCP Owner Societies [17].

Table 4. Interface and bulk trap densities of perovskite with different ETLs.

	Interface trap density (cm^{-3})	**Bulk trap density (cm^{-3})**
Perovskite	5.17×10^{17}	1.66×10^{16}
Perovskite/PCBM	2.40×10^{17}	3.00×10^{16}
Perovskite/PCBM/C60	1.55×10^{17}	1.04×10^{16}
Perovskite/PCBM/C	1.07×10^{17}	1.63×10^{16}

Table 5. Summary of the measured fast decay time (τ_1), slow decay time (τ_2), and average lifetime (τ_{avg}) for perovskites with different ETLs.

	τ_1 (ns)	A_1 (%)	τ_2 (ns)	A_2 (%)	Average lifetime (ns)
Perovskite	3.63	48	28.5	52	16.56
Perov/PCBM	0.94	70	5.63	30	2.35
Perov/PCBM/C60	0.82	87	5.32	13	1.41
Perov/PCBM/C	1.19	61	5.93	39	3.04

6.6 Summary

We have developed a new electron transport layer of PCBM/Carbon which has better conduction and interface passivation than competitive PCBM/C60. In addition, PSC with PCBM/Carbon ETL has photo conversion efficiency of 16.2 % while PSC with PCBM/C60 ETL has 14% PCE. As carbon in abundant in nature, this carbon based ETL will reduce the production cost. So far, the efficiency of perovskite solar cells has improved; however, these solar cells degrade in air. In the following chapter, we will discuss the degradation mechanism of perovskite film when exposed to air.

CHAPTER 7

DEGRADATION MECHANISM OF PEROVSKITE FILM IN AIR

7.1 Introduction

Halide perovskite solar cells have become a promising candidate in the field of solar cells due to the outstanding rise in the power conversion efficiency (PCE) and their low production cost [147,148]. Such tremendous improvement was related to physical properties such as a high absorption coefficient, high mobility of charge carriers, long carrier lifetime and diffusion length, and simple solution-processing methods [59,128,149]. Despite improved PCE, long term stability is one of the major issues impeding outdoor application and commercialization of perovskite solar cells. Degradation of perovskite materials under different environmental conditions leads to chemical instability in the perovskite solar cell, which reduces photovoltaic performance. In general, the main causes of this type of degradation are related to various external conditions such as moisture, oxygen, light, and temperature [91]. In particular, in order to protect the perovskite films from the air the device encapsulation was made. With lower humidity (<30%), the stability of encapsulated solar cell was 1300 hrs while higher humidity expedited the degradation and resulted in shorter lifetime of encapsulated perovskite solar cells [150,151]. Also, various architectural modification including inorganic hydrophobic polymer and carbon electrode have been employed in perovskite device to prevent moisture infiltration in perovskite thin film [152,153].

To further enhance the air stability of perovskite materials, a detailed study of crystallographic, morphological, optical, and mechanical degradation processes in the presence of

moisture in the air is needed. Early research shows that perovskite materials react with moisture and decompose into PbI_2, which quickly degrades the photo conversion efficiency or device performance [154,155]. Walsh, *et al.* [156] indicated that $CH_3NH_3PbI_3$ ($MAPbI_3$) reacts with one single water molecule and converts it into $(CH_3NH_3^+)_{n-1}(CH_3NH_2)PbI_3][H_3O^+]$ by replacing one proton from ammonium. The intermediate phase decomposes into HI, CH_3NH_2, and eventually PbI_2. Christians, *et al.* [157] and Yang, *et al*. [158] found that $MAPbI_3$ hydrated into $(CH_3NH_3)_4PbI_6{\cdot}2H_2O$ in the presence of water, resulting in poor absorption in the visible region. Later, Zhu, *et al.* [159] proposed that perovskite goes under a chemical transition to monohydrate $MAPbI_3{\cdot}H_2O$ in the presence of moisture by sharing one H_2O per MA from the perovskite lattice. In addition, a first-principle study was employed to find the degradation pathway, which revealed that the large interspace in the $MAPbI_3$ perovskite structure caused water to easily enter the inner region and induce structural deformation. From a morphological study, Dao, *et al.* [155] showed the formation of voids in the perovskite film when exposed to air for 18 hrs. However, Christians, *et al.* found highly smooth morphology from a rough surface after 14 days of exposure to air with 90% relative humidity [157]. In addition, photoluminescence (PL) and time-resolved photoluminescence (TRPL) were used to investigate the degradation of perovskite as a non-contact approach. Grancini, *et al*. [160] conducted a PL study, showing blue-shifted PL of perovskite films due to water molecules, which signifies the local distortion of the perovskite crystal lattice. In addition, the study of the degradation of mechanical properties of perovskite material is of great importance because it does not only reveal the basic physical properties of materials for future use, but also has a significant impact on manufacturing and design specifications. Currently, Spina, *et al.* [161] conducted degradation studies of mechanical properties in terms of elastic modulus and hardness of $MAPbI_3$ based perovskite by exposing it to water vapor for a time period starting from

10 days to 170 days. However, for the degradation study, a single crystal $MAPbI_3$ was used instead of multi-crystalline perovskite thin film. Since perovskite solar cells are fabricated by thin films and a number of grains of thin films might play an important role in the degradation mechanism [162,163], it is necessary to study the degradation process of mechanical properties of perovskite thin films. In particular, it is crucial to study the mechanical properties of perovskite thin films with air exposure time as perovskite films degrade very quickly.

Currently, there is no systematic study describing how the air degradation of perovskite films influence the crystallinity and associated mechanical properties such as elastic modulus and hardness of perovskite films. We quantitatively and systematically investigate the crystallographic, morphological and mechanical degradation pathways of $MAPbI_{3-x}Cl_x$ perovskite film that has been widely used for perovskite solar cells. To conduct this study, perovskite thin films were fabricated using a hot casting technique and exposed to air at a humidity of 40% or less. To examine degradation processes, UV-vis, steady-state photoluminescence (PL), X-ray diffraction, high-resolution scanning electron microscope (HRSEM), and nanoindentation technique were employed.

7.2 Optical degradation

While perovskite solar cells have promising prospects, stability has been a major concern for commercialization. It was found that power conversion efficiency (PCE) degrades very rapidly due to a series of factors such as moisture, oxygen, temperature, and ultraviolet (UV) radiation [143,154,155,157,158,164]. In this work, we focused on the study of the degradation of $MAPbI_{3-x}Cl_x$ perovskite materials due to the presence of moisture in the air. Fig. 30 (a) shows $MAPbI_{3-x}Cl_x$ perovskite films as a function of air exposure time. Strikingly, the hydrated perovskite film turned

into an irreversible yellow, non-perovskite phase from a black perovskite phase after more than 20 hrs air exposure of 40% humidity. After 66 hrs air exposure, the perovskite film completely turned into yellow color. This yellow phase indicates the irreversible degradation of $MAPbI_{3-x}Cl_x$ into PbI_2 phase in the film [165]. To investigate the evolution of optical degradation of perovskite films with air exposure times, optical absorption and PL measurements were also performed. Fig. 30 (b) shows the absorption spectra of perovskite thin films as a function of air exposure time. The fresh perovskite thin film revealed a wide absorption band from 400 to 850 nm. One of the interesting features of the absorption spectrum is the sharp band edge of the perovskite thin film, which lies between 740 to 780 nm, yielded a bandgap of around 1.64eV, as shown in an inset of Fig. 30 (b). It is noteworthy that the sharp perovskite band edge begins to drastically degrade after 20 hrs air exposure. As shown in an inset of Fig. 30 (b), the band edge of the perovskite films after 27 hrs air exposure resulted in the significant degradation and complete diminishment after 66 hrs air exposure. Also, it is worthwhile noting the absorption peak at 520 nm assigned to the PbI_2 [157] became noticeable after 27 hrs exposure to air. Fig. 30 (c) shows the evolution of PL with air exposure time. In this case, a Horiba FluoroLog-3 spectrofluorometer was used to measure PL in which the perovskite film was excited by a 450 nm solid-state laser. The fresh perovskite film exhibited the dominant PL peak at 760 nm, as shown in Fig. 30 (c). When a perovskite film is exposed to air, the PL gradually shifted to short wavelength, gradually shifting from 760 nm at 0 hrs to 728 nm after 15 hrs of air exposure. Further air exposure drastically reduced PL intensities which are not shown. Another interesting observation is the asymmetric PL spectra that were skewed to shorter wavelength. Our previous study showed that the asymmetric PL spectra were related to the formation of non-stoichiometric Pb-rich perovskite chemistries [15,16]. Therefore,

the blueshift of PL and development of asymmetric PL spectra could be related to the degradation of perovskite films to Pb-rich perovskite chemistries.

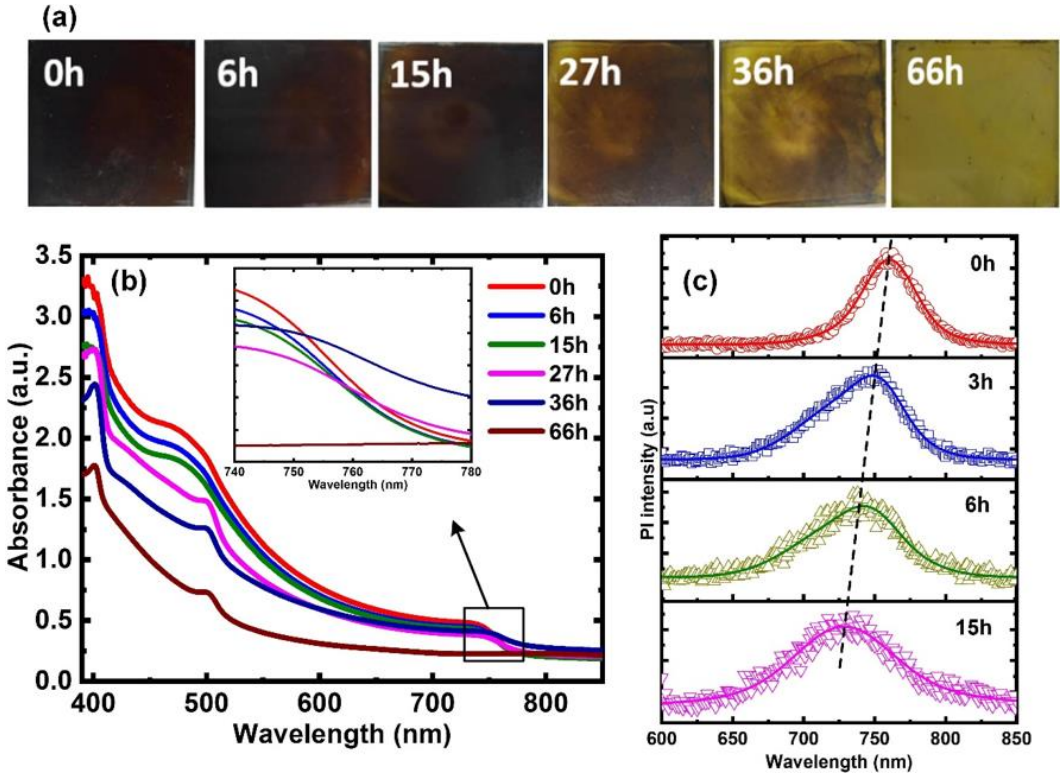

Fig. 30. (a) Photographs showing the color deformation of $MAPbI_{3-x}Cl_x$ thin films exposed to air at a humidity of 40% for up to 66 hrs, (b) absorption spectrum of perovskite film with exposure time, an inset is the magnified view of absorption band edges from 740 to 780 nm, and (c) evolution of PL spectra exhibiting the blueshift of PL [18].

7.3 Crystal degradation

Fig. 31 (a) shows a scanning electron microscope (SEM) image of a perovskite film fabricated by a hot-casting technique that features large-area crystal growth. As shown in Fig. 31

(b), the bare perovskite film exhibited XRD peaks of $MAPbI_{3-x}Cl_x$ film at 14.1º, 28.5º, and 31.9º corresponding to (110), (220), and (310) $MAPb_{3-x}Cl_x$ planes, respectively. The XRD peak at 15.6 ° was assigned to $CH_3NH_3Cl_3$. These perovskite films were exposed to air for 66 hrs at ~40% humidity and the degradation of perovskite crystallinity was monitored by XRD measurement. It is found that the intensity of perovskite XRD peaks gradually decreased over time and almost completely disappeared after 66 hrs of air exposure, as shown in Fig. 31 (b). Interestingly, new peaks of PbI_2 gradually appeared during degradation while an additional XRD peak at 38.7º was observed, which was assigned as (201) I_2. When comparing the integral intensities of the $MAPbI_{3-x}Cl_x$, PbI_2 and I_2 peaks, the XRD intensity of PbI_2 was dominant when exposed to air for 20 hrs. To investigate the effect of the degradation of perovskite films on the crystal size, XRD patterns of perovskite films were further analyzed using Scherrer equation $L = \frac{K\lambda}{\beta \, Cos \, \theta}$ where L is the average crystal size, λ is the wavelength of the X-ray irradiation (0.154 nm), and β is the full width at half maximum (FWHM) [96,97]. As shown in Fig. 31 (d), the crystal size of bare $MAPbI_{3-x}Cl_x$ was calculated to be around 40 nm, which is in good agreement with other reports [166]. In particular, upon exposure to air the crystal size of $MAPbI_{3-x}Cl_x$ initially increased and then started to decrease. Interestingly, an initial increase in crystal size of $MAPbI_{3-x}Cl_x$ is unexpected upon exposure to air. However, many reports demonstrate the enlarged crystal size of perovskite films when perovskite films were fabricated to high humidity level that facilitated recrystallization of grain edges and led to the merging of adjacent grains within the film[166]. In contrast, the crystal size of PbI_2 continuously increased with prolonged exposure to air. The noticeable orthorhombic I_2 (201) at 38.7º was observed around 10 hrs exposure to air. The crystal size of I_2 gradually increased up to 36 hrs and then started to decrease.

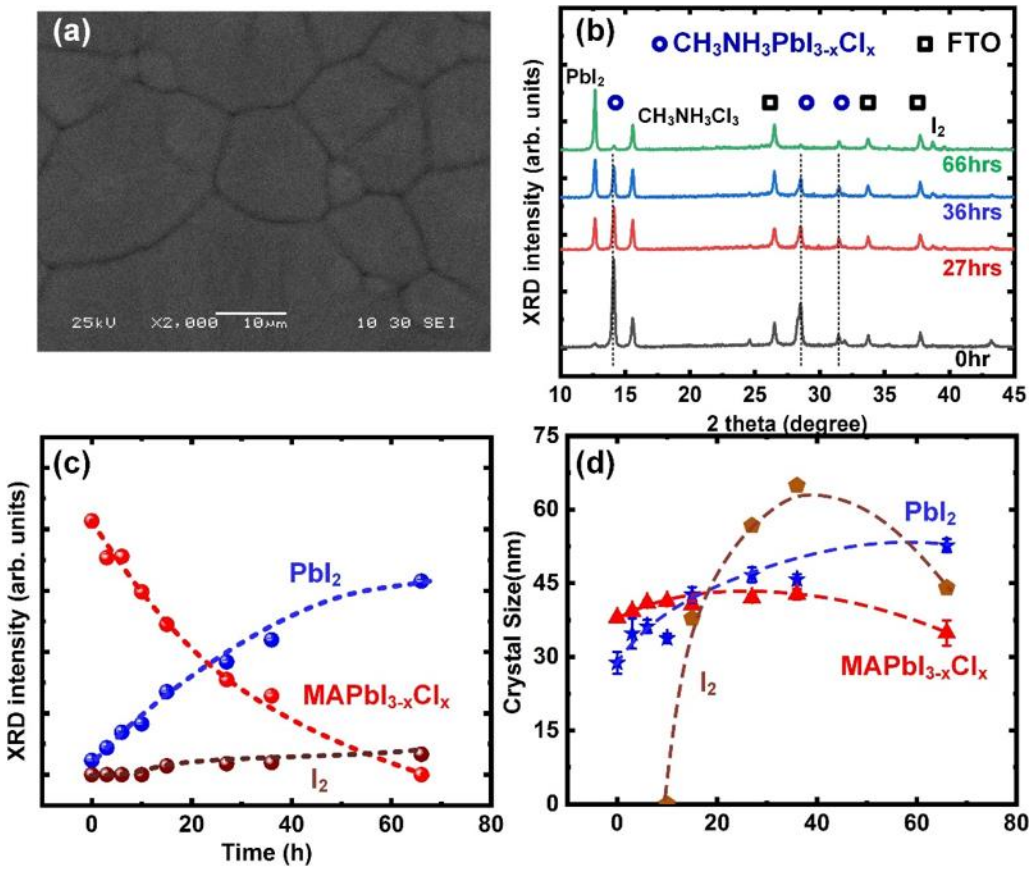

Fig. 31. (a) SEM image of $MAPbI_{3-x}Cl_x$ film, (b) XRD patterns of $MAPbI_{3-x}Cl_x$ film exposed to air for up to 66 hrs, (b) integrated intensity of $MAPbI_{3-x}Cl_x$, PbI_2, and I_2 extracted from XRD patterns, (c) the average crystal size of $MAPbI_{3-x}Cl_x$, PbI_2, and I_2 determined from Scherrer's equation [18].

7.4 Morphological degradation

To understand the dynamic variation of the crystal size of perovskites, surface morphologies of perovskite films were carried out using SEM measurements. Fig. 32 shows high-resolution SEM images of perovskite films as a function of air exposure time. The bare perovskite films in Fig. 32 (a) exhibited continuous films composed of a number of small grains. After 27

hrs-air exposure, small grains became a little enlarged but started to develop pin-holes on the surface of perovskite films. This observation is identical to the XRD measurement in Fig. 31 (d). Prolonged air exposure to 49 and 66 hrs led to the development of pin-holes on the surface of perovskite films, as shown in Fig. 32 (c)-(d). In particular, after 66 hrs-air exposure, pin-holes covered the entire surface of perovskite films. We think that pin-holes of perovskite films might lead to the decrease in the crystal size of perovskite films, as observed in Fig. 32 (d).

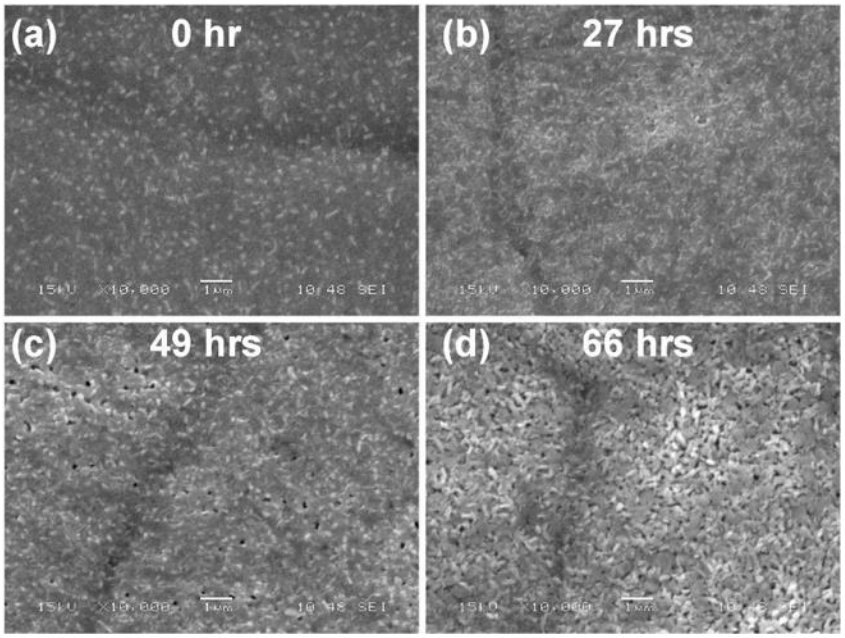

Fig. 32. Top view SEM images of perovskite thin film with various exposure time in air. (a) 0, (b) 27, (c) 49, and (d) 66 hrs. Scale bar is 1μm for images [18].

7.5 Mechanical degradation

The air degradation of perovskite films accompanied the formation of a number of pin-holes of perovskite films that might alter the mechanical hardness of perovskite films. To

investigate the mechanical properties of depredated perovskite films, a nano-indenter XP was used and its configuration was described in an experimental section. Fig. 33 shows the elastic modulus and hardness of the $MAPbI_{3-x}Cl_x$ thin film, measured at 6%, 9%, 32% and 51% of the normalized indentation depth to the film thickness of ~ 440 nm thick $MAPbI_{3-x}Cl_x$. It is found that elastic modulus and hardness values were strongly dependent upon the indentation depth. Fig. 33 summarizes five different indentation depths normalized to the film thickness (h_c/t_f= 6%, 9%, 15%, 32%, 51%) to illustrate the change of elastic modus and hardness with time in which h_c and t_f are indentation depth and film thickness, respectively. Clearly, the elastic modulus at indentation depths normalized to film thicknesses of 6%, 9% and 15% exhibited a similar trend with air exposure time, as shown in Fig. 33 (a). However, close examination showed that the elastic modulus measured at h_c/t_f = 15% exhibited a relatively higher value as compared to the 6% and 9% respectively due to the substrate effect. The study of the other two normalized indentation depths of 29% and 51% mainly showed the substrate dominance on the perovskite material [163]. In contrast, the hardness decreased with an increase in indentation depth that might be due to the dislocations and grain boundary activity in the plastic zone [167]. Typically, an indentation depth of less than 10% of the film thickness, i.e. 70 nm displacement, was used to measure the mechanical properties of the films to circumvent the substrate effect [163,167,168,169]. It is found that at 0 hrs air exposure the elastic modulus and hardness of the $MAPbI_{3-x}Cl_x$ films with h_c/t_f=9% (or 49 nm) indentation depth were 19.65±2.45 GPa and 0.78±0.05 GPa, respectively. Note that the measured elastic modulus and hardness were in the range of 10-20 GPa and 0.25-1.01 GPa for single crystal perovskite films ($CH_3NH_3PbX_3$, where X = I, Br and Cl), respectively [161,170,171]. Interestingly, the values of the elastic modulus and hardness peaked at around 20~25 hrs which can be correlated to the increased crystallinity and crystal size observed by XRD and SEM

measurements. With further air exposure, the modulus and hardness of the perovskite films gradually decreased. The decrease in elastic modulus and hardness can be attributed to the chemical decomposition of the perovskite films, as demonstrated from the XRD and SEM images in Fig. 31 and Fig. 32.

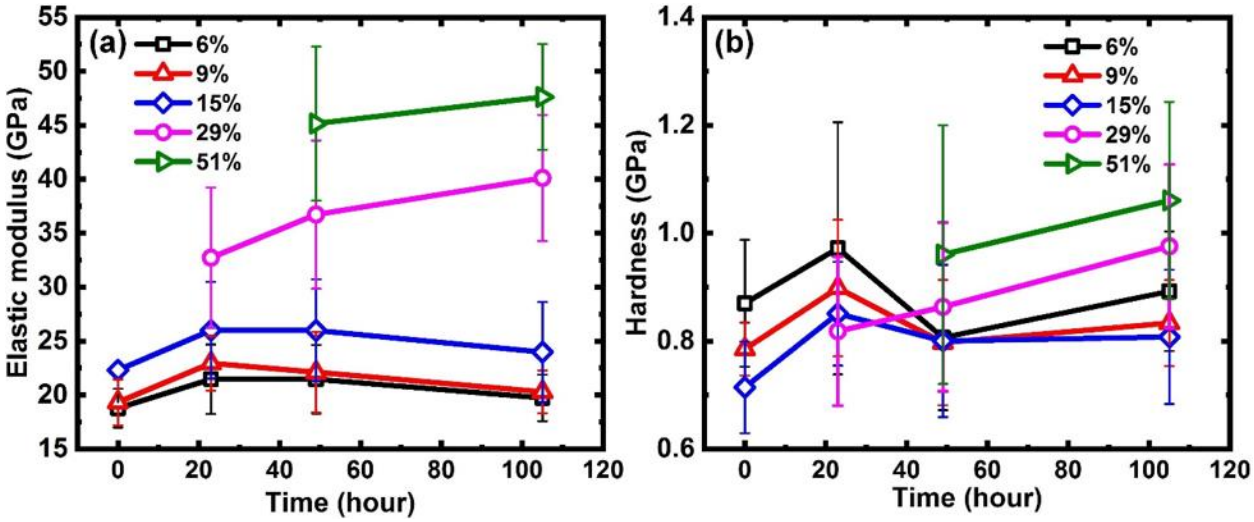

Fig. 33. (a) Elastic modulus and (b) hardness of five different indentation depths (h_c/t_f = 6%, 9%, 15%, 32%, 51%) where h_c and t_f are indentation depth and film thickness, respectively. The thickness of perovskite film is 440 nm [18].

7.6 Summary

We systematically investigated the degradation mechanism of perovskite film when exposed to air with a relative humidity of 40% using optical, crystal, morphological, and mechanical characterization techniques. Perovskite ($CH_3NH_3PbI_{3-x}Cl_x$) films completely degrade into PbI_2 and I_2 after exposure to air for 66 hrs. The crystal size of perovskite increased initially

due to the merging of adjacent grain and began to decrease with increased exposure time due to chemical decomposition and formation of pinholes. This dynamic crystal size variation also matched with the elastic modulus and hardness of the film.

CHAPTER 8

CONCLUSIONS

8.1 Achieved Results

The main goal of this dissertation was to fabricate highly efficient and low-cost perovskite solar cells. For that, we have incorporated a hot-casting technique to fabricate uniform, pinhole-free, and larger grain perovskite film. The GIs and GBs of perovskites have been investigated using chemically, spatially, and temporally resolved measurements at the nanoscale. The local variations in steady-state PL and a time-resolved lifetime are correlated to chemistries, to nanoscale morphologies, and to recombination kinetics. The localized chemical compositions of $MAPbI_{3-x}Cl_x$ perovskites revealed that the GBs were characterized by an absence of chloride, an enriched oxygen concentration, and iodide vacancies, regardless of the gain sizes. In contrast, we found that the content of Cl at the GIs is strongly dependent upon the grain sizes. Critically, the spatially and temporally resolved PL and lifetime measurements revealed non-radiative characteristics at the GBs, such as very strong PL quenching and relatively shorter lifetimes. The results suggest that the GBs indeed contain deep defect centers that might serve as recombinant centers and be detrimental to the perovskite solar cells. However, the benign characteristics of GBs of perovskites can be originated from the bandgap broadening of non-stoichiometric $MAPbI_x$ or PbI_x perovskites at the GB that will form the potential barriers for photo-generated charge carriers toward the GBs. As a consequence, the photo-generated charge carriers adjacent to the GBs will be easily repelled by the GBs, resulting in a greater reduction of the recombination of charge carriers. This is one possible reason for the high performance of $MAPbI_{3-x}Cl_x$ based solar cells.

Later, we developed a new characterization method capable of probing perovskite films which can provide prompt feedback on the quality of films. In particular, the deconvoluted PL approach can provide information on the ordered and disordered phases of perovskite films that mainly originate from the GIs and GBs, respectively. Systematic analysis of power dependent PL spectra on smaller and larger grain perovskites revealed that the nature of the GBs strongly depended on grain size. The larger grains followed an excellent power law that exhibited exciton-like recombination for both the ordered and disordered phases of the PL spectra. In contrast, perovskite films with smaller grain size showed exciton-like recombination for the ordered phase while non-radiative recombination dominated for the disordered phase. Such an observation was closely correlated with the photovoltaic performance of perovskite solar cells. A perovskite solar cell with a large grain size increased the efficiency with higher absorption and effective charge separation at the PEDOT/perovskite interface. In contrast, much lower efficiency was observed for solar cells with smaller grains which showed poor quenching efficiency and light harvesting capability.

We have fabricated a PSCs that has interface defects that lead to the hysteresis effect. So, we demonstrated a new PCBM/carbon electron transport layer for perovskite solar cells. The ultra-flat carbon layer was successfully deposited using e-beam irradiation technique on the soft perovskite/PCBM layer. The deposited carbon film showed higher conductivity than PCBM and C60 by a few orders of magnitude. In addition, it is found that combined PCBM/carbon ETL reduced the interfacial defects and improved shunt and series resistances of perovskite solar cells. In particular, the improved photovoltaic performance and reduced hysteresis of perovskite could be attributed to carbon-induced passivation of interfacial traps. Our results demonstrate the

potential of the use of cost-effective carbon for perovskite solar cells which could reduce production costs.

Then, we investigated the degradation of $CH_3NH_3PbI_{3-x}Cl_x$ perovskite films, particularly in terms of their crystallographic, morphological and mechanical properties when exposed to air at 40% humidity. Steady-state PL spectra revealed a blueshift from 760 nm with development of asymmetric PL spectra when exposed to air which are related to the development of non-stoichiometric Pb-rich perovskite chemistries. Remarkably, UV-VIS measurements revealed noticeable PbI_2 peaks while the perovskite phase diminished with increased air exposure time. Furthermore, morphology and crystal size distribution studies have shown that initial air exposure has slightly increased the crystal size. However, the development of pinholes reduced the crystal sizes beyond 20 hrs air exposure. The mechanical properties including elastic modulus and hardness also evolved with exposure time in the same manner that the crystal size distribution and morphology evolved. This work demonstrates a comprehensive picture of degradation mechanisms of perovskite films with air exposure and facilitates the design and fabrication of perovskite solar cells sustainable in air. Identification of the degradation mechanism of perovskite film provides guidance for future development of air stable perovskite solar cells.

8.2 Future works

We have optimized a perovskite solar cell with a structure of FTO/ PEDOT:PSS/ Perovskite/PCBM/ Carbon/Ag, as shown in Fig. 34 (a). This solar cell has the photoconversion efficiency of ~16% as shown in Fig. 34 (b). However, this solar cell degrades with the exposure of humidified air. In particular, perovskite film quickly degrades into PbI_2 and I_2 when exposed to air, as discussed in chapter 7. Moreover, the hole transport layer and electron transport layer

degrade with air exposure which will intensify the degradation mechanism. Our future plan is to replace organice HTL (PEDOT:PSS) and ETL (PCBM) with metal oxide based hole and electron transport layers. We have observed initial improvement by replacing organic PEDOT:PSS using NiO.

Currently, various inorganic HTLs such as NiO_x, CuSCN, MoO_3, V_2O_5, CuI have been introduced into perovskite solar cells [172]. Among the inorganic HTLs, NiO_x is attracting more attention due to the interfacial band energy alignment with perovskite, strong hole charge extraction characteristics, and optical transparency. However, there are few drawbacks associated with NiO_x as the HTL layer of solar cells which needs to be resolved. In particular, NiO_x layer contains a lot of surface defects, which act as potential trap states in the solar cell structure. These trap states are related to internal defects which cause unwanted severe hysteresis and light soaking phenomenon [173]. Moreover, current synthesis processes of NiO are time consuming and require the use of toxic chemicals such as ethylenediamine and hydrazine monohydrate. We developed a simple, non-toxic, and time efficient process for preparing NiO precursor. In particular, we mixed NiO powder with HCl only for 15 min at 75 °C with magnetic stirring. Then we spun coat this precursor using hot-casting technique. This NiO was applied to our reference solar cell instead of PEDOT:PSS as shown in Fig. 34 (a). We have fabricated ~17% efficient solar cell using NiO which has improved open circuit voltage more than that of PEDOT:PSS based solar cells.

Fig. 34 (c) shows a comparison of the stability of two solar cells: one with PEDOT:PSS HTL and the other with NiO HTL, where the photo conversion efficiency is normalized to 1. PSCs were stored in ambient environtment with a relative humidity less than 40%. The performance of the PEDOT:PSS based solar cell is reduced to ~20% from its intial performance within only 24 hrs of exposure to air. This degradation is due to the decomposition of perovskite into PbI_2 and I_2,

as discussed in the previous chapter. On the contrary, the degradation rate is slower for NiO based solar cells. The PCE of a solar cell with NiO HTL decreased to ~40% when exposed to air for 168 hrs. The application of NiO prevents the degradation of perovskite from NiO side. However, the performance degradation of perovskite occurs from the ETL side. Note that, PEDOT:PSS is a hygroscopic material. Kenji Kawano *et al.* [174] revealed that PSS is present in excess amount in PEDOT:PSS. This exceess amount of PSS reacts with other elements and undergoes oxido-de-sulfonato-substitution where two PSS link together with sulfonic ester group. Finally PEDOT:PSS loses its property and increses the series resitance, which results in quick degradation of PCE of solar cells [174, 175].

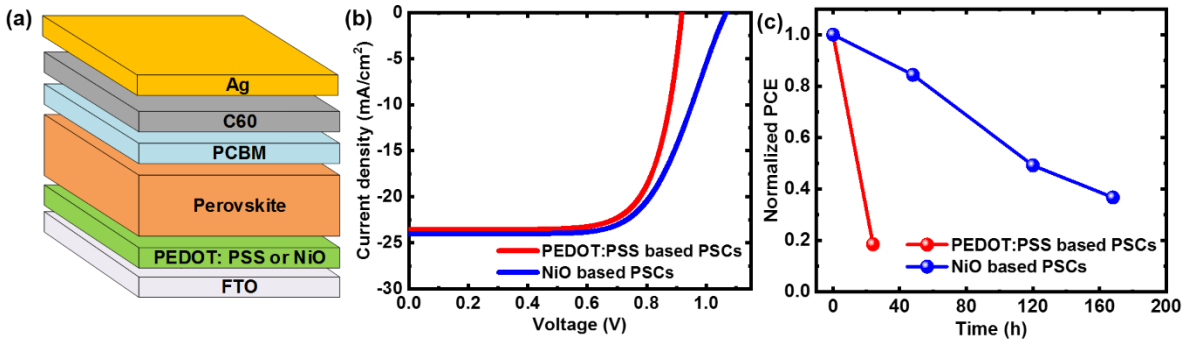

Fig. 34. (a) p-i-n inverted structure composed of FTO/ (PEDOT:PSS or NiO)/ perovskite/ PCBM /C60/ Ag, (b) current-voltage characteristics of two PSCs: one with HTL of PEDOT:PSS and the other with HTL of NiO, (c) Normalized PCE of perovskite solar cells with two different HTLs (NiO and PEDOT:PSS) as a function of aging time in air.

A further improvement can be achieved by incorporating another layer on the perovskite or by adding additive in the perovskite to remove ion migration from perovskite to electrodes and

to passivate the defective grain boundaries. Thus, our future goal is to control the ion migration of the perovskite film. After that, we will apply an encapsulation layer on top of the solar cell to protect it from air. Moreover, the irreversible thermal degradation of the perovskite films was observed at 70 °C [89,143], so our future goal is to fabricate highly efficient thermal and air stable perovskite solar devices. Finally, the above-mentioned modifications will help to commercialize low cost perovskite solar cells.

REFERENCES

[1] Environmental Protection Agency (EPA), "Inventory of U.S. Greenhouse Gas Emissions and Sinks: 1990-2015", *EPA*, 2017.

[2] Energy Information Agency (EIA), "How much of the U.S. carbon dioxide emissions are associated with electricity generation?", *EIA*, 2017.

[3] U. N. Ureigho, "Global warming and environmental degradation" *Nigerian Journal of Agriculture, Food and Environment*, vol. 14, no. 1, pp. 31-34, 2018.

[4] Intergovernmental Panel on Climate Change (IPCC) report on, "Renewable Energy Sources and Climate Change Mitigation", chapter 9, pp. 1075, 2011. [Accessed: February 2019]

[5] National Renewable Energy Laboratory (NREL), "Renewable Electricity Futures Study", Vol. 1, pp. 210, 2012. [Accessed: February 2019]

[6] NREL Fact Sheet, "Life Cycle Greenhouse Gas Emissions from Electricity Generation", 2013. [Accessed: February 2019]

[7] M. E. Becquerel, "Mémoire sur les effets électriques produits sous l'influence des rayons solaires", *Comptes rendus hebdomadaires des séances de l'Académie des sciences*, vol. 9, pp. 561-567,1839.

[8] M. L. Fraas, "Low-cost solar electric power", *New York: Springer*, pp. 31-42, 2014.

[9] The Nobel Prize in Physics 1921. NobelPrize.org. Nobel Media AB 2019. [online] Available: https://www.nobelprize.org/prizes/physics/1921/summary/ [Accessed: February 2019]

[10] Peter Gevorkian, "Solar Power Generation Problems, Solutions, and Monitoring", *Cambridge*, Appendix G, PP-457-459.

[11] US energy information administration, Monthly energy review, Table 1.3 and 10.1, April 2018. [online] Available: https://www.eia.gov/energyexplained/index.php?page=renewable_home [Accessed: February 2019]

[12] NREL chart homepage, http://www.nrel.gov/ncpv/images/efficiency_chart.jpg [Accessed: February 2019].

[13] M. Cai, Y. Wu, H. Chen, X. Yang, Y. Qiang, and L. Han, "Cost-performance analysis of perovskite solar modules", *Advanced Science*, vol. 4, no. 1, pp. 1600269, 2017.

[14] E. W. G. Diau, "Next-Generation Solar Cells and Conversion of Solar Energy", *ACS Energy Letters*, vol. 2, no. 2, pp. 334-335, 2017.

[15] G. Namkoong, H. J. Jeong, A. Mamun, H. Byun, D. Demuth, and M. S. Jeong, "Chemically, spatially, and temporally resolved 2D mapping study for the role of grain interiors and grain boundaries of organic-inorganic lead halide perovskites", *Solar Energy Materials and Solar Cells*, vol. 155, pp. 134-140, 2016.

[16] A. Al Mamun, T. T. Ava, H. J. Jeong, M. S. Jeong, and G. Namkoong, "A deconvoluted PL approach to probe the charge carrier dynamics of the grain interior and grain boundary of a perovskite film for perovskite solar cell applications", *Physical Chemistry Chemical Physics*, vol. 19, no. 13, pp. 9143-9148, 2017.

[17] A. Al Mamun, T. T. Ava, K. Zhang, H. Baumgart, and G. Namkoong, "New PCBM/carbon based electron transport layer for perovskite solar cells", *Physical Chemistry Chemical Physics*, vol. 19, no. 27, pp. 17960-17966, 2017.

[18] A. Al Mamun, Y. Mohammed, T. T. Ava, G. Namkoong, and A. A. Elmustafa, “Influence of air degradation on morphology, crystal size and mechanical hardness of perovskite film”, *Materials Letters*, vol. 229, pp. 167-170, 2018.

[19] Q. Chen, N. De Marco, Y. M. Yang, T. B. Song, C. C. Chen, H. Zhao, Z. Hong, H. Zhou, and Y. Yang, “Under the spotlight: The organic–inorganic hybrid halide perovskite for optoelectronic applications”, *Nano Today*, vol. 10, no. 3, pp. 355–396, 2015.

[20] V. M. Goldschmidt, “Krystallbau und chemische Zusammensetzung”, *Berichte der deutschen chemischen Gesellschaft (A and B Series)*, vol. 60, no. 5, pp. 1263–1296, 1927.

[21] T. Leijtens, K. Bush, R. Cheacharoen, R. Beal, A. Bowring, and M. D. McGehee, “Towards enabling stable lead halide perovskite solar cells; interplay between structural, environmental, and thermal stability”, *Journal of Materials Chemistry A*, vol. 5, no. 23, pp. 11483–11500, 2017.

[22] C. Li, X. Lu, W. Ding, L. Feng, Y. Gao, and Z. Guo, “Formability of ABX_3 (X=F, Cl, Br, I) Halide Perovskites”, *Acta Crystallographica Section B: Structural Science*, vol. 64, no. 6, pp. 702–707, 2008.

[23] A. A. Bakulin, O. Selig, H. J. Bakker, Y. L. Rezus, C. Muller, T. Glaser, R. Lovrincic, Z. Sun, Z. Chen, A. Walsh, and M. J. Frost, “Real-Time Observation of Organic Cation Reorientation in Methylammonium Lead Iodide Perovskites” *The journal of physical chemistry letters*, vol. 6, no. 18, pp. 3663–3669, 2015.

[24] Z. Li, M. Yang, J. S. Park, S. H. Wei, J. J. Berry, and K. Zhu, “Stabilizing perovskite structures by tuning tolerance factor: Formation of formamidinium and cesium lead iodide solid-state alloys”, *Chemistry of Materials*, vol. 28, no. 1 pp. 284–292, 2015.

[25] G. E. Eperon, S. D. Stranks, C. Menelaou, M. B. Johnston, L. M. Herz, and H. J. Snaith, "Formamidinium lead trihalide: a broadly tunable perovskite for efficient planar heterojunction solar cells", *Energy & Environmental Science*, vol. 7, no. 3, pp. 982−988, 2014.

[26] M. Saliba, T. Matsui, K. Domanski, J. Y. Seo, A. Ummadisingu, S. M. Zakeeruddin, J. P. Correa-Baena, W. R. Tress, A. Abate, A. Hagfeldt, and M. Grätzel, "Incorporation of rubidium cations into perovskite solar cells improves photovoltaic performance", *Science*, vol. 354, no. 6309, pp. 206-209, 2016.

[27] A. Dualeh, P. Gao, S. I. Seok, M. K. Nazeeruddin, and M. Grätzel, "Thermal behavior of methylammonium lead-trihalide perovskite photovoltaic light harvesters", *Chemistry of Materials*, vol. 26, no. 21, pp. 6160-6164, 2014.

[28] G. Niu, W. Li, J. Li, X. Liang, and L. Wang, "Enhancement of thermal stability for perovskite solar cells through cesium doping", *RSC Advances*, vol. 7, no. 28, pp. 17473-17479, 2017.

[29] M. Kulbak, D. Cahen, and G. Hodes, "How Important Is the Organic Part of Lead Halide Perovskite Photovoltaic Cells? Efficient $CsPbBr_3$ Cells", *The journal of physical chemistry letters*, vol. 6, no. 13, pp. 2452–2456, 2015.

[30] C. K. Moller, "Crystal structure and photoconductivity of caesium plumbohalides," *Nature*, vol. 182, no. 4647, pp. 1436, 1958.

[31] M. Saliba, T. Matsui, J. Y. Seo, K. Domanski, J. P. Correa-Baena, M. K. Nazeeruddin, S. M. Zakeeruddin, W. Tress, A. Abate, A. Hagfeldt, "Cesium-containing triple cation perovskite solar cells: improved stability, reproducibility and high efficiency", *Energy & environmental science*, vol. 9, no. 6, pp. 1989-1997, 2016.

[32] J. Jiang, C. K. Onwudinanti, R. A. Hatton, P. A. Bobbert, and S. Tao, "Stabilizing lead-free all-inorganic tin halide Perovskites by ion exchange", *The Journal of Physical Chemistry C*, vol. 122, no. 31, pp. 17660-17667, 2018.

[33] I. Chung, B. Lee, J. He, R. P. H. Chang, and M. G. Kanatzidis, "All-Solid-State Dye-Sensitized Solar Cells with High Efficiency", *Nature*, vol. 485, no. 7399, pp. 486−489, 2012..

[34] K. P. Marshall, M. Walker, R. I. Walton, and R. A. Hatton, "Enhanced Stability and Efficiency in Hole-Transport-Layer-Free $CsSnI_3$ Perovskite Photovoltaics", *Nature Energy*, vol. 1, no. 12, pp. 16178, 2016.

[35] J. Even, L. Pedesseau, J. M. Jancu, and C. Katan, "DFT and k. p modelling of the phase transitions of lead and tin halide perovskites for photovoltaic cells", *physica status solidi (RRL)–Rapid Research Letters*, vol. 8, no. 1, pp. 31-35, 2014.

[36] F. Chiarella, A. Zappettini, F. Licci, I Borriello, G. Cantele, D. Ninno, A. Cassinese, and R. Vaglio, "Combined Experimental and Theoretical Investigation of Optical, Structural, and Electronic Properties of $CH_3NH_3SnX_3$ Thin Films (X= Cl, Br)", *Physical Review B*, vol. 77, no. 4, pp. 045129, 2008.

[37] H. Yu, F. Wang, F. Xie, W. Li, J. Chen, and N. Zhao, "The Role of Chlorine in the Formation Process of "$CH_3NH_3PbI_{3-x}Cl_x$" Perovskite", *Advanced Functional Materials*, vol. 24, no. 45, pp. 7102-7108, 2014.

[38] L. Fan, Y. Ding, J. Luo, B. Shi, X. Yao, C. Wei, D. Zhang, G. Wang, Y. Sheng, Y. Chen, and A. Hagfeldt, "Elucidating the role of chlorine in perovskite solar cells", *Journal of Materials Chemistry A*, vol. 5, no. 16, pp. 7423-7432, 2017.

[39] L. Meng, J. You, T. F. Guo, and Y. Yang, "Recent advances in the inverted planar structure of perovskite solar cells", *Accounts of chemical research*, vol. 49, no. 1, pp. 155-165, 2015.

[40] D. W. de Quilettes, S. M. Vorpahl, S. D. Stranks, H. Nagaoka, G. E. Eperon, M. E. Ziffer, H. J. Snaith, and D. S. Ginger, "Impact of microstructure on local carrier lifetime in perovskite solar cells", *Science*, vol. 348, no. 6235, pp. 683–686, 2015.

[41] A. Kojima, K. Teshima, Y. Shirai, and T. Miyasaka, "Organometal halide perovskites as visible-light sensitizers for photovoltaic cells", *Journal of the American Chemical Society*, vol. 131, no. 17, pp. 6050-6051, 2009.

[42] N. Ahn, K. Kwak, M. S. Jang, H. Yoon, B. Y. Lee, J. K. Lee, P. V. Pikhitsa, J. Byun, and M. Choi, "Trapped charge-driven degradation of perovskite solar cells", *Nature communications*, vol. 7, pp. 13422, 2016.

[43] J. Y. Jeng, Y. F. Chiang, M. H. Lee, S. R. Peng, T. F. Guo, P. Chen, and T. C. Wen, "$CH_3NH_3PbI_3$ perovskite/fullerene planar-heterojunction hybrid solar cells", *Advanced Materials*, vol. 25, no. 27, pp. 3727−3732, 2013.

[44] J. Burschka, N. Pellet, S. J. Moon, R. Humphry-Baker, P. Gao, M. K. Nazeeruddin, and M. Grätzel, "Sequential deposition as a route to high-performance perovskite-sensitized solar cells", *Nature*, vol. 499, no. 7458, pp. 316–319, 2013.

[45] H. Heo, S. H. Im, J. H. Noh, T. N. Mandal, C. S. Lim, J. A. Chang, Y. H. Lee, H. J. Kim, A. Sarkar, M. K. Nazeeruddin, M. Gratzel, and S. I. Seok, "Efficient inorganic–organic hybrid heterojunction solar cells containing perovskite compound and polymeric hole conductors", *Nature photonics*, vol. 7, no. 6, pp. 486–491, 2013.

[46] Y. Liu, Q. Chen, H. S. Duan, H. Zhou, Y. Yang, H. Chen, S. Luo, T. B. Song, L. Dou, Z. Hong, and Y. Yang, "A dopant-free organic hole transport material for efficient planar heterojunction perovskite solar cells", *Journal of Materials Chemistry A*, vol. 3, no. 22, pp. 11940–11947, 2015.

[47] Y. Kato, L. K. Ono, M. V. Lee, S. Wang, S. R. Raga, and Y. Qi, "Silver iodide formation in methyl ammonium lead iodide perovskite solar cells with silver top electrodes", *Advanced Materials Interfaces*, vol. 2, no. 13, pp. 1500195, 2015.

[48] H. Zhou, Y. Shi, K. Wang, Q. Dong, X. Bai, Y. Xing, Y. Du, and T. Ma, "Low-temperature processed and carbon-based ZnO/$CH_3NH_3PbI_3$/C planar heterojunction perovskite solar cells", *The Journal of Physical Chemistry C*, vol. 119, no. 9, pp. 4600–4605, 2015.

[49] Z. Ku, Y. Rong, M. Xu, T. Liu, and H. Han, "Full printable processed mesoscopic $CH_3NH_3PbI_3$/TiO2 heterojunction solar cells with carbon counter electrode", *Scientific reports*, vol. 3, pp. 3132, 2013.

[50] J. Chen, Y. Xiong, Y. Rong, A. Mei, Y. Sheng, P. Jiang, Y. Hu, X. Li, and H. Han, "Solvent effect on the hole-conductor-free fully printable perovskite solar cells", *Nano Energy*, vol. 27, pp. 130–137, 2016.

[51] A. Mei, X. Li, L. Liu, Z. Ku, T. Liu, Y. Rong, M. Xu, M. Hu, J. Chen, and Y. Yang, "A hole conductor free, fully printable mesoscopic perovskite solar cell with high stability", *Science*, vol. 345, no. 6194, pp. 295–298, 2014.

[52] Y. Shao, Z. Xiao, C. Bi, Y. Yuan, and J. Huang, "Origin and elimination of photocurrent hysteresis by fullerene passivation in $CH_3NH_3PbI_3$ planar heterojunction solar cells," *Nature communications*, vol. 5, pp. 5784, 2014.

[53] J. Xu, A. Buin, A.H. Ip, W. Li, O. Voznyy, R. Comin, M. Yuan, S. Jeon, Z. Ning, J.J. McDowell, P. Kanjanaboos, J. P. Sun, X. Lan, L.N. Quan, D.H. Kim, I.G. Hill, P. Maksymovych, and E.H. Sargent, "Perovskite–fullerene hybrid materials suppress hysteresis in planar diodes", *Nature communications*, vol. 6, pp. 7081, 2015.

[54] N. Marinova, S. Valero, and J. L. Delgado, "Organic and perovskite solar cells: working principles, materials and interfaces", *Journal of colloid and interface science*, vol. 488, pp. 373-389, 2017.

[55] C. Zhang, J. Zhang, Y. Hao, Z. Lin, and C. Zhu, "A simple and efficient solar cell parameter extraction method from a single current-voltage curve" *Journal of applied physics*, vol. 110, no. 6, pp. 064504, 2011.

[56] F. Hao, C. C. Stoumpos, D. H. Cao, R. P. H. Chang, and M. G. Kanatzidis, "Lead-free solid-state organic–inorganic halide perovskite solar cells", *Nature Photonics*, vol. 8, no. 6, pp. 489, 2014.

[57] Q. Q. Lin, A. Armin, R. C. R. Nagiri, P. L. Burn, and P. Meredith, "Electro-optics of perovskite solar cells", *Nature Photonics*, vol. 9, no. 2, pp. 106, 2015.

[58] A. Miyata, A. Mitioglu, P. Plochocka, O. Portugall, J. T. W. Wang, S. D. Stranks, and H. J. Snaith, R. J. Nicholas, "Direct measurement of the exciton binding energy and effective masses for charge carriers in organic-inorganic tri-halide perovskites", *Nature Physics*, vol. 11, no. 7, pp. 582-587, 2015.

[59] S. D. Stranks, G. E. Eperon, G. Grancini, C. Menelaou, M. J. Alcocer, T. Leijtens, L. M. Herz, A. Petrozza, and H. J. Snaith, "Electron-hole diffusion lengths exceeding 1 micrometer in an organometal trihalide perovskite absorber", *Science*, vol. 342, no. 6156, pp. 341-344, 2013.

[60] G. Xing, N. Mathews, S. Sun, S. S. Lim, Y. M. Lam, M. Gratzel, S. Mhaisalkar, and T. C. Sum, "Long-range balanced electron-and hole-transport lengths in organic-inorganic $CH_3NH_3PbI_3$", *Science*, vol. 342, no. 6156, pp. 344-347, 2013.

[61] Q. Dong, Y. Fang, Y. Shao, P. Mulligan, J. Qiu, L. Cao, and J. Huang, "Electron-hole diffusion lengths> 175 μm in solution grown CH3NH3PbI3 single crystals", *Science*, pp. aaa5760, 2015.

[62] N. Pellet, P. Gao, G. Gregori, T. Y. Yang, M. K. Nazeeruddin, J. Maier, and M. Gratzel, "Mixed-organic-cation Perovskite photovoltaics for enhanced solar-light harvesting", *Angewandte Chemie*, vol. 126, no. 12, pp. 3215-3221, 2014.

[63] W. S. Yang, J. H. Noh, N. J. Jeon, Y. C. Kim, S. Ryu, J. Seo, and S. I. Seok, "High-performance photovoltaic perovskite layers fabricated through intramolecular exchange", *Science*, vol. 348, no. 6240, pp. 1234-1237, 2015.

[64] H. S. Kim, C. R. Lee, J. H. Im, K. B. Lee, T. Moehl, A. Marchioro, S. J. Moon, R. Humphry-Baker, J. H. Yum, and J. E. Moser, "Lead iodide perovskite sensitized all-solid-state submicron thin film mesoscopic solar cell with efficiency exceeding 9%", *Scientific reports*, vol. 2, pp. 591, 2012.

[65] N. Ahn, D. Y. Son, I. H. Jang, S. M. Kang, M. Choi, and N. G. Park, "Highly reproducible perovskite solar cells with average efficiency of 18.3% and best efficiency of 19.7% fabricated via Lewis base adduct of lead (II) iodide", *Journal of the American Chemical Society*, vol. 137, no. 27, pp. 8696-8699, 2015.

[66] D. Liu and T. L. Kelly, “Perovskite solar cells with a planar heterojunction structure prepared using room-temperature solution processing techniques”, *Nature photonics*, vol. 8, no. 2, pp. 133, 2014.

[67] N. J. Jeon, J. H. Noh, Y. C. Kim, W. S. Yang, S. Ryu, and S. I. Seok, “Solvent engineering for high-performance inorganic–organic hybrid perovskite solar cells”, *Nature materials*, vol. 13, no. 9, pp. 897, 2014.

[68] H. Zhou, Q. Chen, G. Li, S. Luo, T. B. Song, H. S. Duan, Z. Hong, J. You, Y. Liu, and Y. Yang, “Interface engineering of highly efficient perovskite solar cells”, *Science*, vol. 345, no. 6196, pp. 542-546, 2014.

[69] M. Liu, M. B. Johnston, and H. J. Snaith, “Efficient planar heterojunction perovskite solar cells by vapour deposition”, *Nature*, vol. 501, no. 7467, pp. 395, 2013.

[70] K. Domanski, W. Tress, T. Moehl, M. Saliba, M. K. Nazeeruddin, and M. Gratzel, “Working Principles of Perovskite Photodetectors: Analyzing the Interplay Between Photoconductivity and Voltage-Driven Energy-Level Alignment”, *Advanced Functional Materials*, vol. 25, no. 44, pp. 6936-6947, 2015.

[71] Z. K. Tan, R. S. Moghaddam, M. L. Lai, P. Docampo, R. Higler, F. Deschler, M. Price, A. Sadhanala, L. M. Pazos, D. Credgington, and F. Hanusch, “Bright light-emitting diodes based on organometal halide perovskite”, *Nature nanotechnology*, vol. 9, no. 9, pp. 687-692, 2014.

[72] G. Xing, N. Mathews, S. S. Lim, N. Yantara, X. Liu, D. Sabba, M. Gratzel, S. Mhaisalkar, and T. C. Sum, “Low-temperature solution-processed wavelength-tunable perovskites for lasing”, *Nature materials*, vol. 13, no. 5, pp. 476, 2014.

[73] M. Saliba, S. M. Wood, J. B. Patel, P. K. Nayak, J. Huang, J. A. Alexander-Webber, B. Wenger, S. D. Stranks, M. T. Horantner, J. T. Wang, R. J. Nicholas, L. M. Herz, M. B. Johnston, S. M. Morris, H. J. Snaith, and M. K. Riede, "Structured organic–inorganic perovskite toward a distributed feedback laser," *Advanced Materials*, vol. 28, no. 5, pp. 923-929, 2016.

[74] M. A. Green, A. Ho-Baillie, and H. J. Snaith, "The emergence of perovskite solar cells", *Nature photonics*, vol. 8, no. 7, pp. 506, 2014.

[75] L. Wang, G. D. Yuan, R. F. Duan, F. Huang, T. B. Wei, Z. Q. Liu, J. X. Wang, and J. M. Li, "Tunable bandgap in hybrid perovskite $CH_3NH_3Pb(Br_{3-x}X_y)$ single crystals and photodetector applications", *AIP Advances*, vol. 6, no. 4, pp. 045115, 2016.

[76] T. A. Berhe, W. N. Su, C. H. Chen, C. J. Pan, J. H. Cheng, H. M. Chen, M. C. Tsai, L. Y. Chen, A. A. Dubale, and B. J. Hwang, "Organometal halide perovskite solar cells: Degradation and stability", *Energy & Environmental Science*, vol. 9, no. 2, pp. 323-356, 2016.

[77] A. Dualeh, T. Moehl, N. Tetreault, J. Teuscher, P. Gao, M. K. Nazeeruddin, and M. Grätzel, "Impedance Spectroscopic Analysis of Lead Iodide Perovskite-Sensitized Solid-State Solar Cells", *ACS Nano*, vol. 8, no. 1, pp. 4053−4053, 2014.

[78] J. A. Christians, J. S. Manser, and P.V. Kamat, "Best Practices in Perovskite Solar Cell Efficiency Measurements. Avoiding the Error of Making Bad Cells Look Good." *The journal of physical chemistry letters*, vol. 6, pp. 852−857, 2015.

[79] B. Chen, M. Yang, S. Priya, and K. Zhu, "Origin of J–V hysteresis in perovskite solar cells", *The journal of physical chemistry letters*, vol. 7, no. 5, pp. 905-917, 2016.

[80] W. Tress, N. Marinova, T. Moehl, S. M. Zakeeruddin, M. K. Nazeeruddin, and M. Grätzel, "Understanding the Rate-Dependent J−V Hysteresis, Slow Time Component, and Aging in $CH_3NH_3PbI_3$ Perovskite Solar Cells: The Role of a Compensated Electric Field", *Energy & Environmental Science*, vol. 8, no. 3, pp. 995-1004, 2015.

[81] R. S. Sanchez, V. Gonzalez-Pedro, J. W. Lee, N. G. Park, Y. S. Kang, I. Mora-Sero, and J. Bisquert, "Slow Dynamic Processes in Lead Halide Perovskite Solar Cells. Characteristic Times and Hysteresis", *The journal of physical chemistry letters*, vol. 5, no. 13, pp. 2357-2363, 2014.

[82] B. Chen, M. J. Yang, X. J. Zheng, C. C. Wu, W. L. Li, Y. K. Yan, J. Bisquert, G. Garcia-Belmonte, K. Zhu, and S. Priya, "Impact of Capacitive Effect and Ion Migration on the Hysteretic Behavior of Perovskite Solar Cells", *The journal of physical chemistry letters*, vol. 6, no. 23, pp. 4693-4700, 2015.

[83] E. L. Unger, E. T. Hoke, C. D. Bailie, W. H. Nguyen, A. R. Bowring, T. Heumueller, M. G. Christoforo, and M. D. McGehee, "Hysteresis and Transient Behavior in Current-Voltage Measurements of Hybrid-Perovskite Absorber Solar Cells", *Energy & Environmental Science*, vol. 7, no. 11, pp. 3690-3698, 2014.

[84] H. S. Kim and N. G. Park, "Parameters Affecting I-V Hysteresis of $CH_3NH_3PbI_3$ Perovskite Solar Cells: Effects of Perovskite Crystal Size and Mesoporous TiO2 Layer. *The journal of physical chemistry letters*, vol. 5, no. 17, pp. 2927-2934, 2014.

[85] J. Wei, Y. C. Zhao, H. Li, G. B. Li, J. L. Pan, D. S. Xu, Q. Zhao, and D. P. Yu, "Hysteresis Analysis Based on the Ferroelectric Effect in Hybrid Perovskite Solar Cells", *The journal of physical chemistry letters*, vol. 5, no. 21, pp. 3937-3945, 2014.

[86] H. J. Snaith, A. Abate, J. M. Ball, G. E. Eperon, T. Leijtens, N. K.Noel, S. D. Stranks, J. T. W. Wang, K. Wojciechowski, and W. Zhang, "Anomalous Hysteresis in Perovskite Solar Cells", *The journal of physical chemistry letters*, vol. 5, no. 21, pp. 3937-3945, 2014.

[87] S.V. Reenen, M. Kemerink, and H.J. Snaith, "Modeling anomalous hysteresis in perovskite solar cells", *The journal of physical chemistry letters*, vol. 6, no. 19, pp. 3808-3814, 2015.

[88] G. Namkoong, A. A. Mamun, and T. T. Ava, "Impact of PCBM/C60 electron transfer layer on charge transports on ordered and disordered perovskite phases and hysteresis-free perovskite solar cells", *Organic Electronics*, vol. 56, pp. 163-169, 2018.

[89] T. Ava, A. Al Mamun, S. Marsillac, and G. Namkoong, "A Review: Thermal Stability of Methylammonium Lead Halide Based Perovskite Solar Cells" *Applied Sciences*, vol. 9, no. 1, pp. 188, 2019.

[90] Z. Messegee, A. Al Mamun, T. T. Ava, G. Namkoong, and T. M. Abdel-Fattah, "Characterization of perovskite ($CH_3NH_3PbI_3$) degradation with the integration of different polymers for increased stability", *Materials Letters*, vol. 236, pp. 159-162, 2019.

[91] G. Niu, X. Guo, and L. Wang, "Review of recent progress in chemical stability of perovskite solar cells", *Journal of Materials Chemistry A*, vol. 3, no. 17, pp. 8970-8980, 2015.

[92] K. Miyano, M. Yanagida, N. Tripathi, and Y. Shirai, "Hysteresis, stability, and ion migration in lead halide perovskite photovoltaics", *The journal of physical chemistry letters*, vol. 7, no. 12, pp. 2240-2245, 2016.

[93] Articles by Hayley Dunning, "Scientists discover why next-gen solar cells break down in days" *Imperial college London*, 27 May 2015. (Accessed: February 2019)) (https://www.imperial.ac.uk/news/165809/scientists-discover-next-gen-solar-cells-break/)

[94] F. Sani, S. Shafie, H. Lim, and A. Musa, "Advancement on lead-free organic-inorganic halide perovskite solar cells: a review", *Materials*, vol. 11, pp. 6, pp. 1008, 2018.

[95] G. Namkoong, A. A. Mamun, T. T. Ava, K. Zhang, and H. Baumgart, "Impact of perovskite precursor solution temperature on charge carrier dynamics and photovoltaic performance of perovskite based solar cells", *Organic Electronics*, vol. 42, pp. 228-233, 2017.

[96] P. Scherrer, "Bestimmung der inneren Struktur und der Größe von Kolloidteilchen mittels Röntgenstrahlen," *In Kolloidchemie Ein Lehrbuch, Springer, Berlin, Heidelberg*, vol. 26, pp 98-100, 1918.

[97] J. I. Langford and A. J. C. Wilson, "Scherrer after Sixty Years: A Survey and Some New Results in the Determination of Crystallite Size", *Journal of Applied Crystallography*, vol. 11, no. 2, pp. 102-113, 1978.

[98] M. M. Lee, J. Teuscher, T. Miyasaka, T. N. Murakami and H. J. Snaith, "Efficient Hybrid Solar Cells Based on Meso-Superstructured Organometal Halide Perovskites", *Science*, vol. 338, no. 6107, pp. 643-647, 2012.

[99] N. J. Jeon, H. G. Lee, Y. C. Kim, J. Seo, J. H. Noh, J. Lee, and S. I. Seok, "o-Methoxy Substituents in Spiro-OMeTAD for Efficient Inorganic–Organic Hybrid Perovskite Solar Cells", *Journal of the American Chemical Society*, vol. 136, no. 22, pp. 7837-7840, 2014.

[100] N. G. Park, "Perovskite solar cells: an emerging photovoltaic technology", *Materials today*, vol. 18, no. 2, pp. 65-72, 2015.

[101] W. J. Yin, T. Shi, and Y. Yan, "Unique properties of Halide Perovskites as possible origins of the superior solar cell performance", *Advanced Materials*, vol. 26, no. 27, pp. 4653-4658, 2014.

[102] M. L. Agiorgousis, Y. Y. Sun, H. Zeng, and S. Zhang, "Strong Covalency-Induced Recombination Centers in Perovskite Solar Cell Material $CH_3NH_3PbI_3$," *Journal of the American Chemical Society*, vol. 136, no. 41, pp. 14570-14575, 2014.

[103] G. J. A. H. Wetzelaer, M. Scheepers, A. M. Sempere, C. Momblona, J. Ávila, and H. J. Bolink, "Trap-Assisted Non-Radiative Recombination in Organic–Inorganic Perovskite Solar Cells", *Advanced Materials*, vol. 27, no. 11, pp. 1837-1841, 2015.

[104] M. Vrućinić, C. Matthiesen, A. Sadhanala, G. Divitini, S. Cacovich, S.E. Dutton, C. Ducati, M. Atatüre, H. Snaith, R.H. Friend, H. Sirringhaus, and F. Deschler, "Local Versus Long-Range Diffusion Effects of Photoexcited States on Radiative Recombination in Organic–Inorganic Lead Halide Perovskites", *Advanced Science*, vol. 2, no. 9, pp. 1500136, 2015.

[105] J. S. Yun, A. H. Baillie, S. Huang, S. H. Woo, Y. Heo, J. Seidel, F. Huang, Y. B. Cheng, and M. A. Green, "Benefit of Grain Boundaries in Organic–Inorganic Halide Planar Perovskite Solar Cells", *The journal of physical chemistry letters*, vol. 6, no. 5, pp. 875-880, 2015.

[106] Q. Chen, H. Zhou, T.B. Song, S. Luo, Z. Hong, H. S. Duan, L. Dou, Y. Liu, and Y. Yang, "Controllable Self-Induced Passivation of Hybrid Lead Iodide Perovskites toward High Performance Solar Cells", *Nano letters*, vol. 14, no. 7, pp. 4158-4163, 2014.

[107] E. Edri, S. Kirmayer, S. Mukhopadhyay, K. Gartsman, G. Hodes, and D. Cahen, "Elucidating the charge carrier separation and working mechanism of $CH_3NH_3PbI_{3-x}Cl_x$ perovskite solar cells", *Nature communications*, vol. 5, pp. 3461, 2014.

[108] H.S. Jung and N.G. Park, "Perovskite Solar Cells: From Materials to Devices", *small*, vol. 11, no. 1, pp. 10-25, 2015.

[109] W. Nie, H. Tsai, R. Asadpour, J. C. Blancon, A. J. Neukirch, G. Gupta, J. J. Crochet, M. Chhowalla, S. Tretiak, M. A. Alam, H. L. Wang, and A. D. Mohite, "High-efficiency solution-processed perovskite solar cells with millimeter-scale grains", *Science*, vol. 347, no. 6221, pp. 522-525, 2015.

[110] E. L. Unger, A. R. Bowring, C. J. Tassone, V. L. Pool, A. Gold-Parker, R. Cheacharoen, K. H. Stone, E. T. Hoke, M. F. Toney, and M. D. McGehee, "Chloride in Lead Chloride-Derived Organo-Metal Halides for Perovskite-Absorber Solar Cells", *Chemistry of Materials*, vol. 26, no. 24, pp. 7158-7165, 2014.

[111] F. Xie, W. Li, J. Chen, and N. Zhao, "The Role of Chlorine in the Formation Process of $CH_3NH_3PbI_{3-x}Cl_x$ Perovskite", *Advanced Functional Materials*, vol. 24, no. 45, pp. 7102-7108, 2014.

[112] S. Colella, E. Mosconi, P. Fedeli, A. Listorti, F. Gazza, F. Orlandi, P. Ferro, T. Besagni, A. Rizzo, G. Calestani, G. Gigli, F. D. Angelis, R. Mosca, "$MAPbI_{3-x}Cl_x$ Mixed Halide Perovskite for Hybrid Solar Cells: The Role of Chloride as Dopant on the Transport and Structural Properties", *Chemistry of Materials*, vol. 25, no. 22, pp. 4613-4618, 2013.

[113] T. W. Ng, C. Y. Chan, M. F. Lo, Z. O. Guan, and C. S. Lee, "Formation chemistry of perovskites with mixed iodide/chloride content and the implications on charge transport properties", *Journal of Materials Chemistry A*, vol. 3, no. 17, pp. 9081-9085, 2015.

[114] Y. Li, X. Xu, C. Wang, C. Wang, F. Xie, and Y. Gao, "Degradation by Exposure of Coevaporated $CH_3NH_3PbI_3$ Thin Films", *Journal of Physical Chemistry C*, vol. 119, no. 42, pp. 23996-24002, 2015.

[115] M. Takihara, T. Minemoto, Y. Wakisaka, and T. Takahashi, "An investigation of band profile around the grain boundary of Cu(InGa)Se_2 solar cell material by scanning probe microscopy", *Progress in Photovoltaics: Research and Applications*, vol. 21, no. 4, pp. 595-599, 2013.

[116] J. B. Li, V. Chawla, and B. M. Clemens, "Investigating the Role of Grain Boundaries in CZTS and CZTSSe Thin Film Solar Cells with Scanning Probe Microscopy", *Advanced Materials*, vol. 24, no. 6, pp. 720-723, 2012.

[117] M. Maiberg, C. Spindler, E. Jarzembowski, and R. Scheer, "Electrical characterization of Cu(In,Ga)Se_2-solar cells by voltage dependent time-resolved photoluminescence", *Thin Solid Films*, vol. 582, pp. 379-382, 2015.

[118] H. J. Snaith, A. Abate, J. M. Ball, G. E. Eperon, T. Leijtens, N. K. Noel, S. D. Stranks, J. T. W. Wang, K. Wojciechowski, and W. Zhang, "Anomalous hysteresis in perovskite solar cells", *Journal of Physical Chemistry letter*, vol. 5, no. 9, pp. 1511-1515, 2014.

[119] W. J. Yin, T. Shi, and Y. Yan, "Unusual defect physics in $CH_3NH_3PbI_3$ perovskite solar cell absorber. *Applied Physics Letters*, vol. 104, no. 6, pp. 063903, 2014.

[120] J. J. Li, J. Y. Ma, Q. Q. Ge, J. S. Hu, D. Wang, and L. J. Wan, "Microscopic investigation of grain boundaries in organolead halide perovskite solar cells", *ACS applied materials & interfaces*, vol. 7, no. 51, pp. 28518-28523, 2015.

[121] Y. Du, H. Cai, H. Wen, Y. Wu, Z. Li, J. Xu, L. Huang, J. Ni, J. Li, and Zhang, "Undesirable role of remnant PbI_2 layer on low temperature processed planar perovskite solar cells", *RSC Advances*, vol. 6, no. 103, pp. 101250-101258, 2016.

[122] B. Yang, O. Dyck, J. Poplawsky, J. Keum, A. Puretzky, S. Das, I. Ivanov, C. Rouleau, G. Duscher, D. Geohegan, and K. Xiao, "Perovskite solar cells with near 100% internal quantum efficiency based on large single crystalline grains and vertical bulk heterojunctions", *Journal of the American Chemical Society*, vol. 137, no. 29, pp. 9210-9213, 2015.

[123] B. W. Park, S. M. Jain, X. Zhang, A. Hagfeldt, G. Boschloo, and T. Edvinsson, "Resonance raman and excitation energy dependent charge transfer mechanism in halide-substituted hybrid perovskite solar cells", *ACS nano*, vol. 9, no. 2, pp. 2088-2101, 2015.

[124] H. He, Q. Yu, H. Li, J. Li, J. Si, Y. Jin, N. Wang, J. Wang, J. He, X. Wang, and Y. Zhang, "Exciton localization in solution-processed organolead trihalide perovskites", *Nature communications*, vol. 7, pp. 10896, 2016.

[125] H. Shibata, M. Sakai, A. Yamada, K. Matsubara, K. Sakurai, H. Tampo, S. Ishizuka, K. K. Kim, and S. Niki, "Excitation-power dependence of free exciton photoluminescence of semiconductors", *Japanese journal of applied physics*, vol. 44, no. 8R, pp. 6113, 2005.

[126] N. M. Gasanly, "Excitation intensity-and temperature-dependent photoluminescence in layered structured $Tl_2GaInSe_2S_2$ crystals", *Journal of Applied Physics*, vol. 113, no. 7, pp. 073504, 2013.

[127] W. Kong, Z. Ye, Z. Qi, B. Zhang, M. Wang, A. Rahimi-Iman, H. Wu, "Characterization of an abnormal photoluminescence behavior upon crystal-phase transition of perovskite $CH_3NH_3PbI_3$", *Physical Chemistry Chemical Physics*, vol. 17, no. 25, pp. 16405-16411, 2015.

[128] C. Wehrenfennig, G. E. Eperon, M. B. Johnston, H. J. Snaith, and L. M. Herz, "High charge carrier mobilities and lifetimes in organolead trihalide perovskites", *Advanced materials*, vol. 26, no. 10, pp. 1584-1589, 2014.

[129] C. C. Stoumpos, C. D. Malliakas, and M. G. Kanatzidis, "Semiconducting tin and lead iodide perovskites with organic cations: phase transitions, high mobilities, and near-infrared photoluminescent properties", *Inorganic chemistry*, vol. 52, no. 15, pp. 9019-9038, 2013.

[130] G. E. Eperon, V. M. Burlakov, P. Docampo, A. Goriely, and H. J. Snaith, "Morphological control for high performance, solution-processed planar heterojunction perovskite solar cells", *Advanced Functional Materials*, vol. 24, no. 1, pp. 151-157, 2014.

[131] H. H. Wang, Q. Chen, H. Zhou, L. Song, Z. St Louis, N. De Marco, and Y. Yang, "Improving the TiO_2 electron transport layer in perovskite solar cells using acetylacetonate-based additives", *Journal of Materials Chemistry A*, vol. 3, no. 17, pp. 9108-9115, 2015.

[132] P. W. Liang, C. C. Chueh, S. T. Williams, and A. K. Y. Jen, "Roles of fullerene-based interlayers in enhancing the performance of organometal perovskite thin-film solar cells", *Advanced Energy Materials*, vol. 5, no. 10, pp. 1402321, 2015.

[133] Q. Wang, Y. Shao, Q. Dong, Z. Xiao, Y. Yuan, and J. Huang, "Large fill-factor bilayer iodine perovskite solar cells fabricated by a low-temperature solution-process", *Energy & Environmental Science*, vol. 7, no. 7, pp. 2359-2365, 2014.

[134] W. Krätschmer, L. D. Lamb, K. Fostiropoulo,s and D. R. Huffman, "Solid C60: a new form of carbon", *Nature*, vol. 347, no. 6291, pp. 354, 1990.

[135] L. T. Scott, M. M. Boorum, B. J. McMahon, S. Hagen, J. Mack, J. Blank, and A. de Meijere, "A rational chemical synthesis of C60", *Science*, vol. 295, no. 5559, pp. 1500-1503, 2002.

[136] Y. Yang, J. Xiao, H. Wei, L. Zhu, D. Li, Y. Luo, and Q. Meng, "An all-carbon counter electrode for highly efficient hole-conductor-free organo-metal perovskite solar cells", *Rsc Advances*, vol. 4, no. 95, pp. 52825-52830, 2014.

[137] X. Liu, H. Yu, L. Yan, Q. Dong, Q. Wan, Y. Zhou and Y. Li, "Triple cathode buffer layers composed of PCBM, C60, and LiF for high-performance planar perovskite solar cells", *ACS applied materials & interfaces*, vol. 7, no. 11, pp. 6230-6237, 2015.

[138] Z. Xiao, Q. Dong, C. Bi, Y. Shao, Y. Yuan and J. Huang, "Solvent annealing of perovskite-induced crystal growth for photovoltaic-device efficiency enhancement", *Advanced Materials*, vol. 26, no. 37, pp. 6503-6509, 2014.

[139] J. Wang, B. Tian, V. B. Nascimento, and L. Angnes, "Performance of screen-printed carbon electrodes fabricated from different carbon inks", *Electrochimica Acta*, vol. 43, no. 23, pp. 3459-3465, 1998.

[140] G. G. Sreenivas, S. S. Ang, I. Fritsch, W. D. Brown, G. A. Gerhardt, and J. D. Woodward, "Fabrication and characterization of sputtered-carbon microelectrode array", *Analytical chemistry*, vol. 68, no. 11, pp. 1858-1864, 1996.

[141] J. J. Blackstock, A. A. Rostami, A. M. Nowak, R. L. McCreery, M. R. Freeman, and M. T. McDermott, "Ultraflat carbon film electrodes prepared by electron beam evaporation", *Analytical chemistry*, vol. 76, no. 9, pp. 2544-2552, 2004.

[142] A. V. Medovnik, Y. A. Burachevsky, V. A. Burdovitsin, and E. M. Oks, "Carbon films, prepared by electron beam evaporation of graphite target", In *Proc. of 9th Int. Conf. on Modification of Materials with Particle Beams and Plasma Flows*, 2008.

[143] A. Al Mamun, T. T, Ava, H. R. Byun, H. J. Jeong, M. S. Jeong, L. Nguyen, C. Gausin, and G. Namkoong, "Unveiling the irreversible performance degradation of organo-inorganic halide perovskite films and solar cells during heating and cooling processes", *Physical Chemistry Chemical Physics*, vol. 19, no. 29, pp. 19487-19495, 2017.

[144] R. A. Street, M. Schoendorf, A. Roy and J. H. Lee, “Interface state recombination in organic solar cells”, *Physical Review B*, vol. 81, no. 20, pp. 205307, 2010.

[145] W. Peng, B. Anand, L. Liu, S. Sampat, B. E. Bearden, A. V. Malko and Y. J. Chabal, “Influence of growth temperature on bulk and surface defects in hybrid lead halide perovskite films”, *Nanoscale*, vol. 8, no. 3, pp. 1627-1634, 2016.

[146] S. D. Stranks, V. M. Burlakov, T. Leijtens, J. M. Ball, A. Goriely and H. J. Snaith, “Recombination kinetics in organic-inorganic perovskites: excitons, free charge, and subgap states”, *Physical Review Applied*, vol. 2, no. 3, pp. 034007, 2014.

[147] H. J. Snaith, “Perovskites: the emergence of a new era for low-cost, high-efficiency solar cell”, *The Journal of Physical Chemistry Letters*, vol. 4, no. 21, pp. 3623-3630, 2013.

[148] G. Hodes, “Perovskite-based solar cells”, *Science*, vol. 342, no. 6156, pp. 317-318, 2013.

[149] M. Grätzel, “The light and shade of perovskite solar cells”, *Nature materials*, vol. 13, no. 9, pp. 838, 2014.

[150] F. Matteocci, L. Cinà, E. Lamanna, S. Cacovich, G. Divitini, P. A. Midgley, C. Ducati, and A. Di Carlo, “Encapsulation for long-term stability enhancement of perovskite solar cells”, *Nano Energy*, vol. 30, pp. 162-172, 2016.

[151] Q. Dong, F. Liu, M. K. Wong, H. W. Tam, A. B. Djurišić, A. Ng, C. Surya, W. K. Chan, and A. M. C. Ng, “Encapsulation of perovskite solar cells for high humidity conditions”, *ChemSusChem*, vol. 9, no. 18, pp. 2597-2603, 2016.

[152] F. Zhang, X. Yang, H. Wang, M. Cheng, J. Zhao, and L. Sun, “Structure engineering of hole–conductor free perovskite-based solar cells with low-temperature-processed commercial

carbon paste as cathode", *ACS applied materials & interfaces*, vol. 6, no. 18, pp. 16140-16146, 2014.

[153] I. Hwang, I. Jeong, J. Lee, M. J. Ko, and K. Yong, "Enhancing stability of perovskite solar cells to moisture by the facile hydrophobic passivation", *ACS applied materials & interfaces*, vol. 7, no. 31, pp. 17330-17336, 2015.

[154] G. Niu, W. Li, F. Meng, L. Wang, H. Dong, and Y. Qiu, "Study on the stability of $CH_3NH_3PbI_3$ films and the effect of post-modification by aluminum oxide in all-solid-state hybrid solar cells", *Journal of Materials Chemistry A*, vol. 2, no. 3, pp. 705-710, 2014.

[155] Q. D. Dao, R. suji, A. Fujii, and M. Ozaki, "Study on degradation mechanism of perovskite solar cell and their recovering effects by introducing CH_3NH_3I layers", *Organic Electronics*, vol. 43, pp. 229-234, 2017.

[156] J. M. Frost, K. T. Butler, F. Brivio, C. H. Hendon, M. Van Schilfgaarde, and A. Walsh, "Atomistic origins of high-performance in hybrid halide perovskite solar cells", *Nano letters*, vol. 14, no. 5, pp. 2584-2590, 2014.

[157] J. A. Christians, P. A. Miranda Herrera, and P. V. Kamat, "Transformation of the excited state and photovoltaic efficiency of $CH_3NH_3PbI_3$ perovskite upon controlled exposure to humidified air", *Journal of the American Chemical Society*, vol. 137, no. 4, pp. 1530-1538, 2015.

[158] J. Yang, B. D. Siempelkamp, D. Liu, and T. L. Kelly, "Investigation of $CH_3NH_3PbI_3$ degradation rates and mechanisms in controlled humidity environments using in situ techniques", *ACS nano*, vol. 9, no. 2, pp. 1955-1963, 2015.

[159] Z. Zhu, V. G. Hadjiev, Y. Rong, R. Guo, B. Cao, Z. Tang, F. Qin, Y. Li, Y. Wang, and S. Venkatesan, "Interaction of organic cation with water molecule in perovskite $MAPbI_3$: From dynamic orientational disorder to hydrogen bonding", *Chemistry of Materials*, vol. 28, no. 20, pp. 7385-7393, 2016.

[160] G. Grancini, V. D'Innocenzo, E. R. Dohner, N. Martino, A. S. Kandada, E. Mosconi, F. De Angelis, H. I. Karunadasa, E. T. Hoke, and A. Petrozza, "$CH_3NH_3PbI_3$ perovskite single crystals: surface photo physics and their interaction with the environment", *Chemical science*, vol. 6, no. 12, pp. 7305-7310, 2015.

[161] M. Spina, A. Karimi, W. Andreoni, C. A. Pignedoli, B. Náfrádi, L. Forróvand, and E. Horváth, "Mechanical signatures of degradation of the photovoltaic perovskite $CH_3NH_3PbI_3$ upon water vapor exposure", *Applied Physics Letters*, vol. 110, no. 12, pp. 121903, 2017.

[162] K. Jemli, H. Diab, F. Lédée, G. Trippé-Allard, D. Garrot, B. Geffroy, J. S. Lauret, P. Audebert, and E. Deleporte, "Using Low Temperature Photoluminescence Spectroscopy to Investigate $CH_3NH_3PbI_3$ Hybrid Perovskite Degradation", *Molecules*, vol. 21, no. 7, pp. 885, 2016.

[163] T. Y. Tsui and G. M. Pharr, "Substrate effects on nanoindentation mechanical property measurement of soft films on hard substrate", *Journal of Materials Research*, vol. 14, no. 1, pp. 292-301, 1999.

[164] N. Aristidou, C. Eames, I. Sanchez-Molina, X. Bu, J. Kosco, M. S. Islam, and S. A. Haque, "Fast oxygen diffusion and iodide defects mediate oxygen-induced degradation of perovskite solar cells", *Nature communications*, vol. 8, pp. 15218, 2017.

[165] X. Qin, Z. Zhao, Y. Wang, J. Wu, Q. Jiang, and J. You, "Recent progress in stability of perovskite solar cells", *Journal of Semiconductors*, vol. 38, no. 1, pp. 011002, 2017.

[166] M. K. Gangishetty, R. W. Scott, and T. L. Kelly, "Effect of relative humidity on crystal growth, device performance and hysteresis in planar heterojunction perovskite solar cells", *Nanoscale*, vol. 8, no. 12, pp. 6300-6307, 2016.

[167] S. R. Jian, G. J. Chen, and W. M. Hsu, "Mechanical properties of Cu_2O thin films by nanoindentation", *Materials*, vol. 6, no. 10, pp. 4505-4513, 2013.

[168] C. Y. Huang, P. J. Hsieh, I. C. Chen, W. C. Ke, P. F. Yang, and S. R. Jian, "Nanoindentation of Mg-doped AlGaN thin films", *Journal of alloys and compounds*, vol. 593, pp. 220-223, 2014.

[169] A. M. Coratolo, N. Orlovskaya, M. Lugovy, V. Slyunyayev, S. Dub, C. Johnson, and R. Gemmen, "Nanoindentation of $LaCrO_3$ thin films", *Journal of materials science*, vol. 41, no. 10, pp. 3105-3111, 2006.

[170] S. Sun, Y. Fang, G. Kieslich, T. J. White, and A. K. Cheetham, "Mechanical properties of organic–inorganic halide perovskites, $CH_3NH_3PbX_3$ (X= I, Br and Cl), by nanoindentation", *Journal of Materials Chemistry A*, vol. 3, no. 36, pp. 18450-18455, 2015.

[171] Y. Rakita, S. R. Cohen, N. K. Kedem, G. Hodes, and D. Cahen, "Mechanical properties of $APbX_3$ (A=Cs or CH_3NH_3; X= I or Br) perovskite single crystals", *MRS Communications*, vol. 5, no. 4, pp. 623-629, 2015.

[172] M. A. Haque, A. D. Sheikh, X. Guan, and T. Wu, "Metal oxides as efficient charge transporters in perovskite solar cells", *Advanced Energy Materials*, vol. 7, no. 20, pp. 1602803, 2017.

[173] C. J. Flynn, S. M. McCullough, L. Li, C. L. Donley, Y. Kanai, and J. F. Cahoon, "Passivation of nickel vacancy defects in nickel oxide solar cells by targeted atomic deposition of boron", *The Journal of Physical Chemistry C*, vol. 120, no. 30, pp. 16568-16576, 2016.

[174] K. Kawano, R. Pacios, D. Poplavskyy, J. Nelson, D. D. Bradley, and J. R. Durrant, "Degradation of organic solar cells due to air exposure", *Solar energy materials and solar cells*, vol. 90, no. 20, pp. 3520-3530, 2006.

[175] M. Jørgensen, K. Norrman, and F. C. Krebs, "Stability/degradation of polymer solar cells", *Solar energy materials and solar cells*, vol. 92, no. 7, pp. 686-714, 2008.

APPENDIX A

This appendix is the supplementary information of chapter 4.

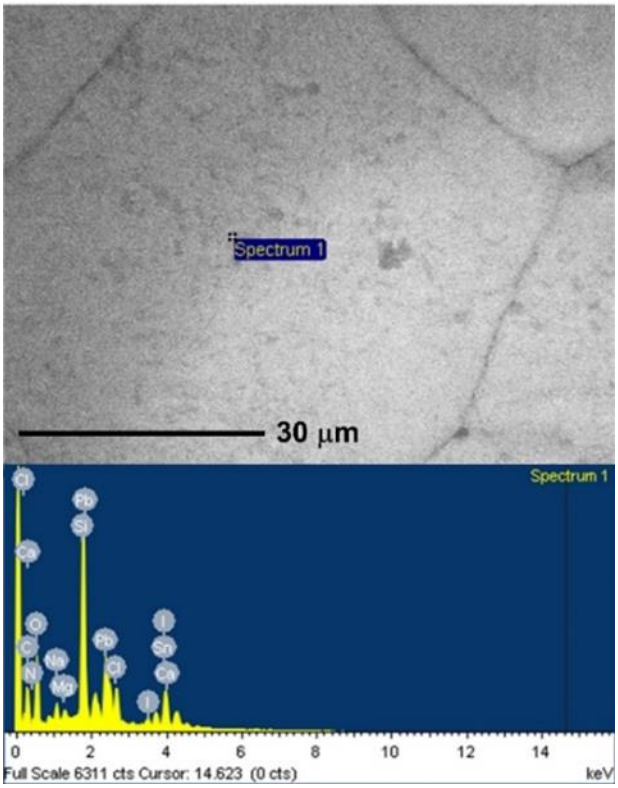

Fig. A1. EDS signals for different chemical components of the represented area showing that the chlorine signal (2.621 KeV) was clearly distinguished from the Pb signal (2.342 KeV).

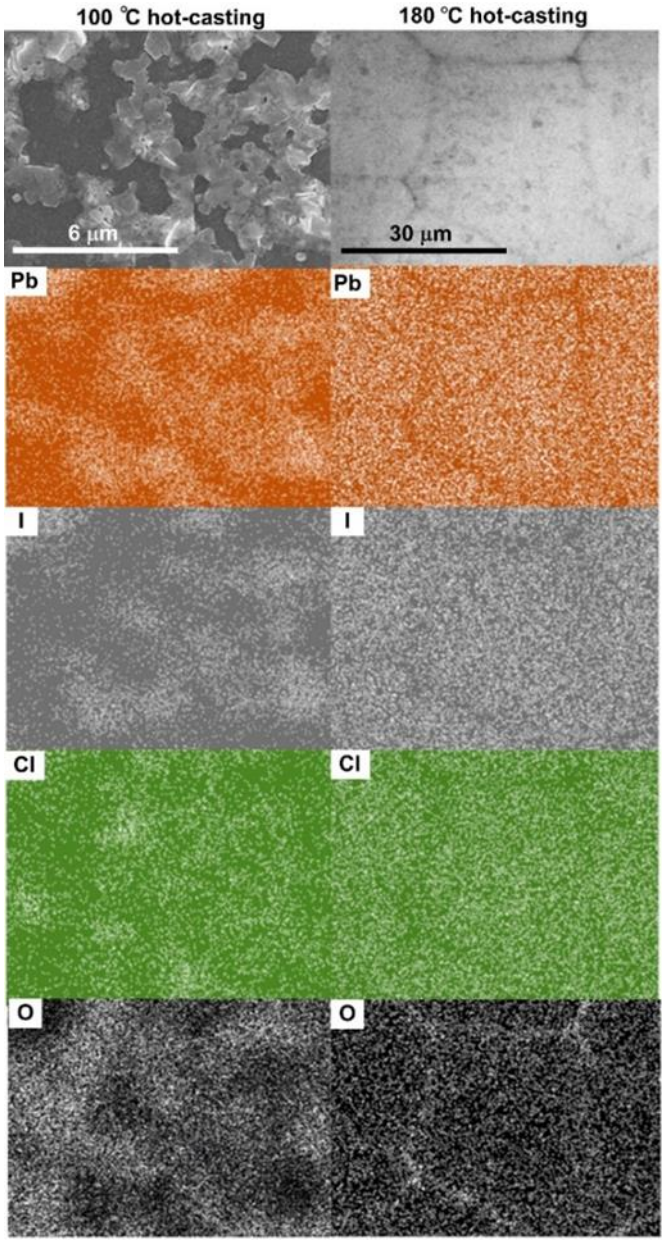

Fig. A2. Comparison of a 2D EDS mapping of lower (100 °C) and higher (180 °C) hot-casting perovskites elucidating the distributions of chemical compositions of Pb, I, Cl, and O, respectively.

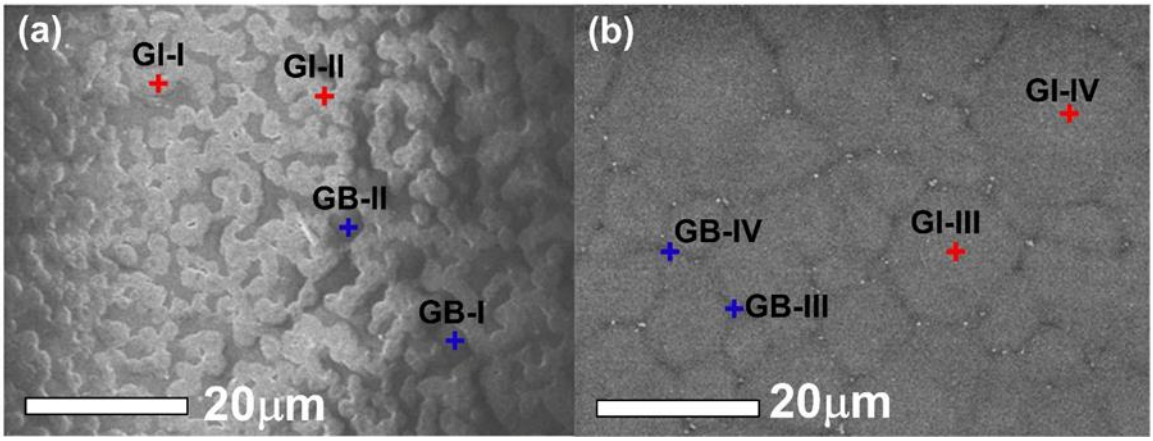

Fig. A3. SEM images of (a) a lower hot-casting perovskite and (b) a hot-casted processed perovskite showing different representative areas for EDS measurements including different GIs and GBs.

Table A1. Atomic chemical percentage of selected chemical components of lower and higher hot-casting perovskites. Other chemical elements such as Na, Mg, Al, Si, S, Ka, and Ca were detected but not shown here.

	100° hot-casting perovskite				**180 °C hot-casting perovskite**			
	GI-I	GI-II	GB-I	GB-II	GI-III	GI-IV	GB-III	GB-IV
C	9.79	10.50			19.64	17.32	11.69	12.85
O	58.28	54.97	66.44	65.89	41.95	40.58	55.80	53.64
Pb	0.97	1.25	0.47		1.14	1.54	0.33	0.37
Cl	1.21	1.19			0.71	0.86		
I	1.01	1.54	0.34		1.91	2.79	0.35	0.43

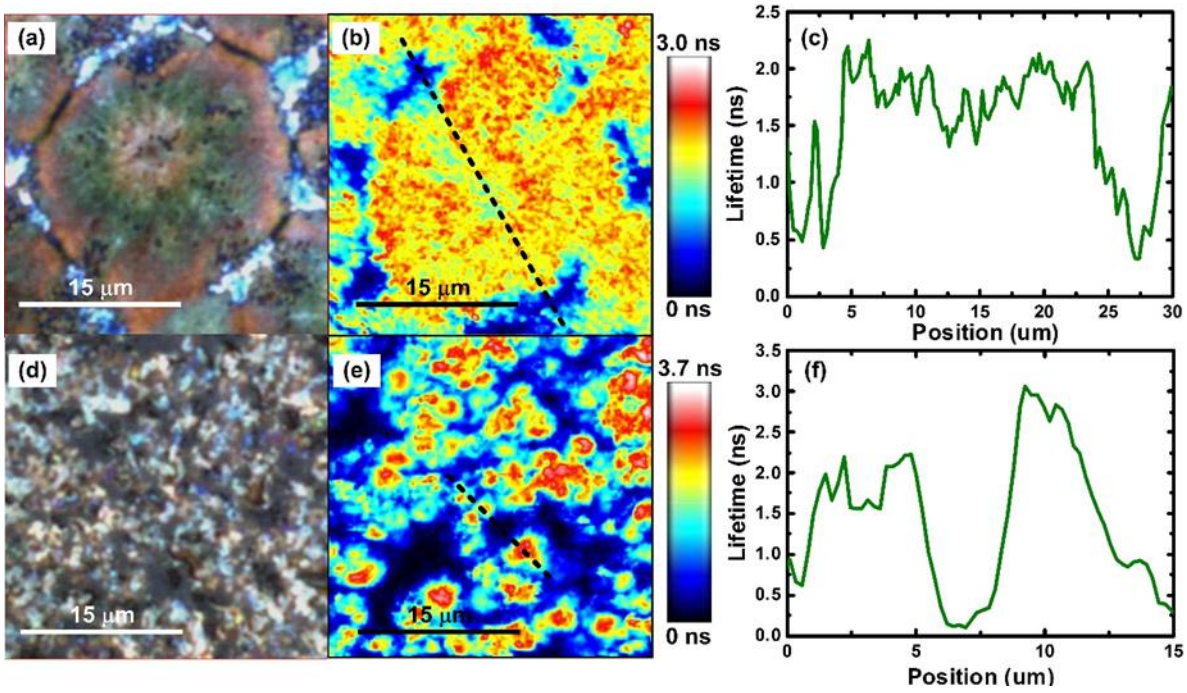

Fig. A4. Microscopic images and corresponding lifetime mapping of hot-casting perovskites that are clearly distinguishable between the GIs and the GBs. (a) and (d) microscopic images, (b) and (e) corresponding time resolved 2D lifetime mapping, (c) and (f) lifetime values as a function of positions for a higher and lower hot-casting perovskite, respectively. The average lifetimes for lower and higher hot-casting perovskites within the grains were estimated about ~ 1.8 and 2.5 ns, respectively.

VITA

Abdullah Al Mamun

amamu001@odu.edu, (757)-785-8750

www.linkedin.com/im/a-a-mamun/

344-B Saint Thomas Drive, Newport News, VA-23606

Education

PhD	Old Dominion University, Norfolk, VA, USA Ph.D. Candidate, Electrical and Computer Engineering	expected May 2019
MS	University of Dhaka, Bangladesh Applied Physics, Electronics, and Communication Engineering	July 2014
BS	University of Dhaka, Bangladesh Applied Physics, Electronics, and Communication Engineering	June 2012

Experience

- Old Dominion University, Norfolk, VA, USA
    - Graduate Research Assistant, August 2014 – present
    - Graduate Teaching Assistant, August 2016 – present
- Mentoring
    - Mentored several graduate and undergraduate research students from Old Dominion University and Christopher Newport University.

Honors and Awards

- Ph.D. Researcher of the year 2017-2018, ECE, Old Dominion University, USA, 2018.

- The Bernard Henry Fund Research Scholarship, SVC foundation, USA, 2018.
- SVC Technical Conference (Techcon) 2019 Travel Award, SVC foundation, USA, 2018.

Journal Publications

- A. A. Mamun, et al. "Influence of air degradation on morphology, crystal size and mechanical hardness of perovskite film." Materials Letters 229 (2018): 167-170.
- A. A. Mamun, et al. "New PCBM/carbon based electron transport layer for perovskite solar cells." Physical Chemistry Chemical Physics 19.27 (2017): 17960-17966.
- A. A. Mamun, et al. "A deconvoluted PL approach to probe the charge carrier dynamics of the grain interior and grain boundary of a perovskite film for perovskite solar cell applications." Physical Chemistry Chemical Physics 19.13 (2017): 9143-9148.
- A. A. Mamun, et al. "Unveiling the irreversible performance degradation of organo-inorganic halide perovskite films and solar cells during heating and cooling processes." Physical Chemistry Chemical Physics 19.29 (2017): 19487-19495.
- T. T. Ava, A. A. Mamun, et al. "A Review: Thermal Stability of Methylammonium Lead Halide Based Perovskite Solar Cells." Applied Sciences 9. (2019): 188.
- Z. Messegee, A. A. Mamun, et al. "Characterization of perovskite (CH3NH3PbI3) degradation with the integration of different polymers for increased stability." Materials Letters 236 (2019): 159-162.
- G. Namkoong, A. A. Mamun, et al. "Impact of PCBM/C60 electron transfer layer on charge transports on ordered and disordered perovskite phases and hysteresis-free perovskite solar cells." Organic Electronics 56 (2018): 163-169.

- G. Namkoong, A. A. Mamun, et al. "Impact of perovskite precursor solution temperature on charge carrier dynamics and photovoltaic performance of perovskite based solar cells." Organic Electronics 42 (2017): 228-233.
- G. Namkoong, H. J. Jeong, A. A. Mamun, et al. "Chemically, spatially, and temporally resolved 2D mapping study for the role of grain interiors and grain boundaries of organic-inorganic lead halide perovskites." Solar Energy Materials and Solar Cells, 155, 134-140.

Conference Publications and Poster Presentations

- A. A. Mamun, et al. "Investigation of Degradation of Organometal Halide Perovskite Film and Solar Cell." The Electrochemical Society, pp. 883-883. (2017)
- A. A. Mamun, et al, "Highly efficient low cost perovskite solar cell using new electron transport layer of PCBM/Carbon." AVS Mid-Atlantic Chapter meeting, April 2017.
- A. A. Mamun, et al. "Improvement towards highly efficient low cost perovskite solar cell using new electron transport layer of PCBM/Carbon." 19th annual Tidewater Student Research Poster Session, April 2017.
- G. Namkoong, H. J. Jeong, A. A. Mamun, et al. "Investigation of Dynamics of Perovskites using Chemically, Spatially and Temporally Resolved 2D Mapping." The Electrochemical Society. pp. 1405-1405. (2016)
- G. Namkoong, H. J. Jeong, A. A. Mamun, et al. "Recombination dynamics of the $CH_3NH_3PbI_{3-x}Cl_x$ using chemically, spatially and temporally resolved 2D mapping. DBpia, pp. 663-663. (2016).